Quantitative Evaluation of Electrical Stimulation Therapy for Eye Disease

By

Joel Thomas

B.S., University of Illinois at Chicago, 2007

Thesis

Submitted as partial fulfillment of requirements

for the degree of Doctor of Philosophy in Bioengineering

in the Graduate College of the

University of Illinois at Chicago, 2019

Defense Committee:

John R. Hetling, PhD, Chair and Advisor

Thomas Royston, PhD, Mechanical Engineering

Anthony Felder, PhD, Bioengineering

James McAnany, PhD, Ophthalmology and Visual Sciences

Laxman Saggere, PhD, Mechanical and Industrial Engineering

Dedication

I would like to dedicate this thesis to my parents George and Aleykutty Thomas, for their support over the course of this research and for impressing the importance of education and hard work.

I would also like to dedicate this thesis to the friends I have made over the years while at UIC, who enriched and defined this journey; to the places we've been, and the places we'll go.

Acknowledgments

I would like to thank my advisor Dr. John R. Hetling for his expertise, mentorship and persistence over the years.

This work would not have been possible without the contributions of my peers. I owe thanks to several members of Dr.Hetling's Neural Engineering Vision Laboratory. I would like to thank Dr. Tamas Ban and Dr. Ashley Selner for their input on computational modeling. Dr. Zahra Derafshi, Hadi Tajali, Yelena Krakova and Navin Agarwal provided valuable assistance in conducting experiments and data analysis.

Special thanks to Dr. Safa Rahmani and Dr. Les Bogdanowicz from the Hetling lab as well as Dr. Machelle Pardue and Moon Han from the Pardue lab at the Atlanta VA Medical Center for their pioneering work in electrical stimulation therapy.

This work was supported in part by Department of Veterans Affairs Grant No. C6693R.

Contribution of Authors

Sections 1 and 2 review background material and provide context for the present work within the larger fields of computational modeling in biology and vision science.

Sections 3 and 4 represent simulation work I conducted, supported by validation data I collected under the guidance of my research advisor Dr. John R. Hetling at the University of Illinois at Chicago. Figures from early efforts in these simulations showing current density distribution across the retina were presented in conference posters on which I am first author [Thomas, J. G., Selner, A., & Hetling, J. R., Exogenous currents delivered to the eye as a potential therapy: computational model comparing two electrode geometries in rat, *Association for Research in Vision and Ophthalmology* Annual Meeting, 2011] and coauthored with collaborators from Emory University [Kim, M. K., Thomas, J. G., Adkins, A., Ciavatta, V. T., Hetling, J. R., & Pardue, M. T., Electrical stimulation therapy preserves visual acuity and retinal ganglion cells in P23H-1 rats, *Association for Research in Vision and Ophthalmology* Annual Meeting, 2012]. Early results of this work are also published in collaboration with the lab of Dr. Machelle Pardue at Emory University, in a paper on which I am coauthor and provided Fig. 1 of that paper [Hanif, Adam M., et al. "Whole-Eye Electrical Stimulation Therapy Preserves Visual Function and Structure in P23H-1 Rats." Experimental Eye Research, 2016, doi:10.1016/ j.exer.2016.06.010]. The figure I contributed provides an early map of current density distribution across the retina afforded by the whole-eye stimulation electrode configuration that is the subject of that paper. Later work with further refined models comparing different electrode configurations described throughout the literature remains unpublished but a manuscript is in review as of summer 2019 on which I am first author and Dr. Hetling is the second author.

Section 5 represents my unpublished work which extends the earlier described modeling methods to human anatomy. I anticipate the research as presented in Section 3, 4 and 5 will be continued after my departure from the Hetling lab, with a solid basis in methodology as provided by the present work.

Section 6 represents electroretinogram analysis I carried out on two different data sets. The first data set was collected by Dr. Safa Rahmani in the Hetling lab at the University of Illinois at Chicago. An analysis of this data set and implications to the larger field of electrical stimulation therapy in the eye is published in a manuscript on which I am coauthor [Rahmani, Safa, et al. "Chronic Delivery of Low-Level Exogenous Current Preserves Retinal Function in Pigmented P23H Rat." Vision Research, 2013, doi:10.1016/ j.visres.2012.10.016]. My contribution was to provide Fig. 4. And Table 1 of that manuscript, which provide insight into effects of the electrical stimulation therapy over time. The second data set studied in Section 6 was collected by Dr. Moon Han in the Pardue lab at Emory University. The collaboration with this lab at Emory included consultation with Dr. Hetling and I on the standard operating procedures and hardware used in the treatment protocol and data acquisition. Included in Section 6 is my own unpublished, detailed analysis of this electroretinogram data which gives further insight into the functional effects of electrical stimulation therapy on the eye.

Section 7 represents an overall summary of the research presented in this thesis, as well as future directions to consider in this research.

Table of Contents

List of Tables

List of Figures

List of Abbreviations

adRP	Autosomal Dominant Retinitis Pigmentosa
AMD	Age-related Macular Degeneration
cAMP	Cyclic Adenosine Monophosphate
DTL	Dawson-Trick-Litzkow
EEG	Electroencephalography
EFP	Evoked Field Potential
ERG	Electroretinogram
ES	Electrical stimulation
EST	Electrical Stimulation Therapy
NEI	National Eye Institute
NMES	Neuromuscular Electrical Stimulation
NORD	National Organization for Rare Disorders
OCT	Optical Coherence Tomography
OIS	Optical Imaging of Intrinsic signals
RP	Retinitis pigmentosa
SES	Subretinal electrical stimulation
TENS	Transcutaneous Electrical Nerve Stimulation
TES	Transcorneal electrical stimulation
VEGF	Vasoendothelial growth factor
VEP	Visual Evoked Potential
WES	Whole-eye electrical stimulation

Summary

Electrical stimulation therapy (EST) is an emerging treatment for degenerative diseases of the retina. There is great variety in EST protocol parameters (e.g.: electrode configuration, stimulus strength, waveform, treatment schedule) that have been reported by different labs in literature. Thus there is a need for a way to objectively compare the different protocols and to correlate the protocol parameters with treatment effects (e.g.: functional and histological measures of structure and function). Towards this end, the focus of this work was to develop and validate finite element (FE) models that provide spatial maps of current density distribution in retinal tissue afforded by different EST electrode configurations, and to evaluate possible functional effects of EST on retinal tissues via electroretinogram (ERG) analysis. The FE simulation environment creates a "level playing field" in which different protocol parameters can be evaluated.

A base geometry of the rat head was developed in Solidworks and imported to ANSYS for FE electrostatic simulations. Measurements for validation and optimization of the model were taken from rat specimens undergoing EST. Three representative electrode configurations were applied to the base geometry for comparison of the current density distribution given by each: whole-eye electrical stimulation (WES), transcorneal electrical stimulation (TES) and subretinal electrical stimulation (SES). Similarly, simulations were carried out on a base geometry of the human head with representative electrode configurations applied. Spatial profiles of current density from the different electrode configurations were plotted for comparison. The results show distinct current density distribution profiles afforded by the different electrode configurations. Notably, the distribution from the SES configuration in the

rat model appears to be affected by the altered conductivity approximation of a degenerated retina, while distributions from the TES and WES configurations remained unchanged. Also noteworthy is the effect of changing the position of the reference electrode in the human model, although there is a lack of validation data from human subjects to support generalized claims.

Analysis of ERG waveforms was conducted on data collected in the Hetling lab at the University of Illinois at Chicago as well as data collected at the Pardue lab in the Center for Visual and Neurocognitive Rehabilitation, VA Medical Center, Atlanta. Trends in a-wave amplitude, b-wave amplitude, half-saturation ($I_{1/2}$) and amplification (α) between treated and control groups of P23H rats are reported, yielding insight into functional preservation in the retina when exposed to EST, despite a lack of structural preservation in the photoreceptor layer. Further analysis on these rats undergoing EST is reported elsewhere.

The methods demonstrated herein provide a means for objective, quantitative prediction and comparison of current density distribution in subjects undergoing EST in existing and future protocols. These methods may inform interpretation of the effects of existing EST protocols and the design of future clinical protocols.

1. Introduction

1.1. Motivation

Degenerative diseases of the retina are a global health concern. In particular, age related macular degeneration (AMD) is a leading cause of vision loss among the elderly both in the U.S. and globally. According to the National Eye Institute (NEI), over 2 million Americans were affected by AMD in 2010 and this is expected to more than double by 2050 [NEI, 2010]. Another disease of interest is retinitis pigmentosa (RP), a group of inherited retinopathies which affects over 2 million globally or approximately 1 in 4000 people according to National Organization for Rare Disorders (NORD) [NORD, 2017]. Treatments for such degenerative diseases have typically focused on slowing the rate of vision loss via nutritional supplements and pharmacological interventions. An emerging treatment strategy entails the delivery of electrical stimulation therapy (EST). Studies on this approach have been reported in animal models of specific eye diseases [Morimoto et al, 2007; Rahmani et al, 2013; Hanif et al, 2016] and optic nerve injury [Tagami et al, 2009; Yin 2016], as well as in human patients [Schatz et al, 2017].

The various labs investigating EST to treat retinal diseases have used a variety of electrode configurations and treatment protocols [reviewed in Sehic et al, 2016]. It would be useful to the understanding of the designs and effects of these protocols both in research and clinical settings to map the spatial distribution of electric fields afforded by the different electrode geometries. This thesis provides such maps, with models predicting current density at the retina from the common electrode geometries used to deliver EST. The methodology here can be further extended to make predictions on the distribution of electric fields from future electrode designs in both animal and human subjects. An evaluation of measured potentials from

rats undergoing EST as well as electroretinogram (ERG) data is also provided, for validation of the models and quantification of the potential functional effects of the treatment. The goal of this work is to provide a quantified basis to understand the design and optimization of present and future EST protocols and associated electrodes.

1.2. Specific Aims

The focus of this work was to develop and validate models that provide spatial maps of current density distribution in retinal tissue afforded by different EST electrode configurations, and to evaluate possible functional effects of EST on retinal tissues. Towards these goals, which provide quantified measures of the effects of EST, the specific aims of this thesis were as follows:

Specific Aim 1. Build and validate an electrostatic model of a rat head undergoing EST.

This entailed constructing the geometry of the rat head with detailed ocular structures in Solidworks. To this base geometry silver pellet electrodes at the cornea and in the mouth, as used in a whole-eye stimulation (WES) EST protocol, were also represented. This geometry was then discretized into tetrahedral elements for finite element analysis (FE) in ANSYS software. Conductivity values as reported in literature were assigned throughout the model and a 0-volt boundary condition applied to the reference electrode. Neglecting magnetic flux density at low-frequencies, Maxwell's equations were reduced and solved to obtain electric potentials throughout the model. These simulated potentials were compared against measured potentials from analogous locations on rat specimens exposed to the same WES protocol. Per sensitivity analysis of tissue conductivities factored into the present model of the rat head, sensitivity analysis in a rat eye model as reported by Selner et al. [Selner et al., 2018] and post-mortem tissue changes reported in literature, muscle conductivity was chosen for incremental adjustment

in the model. An error function was used to compare the simulated potentials vs. measured potentials and determine an optimal value of muscle conductivity to be used for subsequent models.

Specific Aim 2. Predict current density at the retina using the electrostatic model of a rat head for different EST electrode configurations.

Using the base geometry of the rat head developed in specific aim 1., three distinct electrode geometries were compared in simulation. In addition to the previously mentioned WES electrode configuration, other configurations applied were transcorneal electrical stimulation (TES) using concentric ring electrodes [Morimoto et al., 2005, 2007, 2010, 2012] and subretinal electric stimulation (SES) using parallel plate electrodes on opposing sides of a silicon chip implanted in the subretinal space [Pardue et al., 2005]. Assigning a constant, time-invariant current input as the applied load (active electrode surface) and a 0-volt boundary condition at the reference electrode surface, the potential at each node was again solved using Maxwell's equations in ANSYS. For comparison of current density distribution in healthy vs. degenerated retinal tissue, a degenerated state of the retina was also approximated by applying the conductivity value of the adjacent cell layer to the OLM layer. These simulations provide maps of the spatial distribution of current density throughout the rat head given by the different electrode configurations in both healthy and degenerated retinal layers.

Specific Aim 3. Develop a model of the human head and predict current density at the retina afforded by EST.

In a process similar to that described in specific aim 1, the geometry of the human head with detailed ocular structures was constructed in Solidworks. To this base geometry, two different electrode configurations were applied. A Dawson-Trick-Litzkow (DTL) electrode with a reference electrode on the ipsilateral temple [Schatz et al., 2011; Naycheva et al., 2013] and the ERG-Jet electrode with reference electrode similarly placed on the ipsilateral temple [Xie et al. 2011] were used as representative electrode configurations in human EST protocols. This geometry was then discretized into tetrahedral elements for FE analysis in ANSYS software. Assigning a constant, time-invariant current input as the applied load (active electrode surface) and a 0-volt boundary condition at the reference electrode surface, the potential at each node was again solved using Maxwell's equations in ANSYS. These simulations provide maps of the spatial distribution of current density throughout the human retina given by the different electrode configurations.

Specific Aim 4. Evaluate ERG data for evidence of functional rescue of retinal tissues following EST.

Electroretinogram (ERG) data was made available for analysis from two separate investigations into the effects of EST in P23H rats. Data from first study was collected by Dr. Safa Rahmani out of the Hetling lab at the University of Illinois at Chicago [Rahmani et al., 2013]. P23H rats were exposed to WES in 30-minute sessions twice a week until 16 weeks of age. Single-flash electroretinograms were recorded at 4-week intervals. The normalized ERG waveforms thus obtained were evaluated for α, considered an index of the gain or amplification in phototransduction. Change in α over time was compared between treated and control animals.

Data from the second study was collected by Moon Han out of the Pardue lab at Center for Visual and Neurocognitive Rehabilitation, Atlanta VA Medical Center [Hanif et al., 2016]. P23H rats were exposed to WES for 30-minute sessions twice a week until 24 weeks of age, with ERG responses of the retina recorded every 4 weeks. The ERG waveforms thus obtained were evaluated on a-wave peak amplitude, b-wave peak amplitude, half-saturating stimulus $I_{1/2}$ and amplification factor α, for comparison between treated and control groups.

1.3 Scientific and clinical impact

The models described in this thesis may provide quantified measures for comparison of EST protocols to treat degenerative diseases of the retina. As described in this thesis, an anatomically correct model of the rat head was developed, validated and refined to predict current density distribution from a given EST electrode configuration. Maps of the spatial distribution of current density throughout the rat head given by the different electrode configurations in both healthy and diseased retinal layers may inform interpretation of the effects of present EST protocols in rats. The simulation results from the human head model described herein may similarly inform interpretation of the effects of present EST protocols in humans. The trends observed in ERG waveforms in treated vs. control animals via the ERG analysis presented here may provide multiple, quantified metrics of the functional effects of EST on the retina. The methodology for FE modeling described herein may be applied to compare future designs of EST electrode configurations.

2. Background

2.1. Anatomy and physiology of the eye

A diagram of the human eye in cross-section is presented in Figure 1. Light passes thought the cornea and into the aqueous humor, lens and vitreous before striking the retina, which covers 2/3 of the inner surface at the posterior of the eye. The optic nerve connects with the retina at the optic disc, and temporal to the optic disc is the macula, and area with the maximum density of cone photoreceptors [Kolb 2013]. Adjacent and posterior to the retina is the choroid, which provides the blood supply to the retina. The next, outermost layer is the sclera, a supporting wall that is contiguous with the dural layer of the central nervous system. The retina contains photoreceptors of two types, the rhodopsin-containing rods and the opsin-containing cones [Kolb 2013]. These photoreceptors respond to light via an enzyme-mediated cascade which results in the cell membrane hyperpolarizing. The hyperpolarized photoreceptor cells in turn depolarize horizontal and bipolar cells, which synapse to retinal ganglion cells, modulated by amacrine cells. Retinal ganglion cell axons exit the eye via the optic nerve. Action potentials are conducted via the optic nerve to the brain for higher visual processing [Kandel 2000; Kolb 2013]. These events result in electric potentials which can be measured with electrodes placed on the eye, as will be described further under the section on electroretinography (Section 2.6).

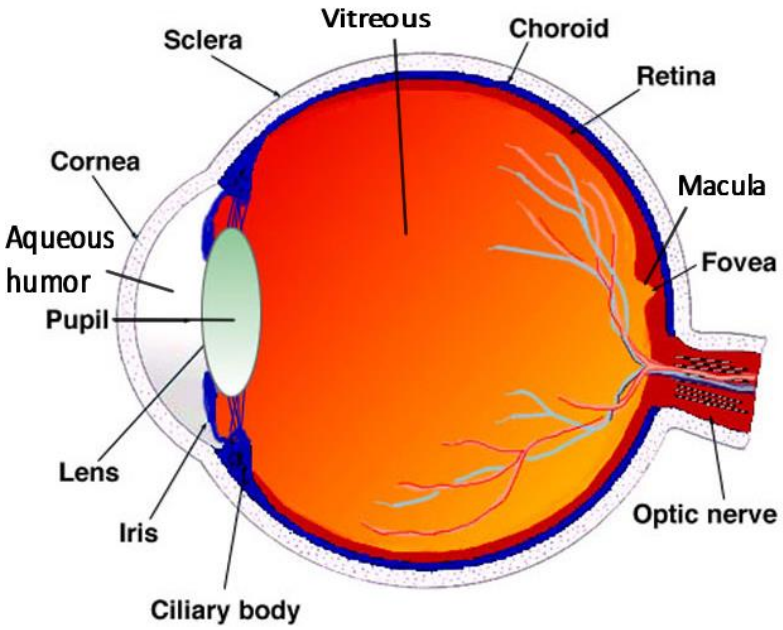

Figure 1. Anatomy of the human eye.

Figure 1. Illustration of the human eye in cross-section, showing major ocular structures. Reprinted with permission [Kolb, 2012].

While in broad terms all mammalian eyes have similar structure and function, there are key differences between human and rat eyes. Figure 2 shows a diagram of the rat eye in cross-section. Most notable is the proportionally larger size of the lens in comparison with the human eye. While there are differences in the photoreceptor types and distributions between rat and human eyes, and a notable lack of a macula in rat eyes, these differences are not relevant to the present modeling work.

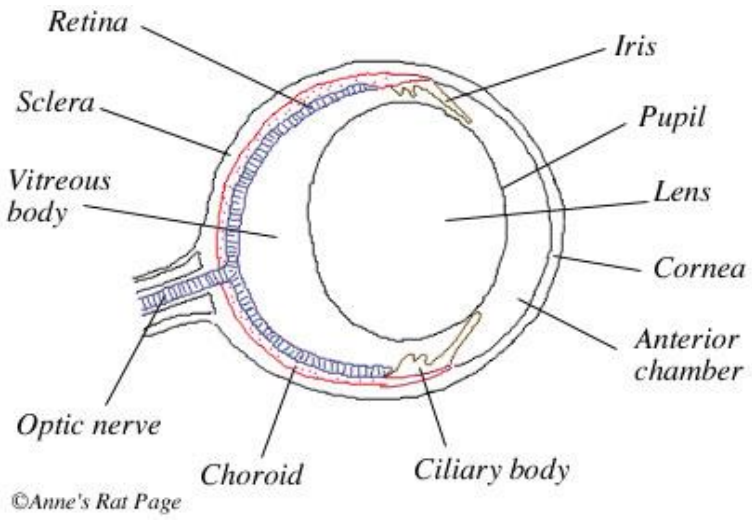

Figure 2. Anatomy of the rat eye

Figure 2. Illustration of the rat eye in cross section, showing major ocular structures. Reprinted with permission [Hanson, 2012].

Rats have been used as models of human retinal degenerative diseases (e.g.: P23H transgenic rats as a model of autosomal retinitis pigmentosa) [Machida et al., 2000]. The stratified organization of the retina in rat eyes are similar to that of human eyes. As shown in Figure 3, the human retina is comprised of several layers of tissue with distinct morphology and function. Pertinent to the composition of electrostatic models of the present study, these layers also have distinct values of electrical conductivity [Kasi et al., 2011; Wang and Weiland, 2015].

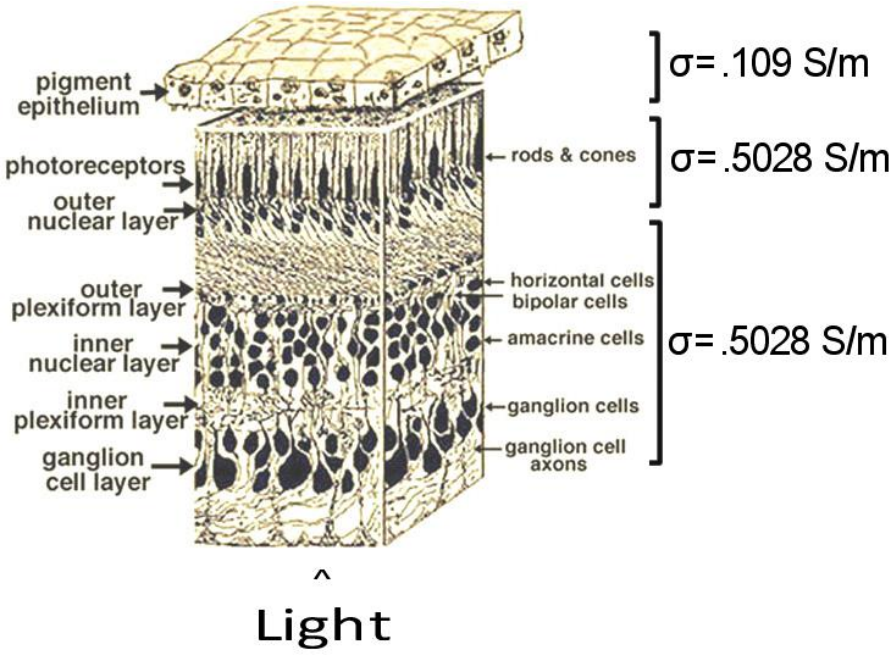

Figure 3. Cross section of the mammalian retina

Figure 3. Illustration showing layers of the mammalian retina. Conductivity values σ noted for some layers, as used in the models of the present work. Reprinted with permission [Kolb, 2012].

2.2. Degenerative diseases of the retina

2.2.1. Age-related macular degeneration

The leading cause of vision loss among people aged 50 and older is age-related macular degeneration (AMD), with 1.9 million Americans affected in 2010 and a projected 3.7 million projected to be affected by 2030. [NEI, 2010]. Diagnosis of AMD entails a combination of tests during an eye exam, including visual acuity tests, a dilated eye exam, fluorescein angiogram or optical coherence tomography (OCT) [NEI, 2018].

Most cases of AMD are classified as “dry” AMD, characterized by pigment disruption and small deposits in the retina called drusen. The disease is progressive and loss of visual

function may take years, with many patients asymptomatic and unaware of their condition. About 10-15% of cases progress to "wet" AMD, characterized by neovascularization into the subretinal space. Most therapeutic efforts have focused on wet AMD, including interventions using vascular endothelial growth factor (VEGF) inhibitors [Ba et al., 2015], antioxidant and other dietary supplements [Zampatti et al., 2014], and photodynamic therapy [Su et al., 2018]. Pertinent to the present study, multiple researchers have conducted clinical studies using an emerging treatment strategy of electrical stimulation to treat AMD [Sehic et al., 2016].

2.2.2. Retinitis Pigmentosa

Retinitis pigmentosa (RP) is a group of hereditary, progressive retinopathies which affects over 2 million globally or approximately 1 in 4000 people. According to the National Organization for Rare Disorders (NORD), RP is the most common form of inherited vision loss after AMD and glaucoma [NORD, 2017]. It is most commonly diagnosed in childhood, with children displaying sensitivity to light and difficulty navigating in low light. The visual field diminishes gradually, with most patients experiencing a loss of vision in adulthood. Common diagnostic methods include visual inspection via ophthalmoscope, electroretinogram analysis, visual field testing or genetic testing [NEI, 2018]. No effective cure has been established for the treatment of RP, and management strategies assist patients in living with vision loss. Several treatment methodologies, including nutritional supplements and gene therapies, have been investigated. Pertinent to the present study, multiple researchers have conducted animal experiments and clinical studies using an emerging treatment strategy of electrical stimulation to treat RP [Rahmani et al., 2013; Schatz et al., 2011; Schatz et al., 2017].

RP inheritance patterns may be autosomal recessive, autosomal dominant or X-linked. Autosomal dominant retinitis pigmentosa (adRP) is one of the more prevalent forms and is

associated with several rhodopsin mutations, most commonly the P23H rhodopsin mutation [Sung et al., 2006]. The P23H rat is an animal model developed to mimic adRP retinal degeneration [Machida et al., 2000].

2.3 Electrical stimulation therapies across tissue types and pathologies

Electrical stimulation (ES) has been applied for therapeutic effect across a wide range of tissue types and pathologies. Review articles as described below asses the effects of many and varied treatment protocols using exogenous electrical current, including stimulation for wound healing, muscle stimulation for stroke rehabilitation, nerve stimulation to treat neuropathic pain, and stimulation for nerve regeneration.

Hunckler and Mel recently reviewed the understanding and use of electric currents as applied to wound healing [Hunckler and Mel, 2017]. They note that several of the EST parameters, including voltage, duration, frequency, phase, mode and type of pulse are varied across studies. They determined the variation in these parameters, modes, dosage and treatment duration lead to complications in comparison of the data from multiple studies. They note the need for better designed clinical trials.

Takeda et al. reviewed neuromuscular electrical stimulation (NMES), specifically functional and therapeutic stimulation following stroke, with a focus on commercially available devices [Takeda et al., 2017]. They note that in stroke rehabilitation, NMES is used not only for strengthening of muscles and motor recovery of paralyzed limbs, but also for reducing spasticity and improving swallowing function.

Gibson et al. reviewed transcutaneous electrical nerve stimulation (TENS) versus placebo results as reported on 724 participants in 15 studies across multiple databases. They noted a

wide range in treatment duration, frequency of application, intensity of application and control conditions. They noted that the large diversity in control conditions and insufficient data across studies prevented them from making quantitative comparisons. This in turn meant they could not confidently state whether TENS had positive effects for patients with neuropathic pain [Gibson et al., 2017].

Willand et al. reviewed the biological basis for low-frequency ES to promote peripheral nerve growth, as well as potential clinical applications [Willand et al., 2016]. In regards to mechanism of action, it is noted that ES at 20Hz in peripheral nerves increases levels of cyclic adenosine monophosphate (cAMP) and upregulates neurotrophic factors and their receptors in neurons. They note imminent clinical applicability of ES to promote axonal regeneration after surgical repair, and positive effects of ES on functional recovery after a variety of peripheral nerve injuries.

With respect to the present study, an analogous variety in stimulation parameters and treatment protocols for ES to treat retinal degeneration exists, and the methodology and models provided herein may provide the means for objective comparison.

2.4 Electrical stimulation therapies for the eye

Most relevant to the present study is the available research on the use of electrical stimulation to treat eye disease. Several studies of ESTs have been reported, in both animal models of target eye diseases [Morimoto et al., 2007; Rahmani et al., 2013; Hanif et al., 2016] and optic nerve injury [Tagami et al., 2009; Yin et al., 2016], and in human patients [Schatz et al., 2017]. Over a wide range of experimental conditions, EST results have been positive, resulting in reduced rate of disease progression [Morimoto et al., 2007; Rahmani et al., 2013; Hanif et al., 2016] or enhanced recovery following experimental insult [Tagami et al., 2009; Yin 2016].

A variety of EST delivery methods and protocols have been investigated; most can be classified into one of three groups based on the arrangement of EST delivery electrodes: Whole-eye electrical stimulation (WES) places one electrode on the cornea, and the second in the mouth. In one study on this approach, electroretinogram analysis on P23H rats showed a decrease in the amplification constant in treated animals, leading to speculation that the mechanism of action for EST may be either enhanced expression of the wild-type rhodopsin gene or suppression of the mutated rhodopsin gene. The results also suggested that the EST may have accelerated horizontal cells retracting from photoreceptors.

Transcorneal electrical stimulation (TES) passes currents between two concentric ring electrodes in contact with the cornea [Morimoto et al., 2007; Tagami et al., 2009; Morimoto et al., 2010; Morimoto et al., 2012]. The proposed mechanism of action in some such studies have included upregulation of mRNAs of various growth factors, including IGF, bFGF, CNTF, NT-3, NT-4/5, GDNF and BDNF [Morimoto et al., 2007].

Subretinal electrical stimulation (SES) places active and return electrodes in the subretinal space, with results suggesting a neuroprotective effect from the implant [Pardue et al., 2005].

In the present study the phrase "TES" is used to refer to bipolar electrodes on the cornea, though this term is frequently used to describe currents delivered to induce seizures via "corneal kindling" [Potschka and Loscher,1999], or to induce phosphene perceptions with both monopolar and bipolar corneal electrodes [Sehic et al., 2016]. At least three groups investigating EST have used the phrase "TES" to describe currents delivered between a monopolar corneal electrode and a return electrode elsewhere in the body [e.g. Ni et al., 2009; Schatz et al., 2017, Fu et al., 2018], most similar to the arrangement described here as WES.

In addition to the varied electrode configurations, the EST parameters (current amplitude, waveform, frequency of treatment, duration of treatment) have also varied widely across laboratories. For example, the Morimoto et al. 2007 study on TES used RCS rats, delivering up to 100μA of current in biphasic rectangular pulses (1ms/phase) at 20Hz in one-hour sessions each week from 3 to 9 weeks of age; whereas Rahmani's 2013 study on WES used P23H transgenic rats delivered 1.5μA of sinusoidal current at 5Hz in two 30 minute sessions per week from 4 weeks to 16 weeks of age. Comparison between the different protocols is further hindered by protocols focusing on different tissue types and metrics to measure effectiveness of treatment. For example, the Morimoto et al. 2007 study evaluated the effects of EST in RCS rats via visual evoked potential (VEP) amplitude and histology. In contrast, the Ma et al. 2014 study evaluated the effects of EST in cats via measurements of neuronal activity using multiwavelength optical imaging of intrinsic signals (OIS) and via measurement of subdural evoked field potentials (EFPs) using a multichannel electrode array.

Positive EST results have been reported with WES, TES and SES configurations and across a variety of treatment protocols. These protocol differences make it difficult to summarize the present body of work into a coherent view of the physiological effects of each EST parameter, and to then progress toward optimal electrode configurations and treatment protocols. Importantly, no single study has compared EST where electrode configuration was the dependent variable. The present work focuses on this basic EST parameter, electrode configuration, with the goal of making a direct comparison between WES, TES and SES configurations in a controlled computational environment.

2.5 Modeling of electric potentials and currents in biological structures

2.5.1. Early models of electric currents in biology: body, head, eye

For the scenario of exposure to low-frequency electromagnetic fields, the human body has been modeled as a non-perfectly conducting cylinder of conductivity σ, with radius a and length L [Poljak 2003], for which the impedance per unit of length Z_L is given by:

$$Z_L(z) = \frac{1}{a^2 \pi \sigma} + Z_c \qquad \text{(Equation 1)}$$

where $Z_c(z)=1/j\omega C$ and C is the capacitance between the soles of the feet and the ground. In the case where the body is well-grounded, this capacitance is reduced to 0 and $Z_c=0$. With a known axial current I_z the current density J_z may be calculated as:

$$J_Z(z) = \frac{I_z(z)}{a^2 \pi} \qquad \text{(Equation 2)}$$

and the induced electric field calculated as:

$$E_Z(z) = \frac{J(z)}{\sigma} \qquad \text{(Equation 3)}$$

which may be recognized as the vector form of Ohm's Law (J=σE).

With regard to the present study, useful approximations of current density at the retina would necessitate a model more complex than a simple cylinder model of the whole body. Some of this complexity is acknowledged in an illustration of equipotential lines and current density arrows in the context of electroencephalography (EEG) as described by Nunez and Srinivasan [Nunez and Srinivasan, 2009] and seen in Figure 4A., which shows an idealized concentric shell model of the head.

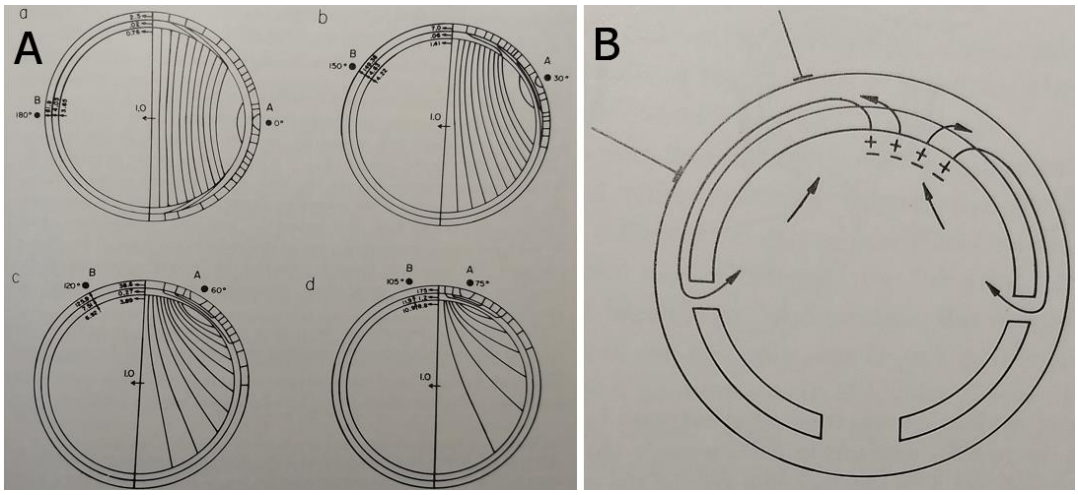

Figure 4. Concentric sphere model of electric fields from stimulating scalp electrodes.

Figure 4. Concentric sphere model of electric fields from stimulating scalp electrodes. (A) Diagram showing isopotential lines resulting from different electrode placements. (B) Model showing distortion of current flow as skull openings are introduced to the idealized model. Reprinted with permission (Nunez and Srinivasan, 2009).

Stimulating electrodes on the scalp at locations A and B connected to a voltage generator would cause current to flow from A to B, passing through scalp, skull and brain represented by

the concentric shells. Although the total current passing through electrode A must equal the current passing through electrode B, there will be considerable variation of current density throughout the head due to the geometry and inhomogeneity of the head. The fraction of the total current passing through the brain depends on the spacing of the electrodes, dropping rapidly as the electrodes are brought closer. This idealized model can be brought further in-line with real-life biology by introducing openings in the skull as seen in Figure 4B, which distorts patterns of electric potential as current flows through paths of least resistance via such openings [Nunez and Srinivasan, 2009]. The openings in the skull in this simplified model are analogous to such features as orbital fissures, the nasal cavity and various foramina in mammalian skulls, which are consequently included in the models of the present study. In other words, these openings in the skull and their significant effect on the electric field distribution throughout the head are a motivating factor to use whole-head models to compare EST electrode configurations, as was done in the present study.

Electric fields in the eye have been classically modeled in the context of electroretinography. Similar to the idealized concentric sphere model for the head in Figure 4., Krakau modeled a rabbit cornea as a perfect sphere and compared his model predictions to recorded corneal potentials [Krakau, 1958]. This work was further expanded on by Doslak et al., using a stylized eye model with separate tissue layers and numerical methods to solve for electric potential at 1000 empirically distributed nodes [Doslak et al. 1980; Doslak et al. 1981]. Doslak et al. then modeled the human electroretinogram volume conductor as an axially symmetric spherical system simplified to two dimensions [Doslak et al., 1981], as seen in Figure 5. Retinal excitation was modeled as a uniform dipole layer perpendicular to the face of the retina, and the system was solved using finite difference methods.

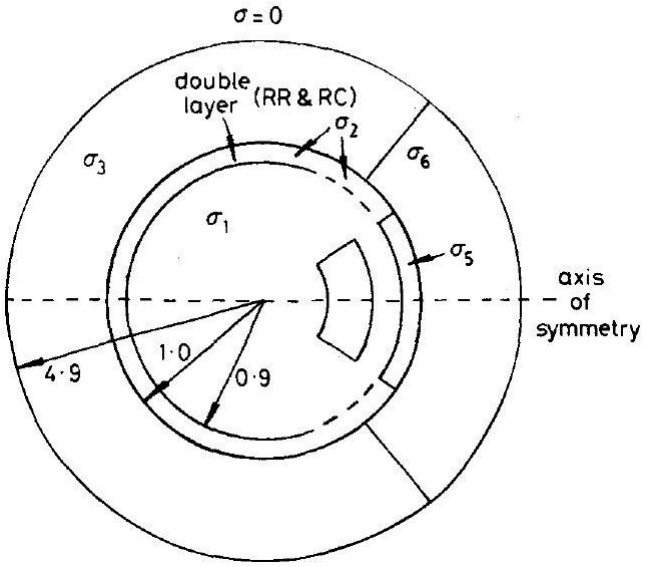

Figure 5. ERG volume conductor, Doslak et al., 1981.

Figure 5. ERG volume conductor as seen in Doslak et al., 1981. Here, the retina and R-membrane impedance are represented by the double layer and RR and RC respectively. The region conductivities are given as follows: σ1: aqueous and vitreous; σ2, slera; σ3, extraocular region; σ4, lens; σ5, cornea; σ6, air in front. The posterior of the lens region is concave to facilitate the numerical solution.

The Doslak model was extended to three dimensions by Job et al. using a finite difference method, to evaluate the use of a single electrode location with the multi-focal ERG technique [Job et al., 1999]. Here the human eye was approximated as a toroidal sphere and incorporated an accurate distribution of photoreceptor density. Results were reported as a color plot of corneal potentials, as seen in Figure 6.

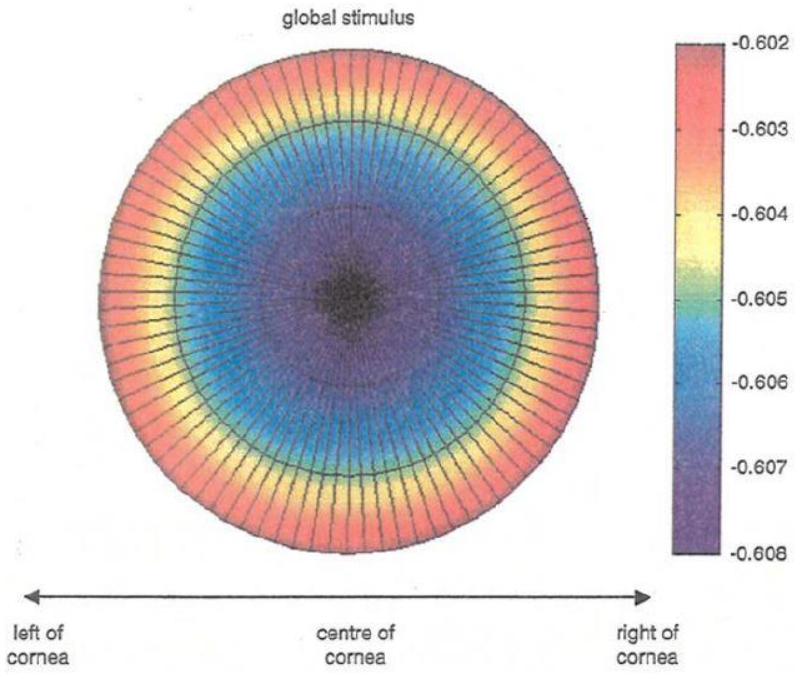

Figure 6. Map of corneal potentials, Job et al., 1999.

Figure 6. Color plot of simulated corneal potentials following full-field stimulation.

The approaches in modeling described thus far use extensive simplification of the eye geometry and are not conducive to answering questions on the effects of different electrode configurations on current density distribution in ES or the placement of these current densities in proper context, i.e.: placement in more complex morphologies such as that of a whole rat head or human head. As will be discussed, the models of the present work can address these needs.

2.5.2. Maxwell's equations

Electromagnetic fields are characterized by Maxwell's equations as follows. In the present work, Equations 4 to 7 were used to solve for the scalar potential at each node using the transient electric solver (further discussed in Section 3).

Ampere's Circuital Law: $$\nabla \times \{H\} = \{J\} + \left\{\frac{\partial D}{\partial t}\right\} = \{Js\} + \{Je\} + \{Jv\} + \left\{\frac{\partial D}{\partial t}\right\}$$ (Equation 4)

Faraday's Law:
$$\nabla \times \{E\} = -\left\{\frac{\partial B}{\partial t}\right\} \quad \text{(Equation 5)}$$

Gauss's Law for Magnetism:
$$\nabla \cdot \{B\} = 0 \quad \text{(Equation 6)}$$

Gauss's Law:
$$\nabla \cdot \{D\} = \rho \quad \text{(Equation 7)}$$

where:

$\nabla\times$	= curl operator
$\nabla\cdot$	= divergence operator
H	=magnetic field intensity vector
J	= total current density vector
Js	= applied source current density vector
Je	= induced eddy current density vector
Jvs	= velocity current density vector
D	= displacement vector, or electric flux density vector
t	= time
E	=electric field intensity vector
B	= magnetic flux density vector
ρ	=electric charge density

Taking the divergence from both sides of Equation 4 gives the continuity equation:
$$\nabla \cdot \left[\{J\} + \left\{\frac{\partial D}{\partial t}\right\}\right] = 0 \quad \text{(Equation 8)}$$

2.5.3. The FE method

Whereas the described earlier efforts solved differential equations across the entire domain of the problem, the finite element (FE) method offers a numerical method of solving differential equations by first subdividing the domain into a set of simple sub-domains referred to as finite elements. Within each element, the solution is approximated in simple polynomial form [Kim & Sankar, 2009]. This has enabled the solution of many complex practical problems with the aid of computers which were previously very difficult or impossible to solve due to domain (geometry) complexity. Though the FE method was initially used in the context of structural mechanics, it has since been adopted to other areas such as thermodynamics, fluid dynamics and electromagnetics. In broadest terms, the steps in the FE method include creation of the FE model geometry, applying boundary conditions and loads, solving the FE matrix equations and finally interpretation and verification of the results [Kim & Shankar, 2009]. Creation of the FE model entails both building a geometry representative of the problem as well as discretizing it into the finite elements.

ANSYS (Ansys Inc., Canonsburg, PA) is a commercially available software application used for commercial, research and academic purposes. In the present study, we have used ANSYS Maxwell to solve for the volume conductor problem of exogenous currents delivered to the eye in rats.

2.5.4. Model precedence: body, head, eye

Some early work using the FE method, also referred to as the Galerkin-Bubnov variant of the boundary element method (BEM), is seen in Poljak et. al's 2003 study, reporting on an analysis of human exposure to low and high frequency fields [Poljak et al., 2003]. Here, the human body was modeled as a non-perfectly conducting cylinder (see section 2.51). With regards to the present study, describing current density at the retina resulting from the delivery of exogenous current in any useful way would require a more complex geometry of the head, with particular attention to the ocular structures.

In the Chen and Mogul 2009 study a structurally detailed model of the human head was presented, in the context of transcranial magnetic stimulation (TMS) [Chen and Mogul, 2009]. The geometry for this model included structural details of the head derived from computed tomography (CT) and magnetic resonance imaging (MRI), including skull, scalp, cerebrospinal fluid system, gray matter, white matter and ventricles. Localized columns of finer features, such as pyramidal neurons traversing the neocortical layers, provided near-cellular levels of detail for the geometry. The results include color contour plots of induced current density distribution, as afforded by a 90mm circular coil with a sinusoidal voltage of 1120V at 2.4kHz.

In the Peratta study from 2008, a 3D boundary element model of the human eye in the context of conductive keratoplasty is presented [Peratta, 2008]. Here the retina is presented as a single layer with uniform conductivity, and is not further differentiated into separate layers of retinal tissue. The model solution is presented for current density distribution in different tissues as a 350kHz, high voltage signal is applied. Power absorbed is also presented, with consideration as to the amount of heat which could be dissipated by biological systems such as blood perfusion.

In the Selner et al. study from 2018, a 3D FE model of the eye is presented in the context of ERG analysis [Selner et al., 2018]. Here the eye geometry is based on a high-resolution MRI image of a rat eye, hand segmented to define major ocular structures as shown in Figure 7, with the retina presented as a single layer of uniform conductivity. The inner (vitreal) side of the retina was considered a current source with 3.48 $\mu A/mm^2$ current density, and the outer (scleral) side was considered a voltage sink. The distribution of simulated corneal potentials is reported, in good agreement with measured potentials from rats [Derafshi et al., 2017].

As evidenced by the work cited above, there is some precedence for the use of the FE method in relation to complex models of cranial and ocular structures in a variety of practical contexts. As discussed earlier (Section 2.4), there exists a need to model electrode configurations used to deliver exogenous electric currents in the context of EST, and the present work applies the FE method towards this goal. As will be detailed in Section 3, structural details in the geometry representing a rat head as well as a retina geometry (differentiated into distinct layers of retinal tissue) should provide necessary, novel detail for objective comparison of current density distribution afforded by the different electrode configurations.

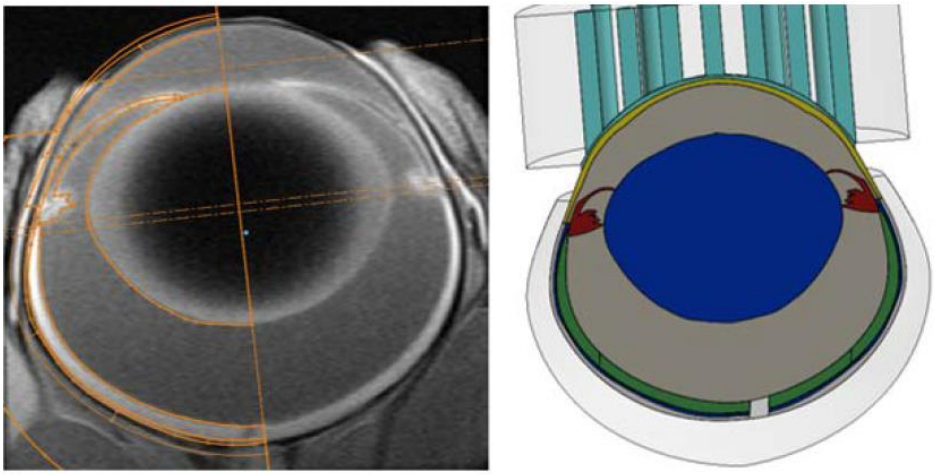

Figure 7. Rat eye model defined from MRI image.

Figure 7. Rat eye model from MRI image. Image was taken of a 50-day old Long Evans rat eye. (A) Axial cross-section view of the eye, with orange lines indicating hand segmentation to define major ocular tissue. (B) Cross-section view of the resulting, revolved 3-D geometry, done in SolidWorks. Shown with the Contact Lens Electrode Array (CLEAr Lens) applied at corneal surface. [Selner et al. 2018] © [2018] IEEE.

2.6. ERG as a diagnostic tool

Also of interest to the present thesis, electroretinography (ERG) can provide an objective functional measure of the health of the retina, which may be used to evaluate the effects of EST in rats or humans.

Electroretinography is a non-invasive technique of measuring the electric potential at the surface of the eye in response to a light stimulus. An electroretinogram has a characteristic waveform, as represented in Figure 8. The origins of the different waves that comprise this waveform have been traced to specific tissue layers within the retina via physiological and pharmacological dissection. The a-wave, an initial negative deflection in the waveform, represents the closure of cGMP-gated cationic channels to stop the flow of glutamate from the

photoreceptor layer to the inner retinal cells [Perlman, 2015]. Thus the a-wave may be considered a measure of the functionality of the photoreceptor layer. The b-wave, measured from the trough of the a-wave, represents the activity of the ON-bipolar cells [Sievang et al., 1994]. Rod-photoreceptors are dominant in dark-adapted (scotopic) ERG responses whereas cone-photoreceptors are dominant in light-adapted (photopic) ERG response [Creel, 2015].

As discussed in Section 6, the present study will use the amplitude and sensitivity characteristics from a-wave and b-wave components of the ERG waveform as metrics to compare photoreceptor functionality in EST-treated and control animals.

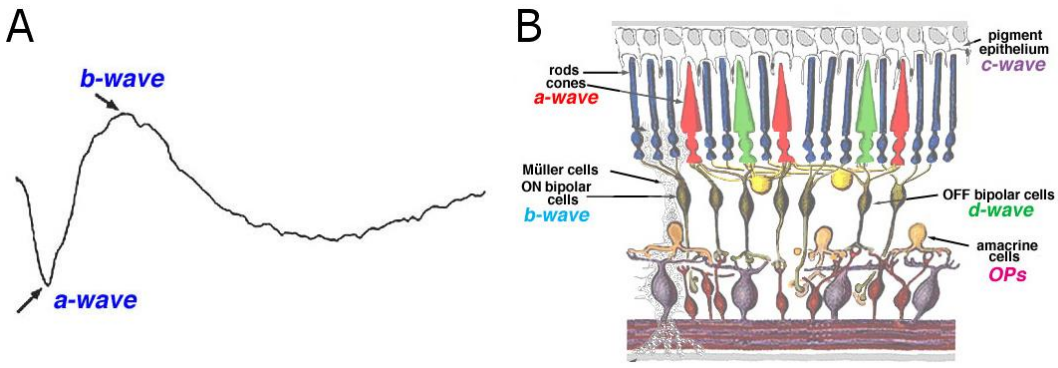

Figure 8. The ERG waveform.

Figure 8. The ERG waveform as would results from a brief, full-field flash stimulus delivered to a dark-adapted eye. A. Representative ERG waveform. B. Illustration of retinal layers showing origin of major features of the ERG waveform. Reprinted with permission [Creel, 2015].

3. Specific Aim 1 – Build and validate an electrostatic model of a rat head undergoing EST.

(Parts of this section were previously published as Hanif, Adam M., et al. "Whole-Eye Electrical Stimulation Therapy Preserves Visual Function and Structure in P23H-1 Rats." Experimental Eye Research, 2016, doi:10.1016/j.exer.2016.06.010.)

3.1. Methods of modeling

3.1.1. FE model

Here we approximated the anatomy of a rat head in a three-dimensional FE model (bone, muscle, skin, adipose tissues represented), with one eye containing a high level of detail. Tissue conductivities were taken from the literature. Rat was chosen because this species has been used by multiple groups studying EST in the eye (due to available disease and injury models, and an eye of convenient size for contacting with current-delivery electrodes) as discussed in section 2.4. The geometry was initially built in very idealized form to minimize computational load, and later models used a more anatomically detailed version of the geometry. The FE model was optimized to match experimental measurements of local potentials recorded during WES-style current delivery in recently sacrificed rats. The optimized model was then used to predict current densities across the retina for three EST electrode geometries.

3.1.1.1. Model geometry

Greene's widely referenced illustrations [Greene, 1959] such as shown in Figure 9 served as the basis for the rat skull in our geometry of the rat head for FE modeling.

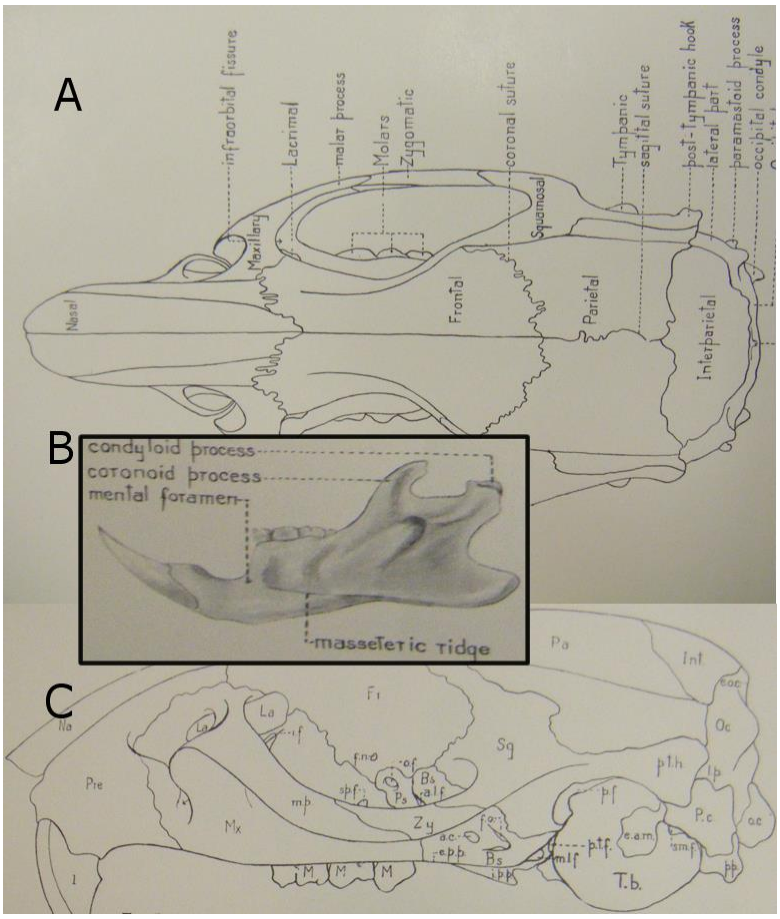

Figure 9. Anatomical drawings of the rat head.

Figure 9. Anatomical drawings of the rat head. (A) Dorsal view of the rat skull. (B) (inset) Lateral view of mandible in the rat skull. (C) Lateral view of the rat skull. Reprinted with permission [Greene, 1959].

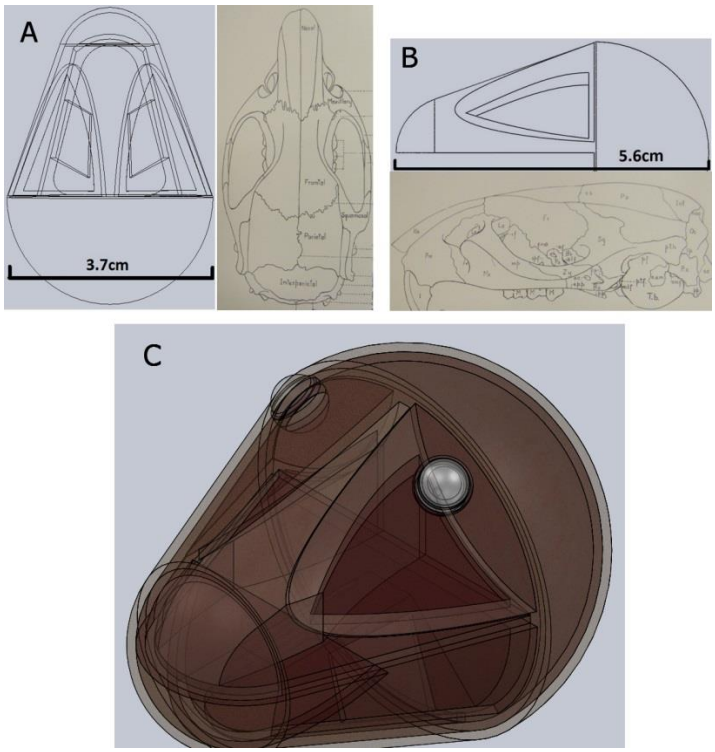

Figure 10. Rat head geometry, "muppet", idealized.

Figure 10. Rat head geometry, idealized. (A) Dorsal view, SolidWorks approximation (left) vs. anatomical drawing (right). (B) Lateral view, SolidWorks approximation (top) vs. anatomical drawing (bottom). (C) Simplified geometry of a rat head, which includes skull, muscle and bone tissues as well as a detailed assembly of the eye.

The nasal cavity, zygomatic process and surrounding soft tissues were represented in the model with the initial, idealized skull geometry. Muscle tissue, skin and a detailed eye model were then applied to the base skull structure. The optic foramen, spheno-palatine foramen, alisphenoid canal and intraorbital fissure were represented in the later, more detailed skull geometry.

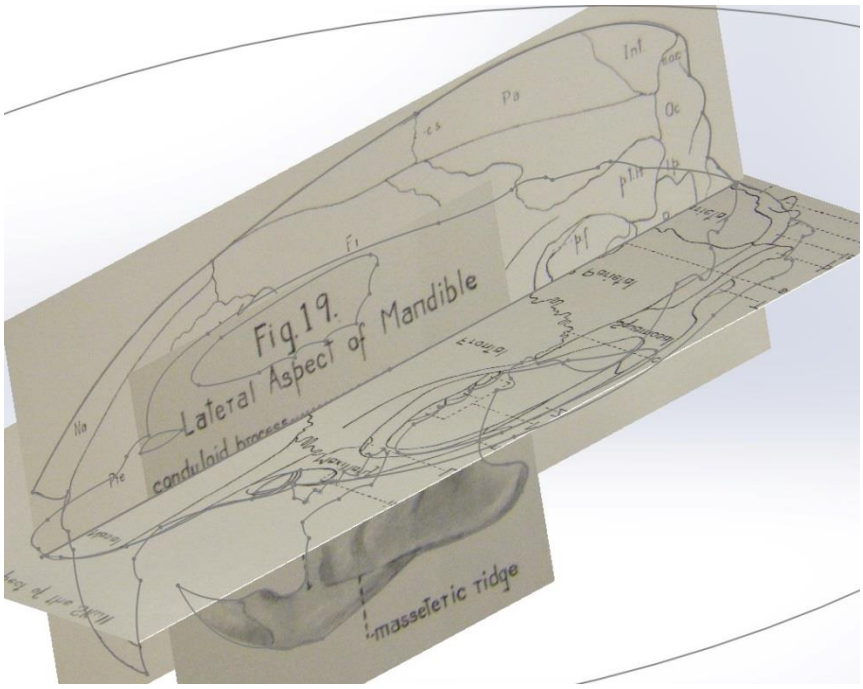

Figure 11. Anatomical drawings arranged along orthogonal planes.

Figure 11. Anatomical drawings arranged along orthogonal planes. Lateral view of the rat skull. Reprinted with permission [Greene, 1959].

The anatomical drawings used as guides in their respective, orthogonal planes can be seen in Figure 10A, B. This idealized model (colloquially referred to as the "muppet model") was utilized in initial simulations. In later, more detailed geometry (colloquially, "Remy") the orthogonal section views representing the sagittal, coronal and axial anatomical planes were extrapolated and sculpted to arrive at a three-dimensional representation of the rat skull in SolidWorks (Dassault Systemes, Velizy-Villacoublay, France), as seen Figure 9, 10.

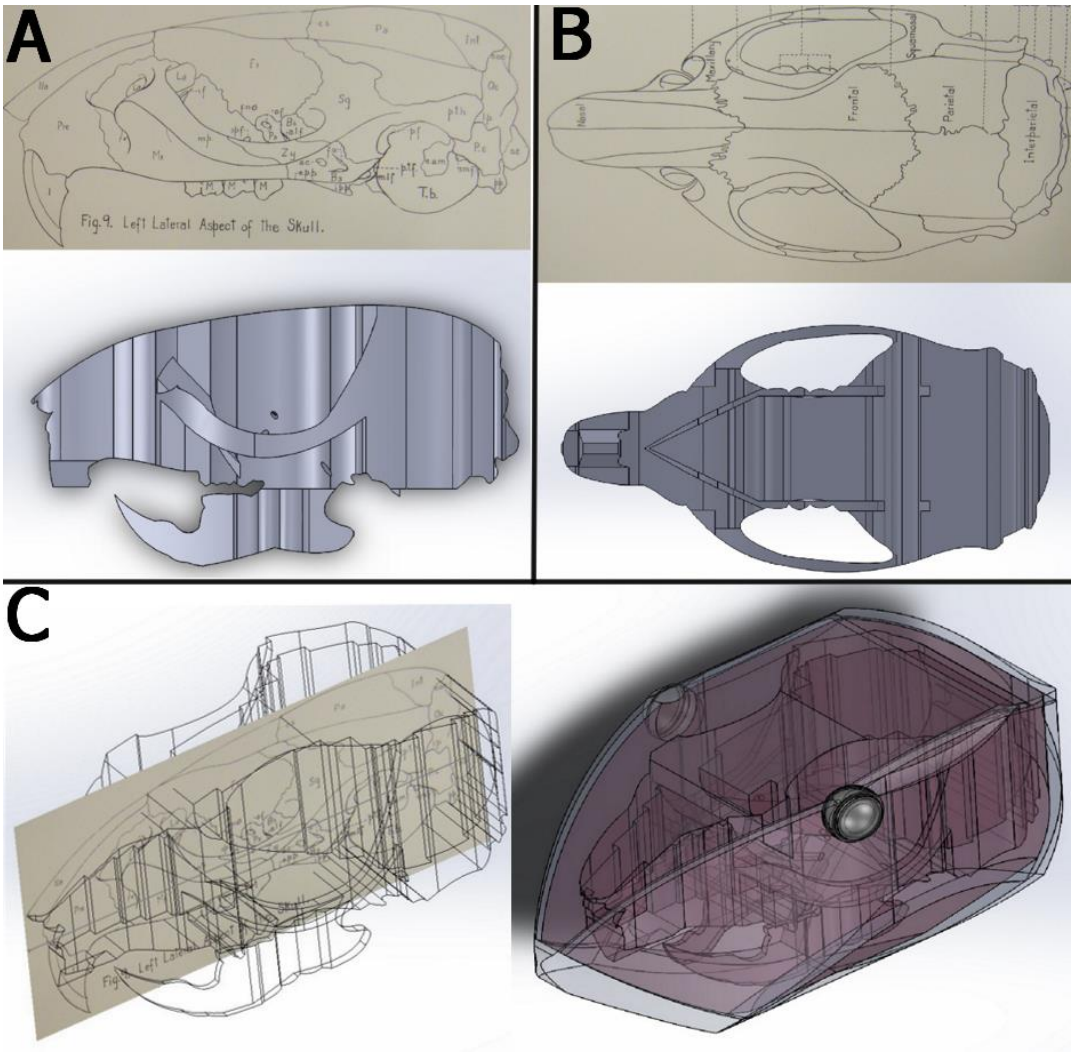

Figure 12. Rat head geometry, "Remy", added detail.

Figure 12. Rat head geometry, detailed. (A) Later view of two-dimensional anatomical drawings (top)[Greene, 1959], used as reference to create a three-dimensional model of a rat skull (bottom). (B) Dorsal view of two-dimensional anatomical drawings (top), used as reference to create a three-dimensional model of a rat skull (bottom). (C) Isometric view of the extrapolation from anatomical drawings to three-dimensional model (left), resulting in SolidWorks assembly of the model (right).

Gross anatomy of the model eyes was constructed with reference to Hughes' schematic eye of the rat [Hughes, 1979].

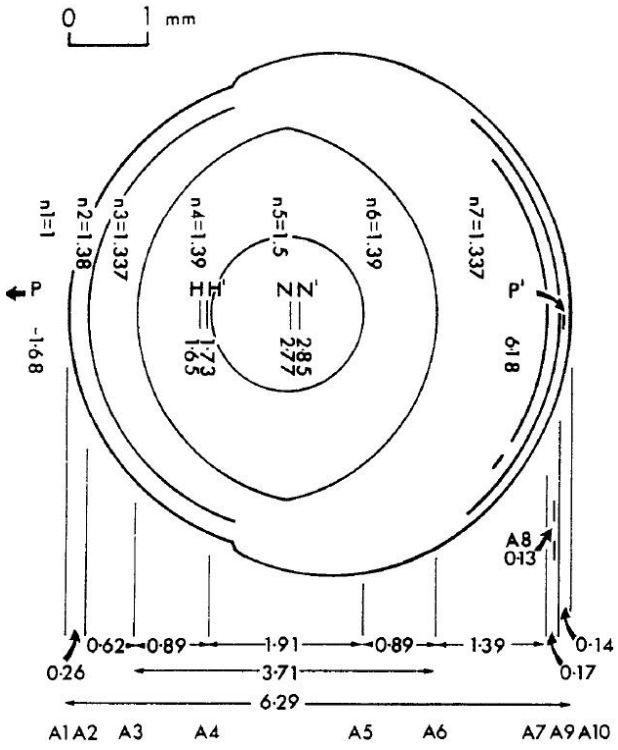

Figure 13. Schematic cross-section of the rat eye.

Figure 13. Schematic cross-section of the rat eye. Measurements shown in mm from the corneal surface where not indicated by arrows. The prefix n- denotes refractive index at different points. A1 thru A10 denote positions at the anterior cornea surface, posterior cornea surface, anterior lens surface, anterior core surface, posterior core surface, posterior lens surface, retina surface, outer limiting membrane, choroid/retina interface and posterior scleral surface respectively. Reprinted with permission [Hughes, 1979].

One eye in the model, which was taken to be the target of simulated EST, was defined with a high level of detail. As current density and distribution at, and within, the retina are of particular interest, and because conductivities of retinal layers in rodents vary significantly [Kasi et al., 2011; Wang and Weiland, 2015], the detailed model eye included discrete posterior layers (Figure 14 and Table 1).

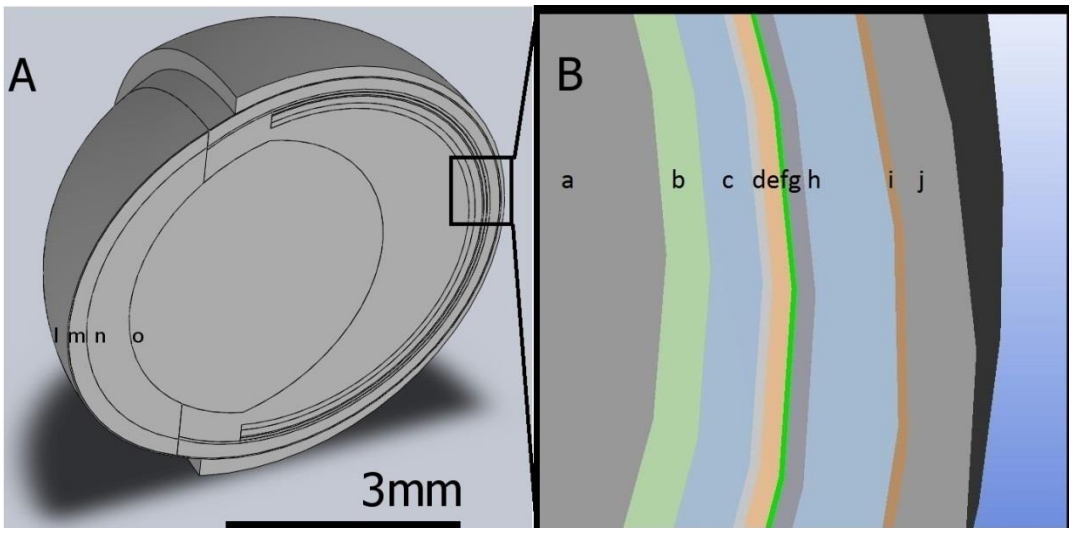

Figure 14. The rat eye geometry.

Figure 14. The rat eye geometry. (A) Cross section of model rat eye in SolidWorks based on the schematic eye described by Hughes [1979]. (B) Detail of retinal layers, labels corresponding to Table 1.

The retinal layers in the model include: retinal nerve fiber layer (RNFL); combined ganglion, amacrine, horizontal, bipolar and Muller cells (GC, AC, H/BC, MC), outer limiting membrane (OLM), and the photoreceptor layer (rods and cones). The eye model also includes distinct layers to represent the retinal pigment epithelium (RPE) and choroid. Table 1 lists the thickness (D) of each model layer along the central axis of the eye.

Tissue	Material	D (mm)	Cond. (S/m)
a	Vitreous Humor	1.2552	1.5
b	RNFL	0.09	0.5028
c	GC, AC, H/BC, MC	0.108	0.5028
d	OLM	0.02	0.109
e	Rods, Cones	0.04	0.5028
f	RPE	0.01	0.109
g	Choroid	0.04	0.2779
h	Sclera	0.147	0.5028
i	Posterior Tear Film	0.02	1.5
j	Adipose Tissue	0.4253	0.02081
k	Air	-	0
l	Anterior Tear Film	0.02	1.5
m	Cornea	0.2539	0.422
n	Anterior Chamber	0.6427	1.5
o	Lens	3.6883	0.3222
p	Muscle	-	0.26671
q	Bone	-	0.020059
r	Skin	-	0.00020

Table 1 Geometric and electrical properties of tissues, materials in the FE model of a rat head

Here D is the thickness of the structure as measured along the optical axis of the eye. Conductivity is given in Siemens per meter [Andreuccetti et al., 1997; Hasgall *et al.*, 2018].

3.1.1.2. Design considerations and assumptions

It may be noted from Table 1 that the OLM and RPE present as barriers of relatively low conductivity within the layers of retinal tissue, which could significantly impact the distribution

of current density depending on relative locations of the active and reference electrodes. The differentiation of the retina into distinct tissue layers in the geometry of our model would thus provide more meaningful solutions for current density than in the case of the retina being represented by a single layer of uniform conductivity. As even the sub-millimeter resolution of rat MRI may not clearly provide the cellular-level detail needed to represent such distinct tissue layers, the schematic of the rat eye as in Figure 13 provides a necessary reference. It may also be noted that the present work uses a representation of the retinal layers that terminate to a flat edge instead of the gradual tapering that may be seen as these layers form the ora serrata at their junction with the cilliary body. This was done as a means of minimizing computational cost associated with such a tapering off of multiple tissue layers in the geometry, though the relatively small size of this histological feature in relation to the other ocular structures means it should have little impact to the final results of the simulation.

Consistent with precedent work [Doslak et al., 1980; Job et al., 1999; Selner et al., 2018], it is assumed the electric fields are quasi-static and that all ocular tissues are passive conductors with isotropic conductivity [Pavselj et al., 2005; Cindric et al., 2018; Selner et al., 2018]. At low frequencies, neglecting the magnetic induction is considered appropriate in approximating the electric field in biological tissue [Nunez and Srinivasan, 2009],

As noted in section 2.5, openings in the skull can significantly affect the propagation of electric fields throughout the head because the skull has relatively low conductivity and the tissues passing through these openings have relatively high conductivity. As such the nasal cavity, optic foramen, spheno-palatine foramen, alisphenoid canals and intraorbital fissures were all considered key features in to include in the geometry.

3.1.1.3. Application of Maxwell's Equations

Neglecting the time derivative of magnetic flux, Faraday's Law (Equation 5) reduces to:

$$\nabla \times \{E\} = 0 \qquad \text{(Equation 9)}$$

from which it follows that:

$$\{E\} = -\nabla V \qquad \text{(Equation 10)}$$

where V=electric scalar potential. In the time-varying electromagnetic field governed by Equations 4,6,7 and 9, the electric and magnetic fields are uncoupled. As only the electric solution is of interest, the constitutive equations for the electric field become:

$$\{J\}=[\alpha]\{E\} \qquad \text{(Equation 11)}$$

$$\{D\}=[\varepsilon]\{E\} \qquad \text{(Equation 12)}$$

Here, $[\sigma] = \begin{bmatrix} \frac{1}{\rho_{xx}} & 0 & 0 \\ 0 & \frac{1}{\rho_{yy}} & 0 \\ 0 & 0 & \frac{1}{\rho_{zz}} \end{bmatrix}$ is the electrical conductivity matrix,

and $$[\varepsilon] = \begin{bmatrix} \varepsilon_{xx} & 0 & 0 \\ 0 & \varepsilon_{yy} & 0 \\ 0 & 0 & \varepsilon_{zz} \end{bmatrix}$$ is the permittivity matrix,

where ρ_{xx}, ρ_{yy} and ρ_{zz} are the resistivity in the x-, y- and z-directions respectively, and similarly ε_{xx}, ε_{yy} and ε_{zz} are the permittivity in the x-, y- and z-directions respectively.

Substituting constitutive Equation 11 and Equation 12, continuity Equation 8, and considering Equation 10, one can derive the electric scalar potential as:

$$-\nabla \cdot ([\sigma]\Delta V) - \nabla \cdot \left([\varepsilon] \nabla \frac{\partial V}{\partial t} \right) = 0 \qquad \text{(Equation 13)}$$

Neglecting the time-variation of electrical potential, as in a quasi-static assumption, yields the equation:

$$-\nabla \cdot ([\sigma]\Delta V) = 0 \qquad \text{(Equation 14)}$$

Equation 14 was used in FE simulations run in ANSYS 14.5 and solved at every node. Conductivity, in Siemens per meter (S/m), was obtained from literature, as noted in Table 1. With regards to convergence, electric potentials were compared after iterative mesh refinements until results deviated by less than 3% between refinements.

3.1.1.4 Element definition

The model was then imported from SolidWorks to ANSYS (Ansys Inc., Canonsburg, PA) for simulations. Discretization of the 3-D volume of the model and mesh refinement were defined to facilitate convergence while achieving satisfactory spatial resolution in the solution (predicted current density).

Elements were defined with 10 nodes and voltage (u) as the 1 degree of freedom (DOF) and four integration points. This element conforms well with the curved boundaries such as those in the present model geometry. The resulting model is comprised of over 100k tetrahedral elements (Figure 15). The tetrahedral element is described by the shape function:

$$u = u_I(2L_1\text{-}1)L1 + u_J(2L_2\text{-}1)L_2 + u_K(2L_3\text{-}1)L_3 + u_L(2L_4\text{-}1)L_4$$
$$+ 4u_ML_1L_2 + u_NL_2L_3 + u_OL_1L_3 + u_PL_1L_4 + u_QL_2L_4 + u_RL_3L_4$$
$$V = V_I(2L_1\text{-}1) + \ldots \text{ (analogous to } u)$$

where (L1 thru L4) are volume coordinates defined by the ratio of volume of a tetrahedron defined by a point inside the element and the faces of the element.

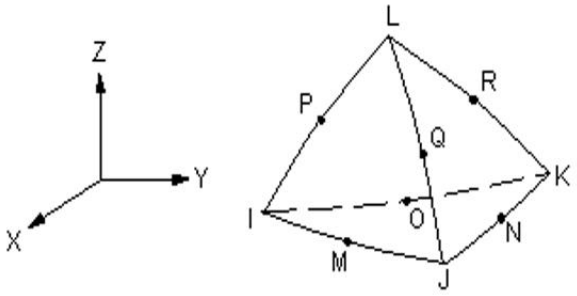

Figure 15. Tetrahedral element in ANSYS.

Figure 15. Tetrahedral element in ANSYS. The element is defined with 10 nodes (I thru R). Reprinted with permission, Ansys Inc.

3.1.2. Validation

3.1.2.1. Animals

Twelve P23H transgenic rats (line 1), aged 6 to 11 weeks, were used for validation measurements. P23H rats are a transgenic model of retinitis pigmentosa (RP) [Machida et al., 2000], and RP has been targeted as an important clinical area of application for EST [Sehic et al., 2016]. The rats were sacrificed using CO_2 asphyxiation, with or without first being anesthetized with 0.2mL ketamine and 0.025mL xylazine per 100 gram bodyweight, depending on prior usage in unrelated experiments. All measurement sessions were carried out within three hours of sacrifice.

3.1.2.2. Electrode placement

Voltages were measured at eight standard locations (Figure 16) via a needle electrode connected to a physiological amplifier (Grass P511, Astro-Med Inc., Warwick, US) with passband of 0.3-3kHz. The measuring electrode (E2-48, Astro-Med Inc., Warwick, US) was modified by applying a coating of insulating acrylic followed by abrasion of the tip with fine sandpaper, resulting in a point electrode which could be inserted at desired subdermal measurement locations. Four measurement locations were 1cm apart along the midline of the head with location 2 placed on the midline between the eyes, and at two locations below each eyelid (Figure 1 6). Skin at each measurement location was punctured with an 18 gauge hypodermic needle to ease insertion of the measuring electrode to the subdermal locations.

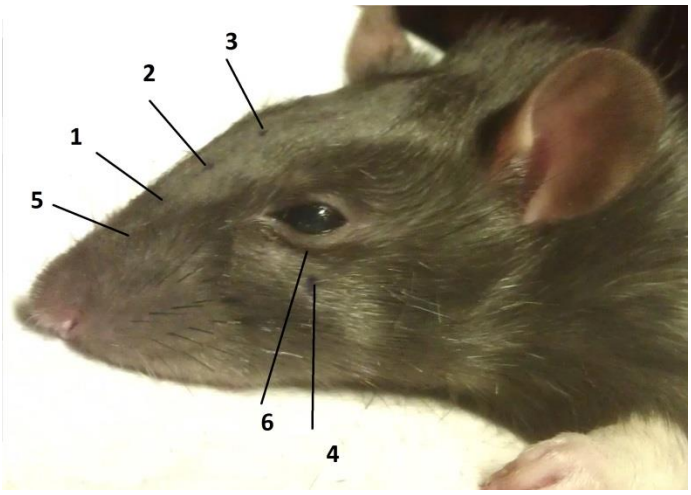

Figure 16. Measurement locations for validation experiments.

Figure 16. Measurement locations for validation experiments. Rat with subdermal electrode measurement points marked. Locations 7 and 8, analogous to 6 and 4, respectively, are below the opposite eye and thus obscured from view.

3.1.2.3 Measurement protocol

Measuring electrodes were inserted subdermally. Measurements were made at each of eight locations in sequence, and the sequence repeated 2-3 times. Measurement locations are labeled in Figure 16. WES was the chosen protocol for these measurements, as our facility has experience with this technique (Rahmani et al., 2013). Current was delivered via an active Ag/AgCl pellet electrode disc (1.5mm diameter) placed in contact with the cornea via a layer of commercially available artificial tear solution at the area of contact. A second, cylindrical pellet electrode (1mm dia. x 2.5mm long), coated with commercially available conductive gel, was placed in the mouth between the jaw and cheek and served as reference. The artificial tears and conductive gel ensured proper contact and consistent impedance at the electrode-tissue interface. EST of 10μA RMS at 1kHz (sinusoidal waveform) was delivered using a waveform generator (BK Precision 4011) modified to deliver constant current (Rahmani et al., 2013). Impedance between the eye and mouth electrodes was measured at the beginning and end of each

experiment to ensure that the voltage required to drive the desired currents did not exceed the compliance voltage limitation of the waveform generator.

3.1.2.4 Error Function, comparison

An error function was defined to quantify the differences between model predictions and measured potentials. The error function was the root-mean-square error (RMSE) calculated using the equation:

$$RMSE = \sqrt{\left(\sum_{x=1}^{n} \left(V_{(simulated,x)} - V_{(measured,x)} \right)^2 \right) / n} \qquad \textbf{Equation 15}$$

where n is the number of measurement locations (n =1 to 8), $V_{(simulated,x)}$ is the potential evaluated at each location *x* from simulation and $V_{(measured,x)}$ is the average potential at the same location *x* as measured experimentally across all twelve animal specimens.

We also wished to quantify the apparent variability between measurements from different animals. Thus the RMSE was also calculated between the potentials measured in each individual animal versus the average values at each measurement point across the remaining eleven animal specimens, referred to as $RMSE_A$ using Equation 16,

$$RMSE_A = \sqrt{\left(\sum_{y=1}^{n} \left(V_{(measured,A)} - V_{(measured,y)} \right)^2 \right) / n} \qquad \textbf{Equation 16}$$

where n is the number of measurement locations (n =1 to 8), $V_{(measured,A)}$ is the average potential evaluated at each location in an individual animal y and $V_{(measured,y)}$ is the average potential measured at each location across the remaining animals. This leave-one-out method was considered a metric to evaluate inter-animal variability in the empirical measurements.

As discussed in Section 3.2.2., muscle conductivity was chosen as the sole free parameter in the model optimization. The muscle conductivity value started with the value of .2667 S/m obtained from literature [Hasgall et al., 2018] and was manually altered in a progressive staircase search until a minimum value of RMSE per (Equation 15) was determined.

3.2. Results

3.2.1. Initial model results

The idealized "muppet" model with detailed retinal layers as described earlier was discretized, as seen in Figure 17A and the model solved as seen in Figure 17B. Results were then noted for comparison with measured potentials from analogous locations on rat specimens exposed to EST using the WES configuration. A comparison of those measured potentials vs. these early model results is plotted in Figure 17C.

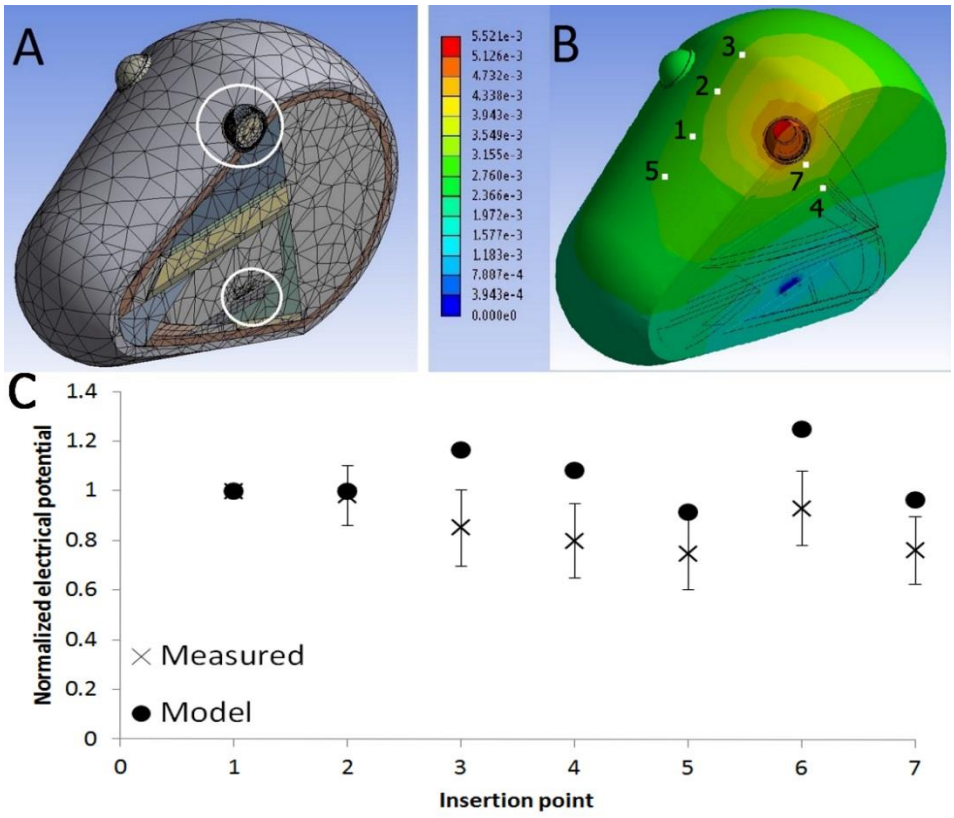

Figure 17 Electric potential in WES, measured vs. model using simplified rat head geometry

(A) Cross-sectional view, showing meshed model, white circles indicating electrode positions. (B) Contour plot of voltage, white dots marking measurement sites used in model validation. (color scale max.: 5.521e-3V, min.: 0V) Note that point 7 is on the opposite eye, obscured from this view. (C) Normalized potential per location. Measured potentials were averaged from multiple readings at each location. Note the same general trend seen in both measured and model (simulated) potentials.

3.2.2. Sensitivity of the model to changes in conductivity

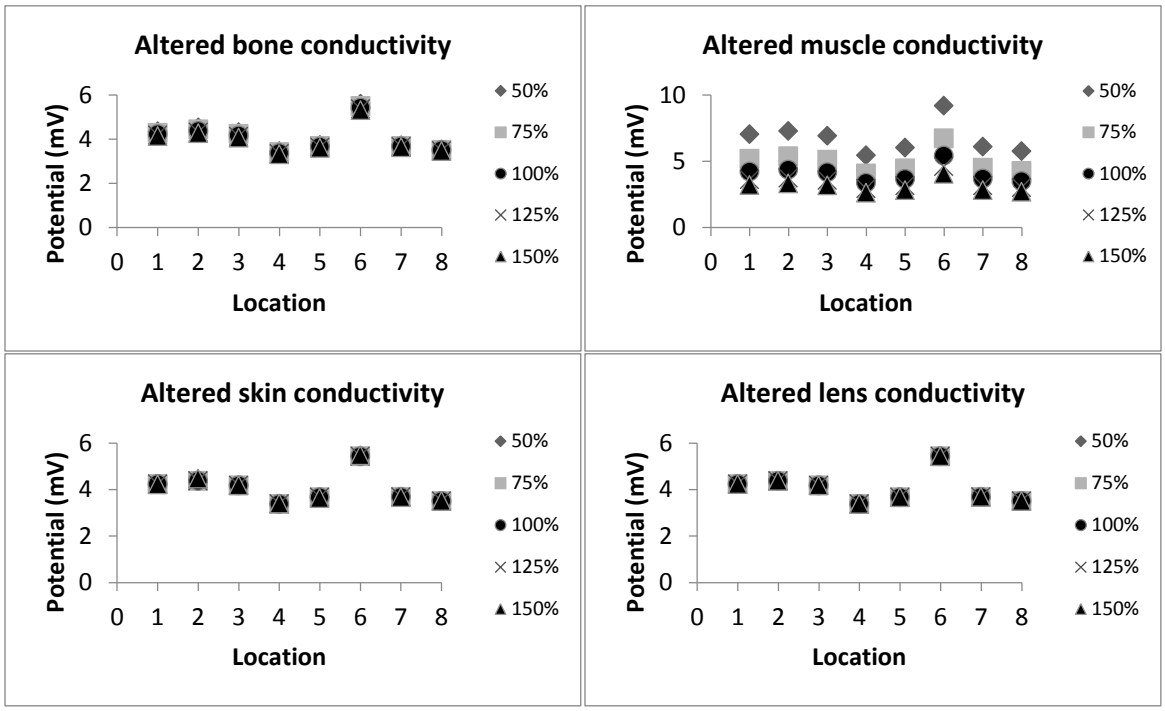

Figure 18. Effects of altering conductivity in tissues.

Figure 18. Effects of altering conductivity in tissues. Conductivity values were altered to increments of 50%, 75%, 125% and 150% in reference to literature values (at 100%) in bone, muscle, skin and lens tissues respectively, while holding all other tissues at literature values. Model results (mV) are plotted vs. location, where locations correspond those shown in Figure 17B.

Sensitivity of the model, with more detailed geometry, to changes in muscle, skin and bone conductivity values can be seen in Figure 18, which plots potentials predicted by the mode at locations as marked in Figure 17B. The effect of changes in the conductivity values of ocular tissues and adipose on potentials predicted by the model of a rat eye has been previously reported [Selner et al., 2018], nonetheless changes in lens conductivity were also included as a representative example. For each of these tissues, the model was run at 50%, 75%, 100%, 125% and 150% increments of the literature value for conductivity of that tissue while keeping all other tissues at literature value. The root mean squared error (RMSE) between potentials at each

increment and the 100% value for each tissue was found. The RMSE was found to be .0737, 1.3059, .0003 and .0101 mV for bone, muscle, lens and skin respectively. By this metric, variation in muscle tissue showed the greatest effect on the model. Therefore, muscle conductivity was chosen as the sole free parameter in the subsequent optimization process.

3.2.3. Validation measurements

	Measurement point							
	1	2	3	4	5	6	7	8
Animal 1	49.14	46.31	41.84	0.00	37.74	54.33	36.91	-
Animal 2	36.68	30.83	27.34	25.17	22.25	33.52	25.46	22.91
Animal 3	31.63	28.76	25.74	28.57	20.36	30.16	-	-
Animal 4	23.62	18.34	18.10	14.14	15.34	24.04	14.57	14.00
Animal 5	28.05	26.35	24.70	21.80	21.35	27.44	-	-
Animal 6	27.81	32.81	14.50	14.50	18.17	21.00	22.91	15.91
Animal 7	24.47	21.59	16.97	22.70	15.17	20.44	-	-
Animal 8	30.69	33.16	30.79	30.17	17.85	18.03	15.41	15.08
Animal 9	36.42	38.89	36.65	33.52	35.71	40.48	31.71	31.64
Animal 10	39.07	41.01	36.66	34.08	36.59	40.48	33.66	31.11
Animal 11	41.90	45.96	41.96	37.30	36.66	38.89	34.58	34.37
Animal 12	39.83	40.84	40.13	29.27	36.06	38.54	37.12	34.08
Mean	34.11	33.74	29.62	24.27	26.11	32.28	21.03	16.59
Std. dev.	7.71	9.10	9.90	10.56	9.46	10.75	14.74	14.17

Table 2 Peak to peak measurements of potentials

Mean RMS values (in mV) of peak-to-peak potential at each measurement point, shown per experiment date.

As an indicator of inter-animal variability in the empirical measurements reported in Table 2, the average RMSE value from Equation 16 was 57.1mV. Early work with the model yielded an RMSE per Equation 15 of 51.22mV, i.e.: error between simulated and average measured potentials was lower (by 10%) than the mean inter-animal variability. Optimization that followed, as reported below, minimizes the error in model vs. measured potentials.

3.2.4. Optimization in detailed model

Progressing to the more detailed, "Remy" model, a staircase approach was taken to find the muscle conductivity value that produces minimal error between measured and modeled potentials.

A.

Factor	Conductivity (S/m)	RMSE
1	0.2667	23.81
(1/5)	0.0533	14.30
(1/10)	0.0267	5.69
(1/15)	0.0178	6.02
(1/20)	0.0133	12.30

B.

Factor	Conductivity (S/m)	RMSE
(1/7)	0.03810	10.43
(1/8)	0.03334	8.72
(1/9)	0.02963	7.12
(1/11)	0.02425	4.76
(1/12)	0.02223	4.29
(1/13)	0.02052	4.42
(1/14)	0.01905	5.02

Table 3 RMSE values for iterations of muscle conductivity

A. RMSE as found via Equation 15, from initial iterations using factors of 1/5 to change muscle conductivity. **B.** RMSE as found from subsequent iterations, changing muscle conductivity by incremental factors.

Muscle conductivity values and resulting RMSE values are given in Table 3. The minimum RMSE value was obtained when muscle conductivity was equal to 0.02223 S/m; this conductance value was then adopted for all further simulations.

3.2.5. Results from detailed model

Measurement locations are marked in Figure 19A and compared with predicted potentials using the more detailed model as seen in Figure 19B. A subset of the simulation results referred to in Table 3c is plotted in Figure 19C.

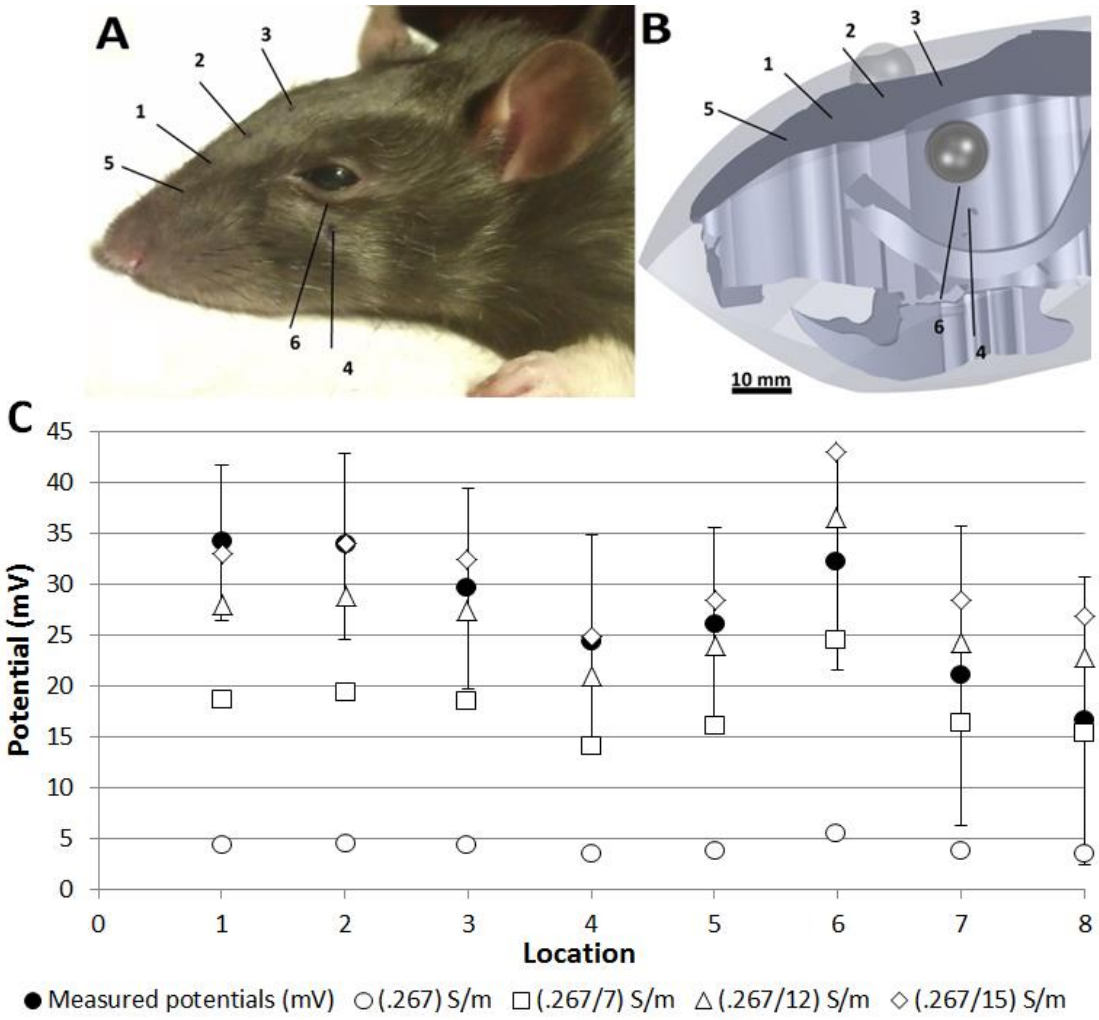

Figure 19. Electric potential, measured vs. model.

Figure 19. Electric potential, measured vs. model. (A) Rat with subdermal electrode measurement points marked. Locations 7 and 8, analogous to 6 and 4, respectively, are below the opposite eye and thus obscured from view. (B) Model with measurement points labeled, with skin, muscle and adipose tissue rendered transparent to better illustrate the measurement locations relative to the skull. (C) Measured and simulated potentials. Locations plotted along x-axis correspond to points as labeled in panels A and B. Potentials measured experimentally are plotted with filled circles (●). Simulations are plotted for four values of muscle conductivity as also referenced in Table 3: (0.267) S/m (○, starting value from literature), (0.267/7) S/m (□), (0.267/12)S/m (△), and (0.267/15) S/m (◇).

3.3. Discussion

3.3.1. Summary

Twelve P23H transgenic rats (line 1), aged 6 to 11 weeks, were used for validation measurements. Table 2 shows the average potential measured at each location marked in the photograph in Figure 19, for individual animals as noted by experiment date. Table 2 also condenses this data to a mean and standard deviation at each of the noted measurement points.

Early simulations were run using the simplified "muppet" model shown in Figure 17A. The locations denoted in Tables 2A and 2B are analogous to the locations correspondingly numbered in the model results view shown in Figure 19B. These early simulations provided the "Model" results normalized and plotted in Figure 17C, while the data in Table 2c is normalized and plotted as the "Measured" potentials in Figure 17C. This early work provided a profile of electric potentials, albeit with wide standard deviation seen in the measured potentials. Though this reflects differences in potentials measured from one individual animal to the next, the profile of potential values as seen in Fig.17C largely remains the same, differing by some scalar value across all measurement locations for a given animal.

As noted earlier, conductivity values within the eye were recently validated in a similar model used to evaluate electroretinograph field potentials [Selner et al., 2018], and so were not included in the optimization process here. As reference, the lens occupies .09% of the total model volume. Bone tissue occupies approximately 18% of the head volume, yet has a relatively low conductivity (an order of magnitude below muscle), and effectively acts as an insulator in this context. Similar to bone, skin tissue occupies approximately 17.5% of the head volume, has a relatively low conductivity and effectively acts as an insulator in this context. Muscle tissue

occupies approximately 64% of the head volume, and is known to undergo significant conductivity changes with time post-mortem [Zheng et al., 1984; Martinsen et al., 2000; Roth et al., 2006]. These temporal changes may account, in part, for variability in the impedance values reported across literature, and may have affected the *in situ* measurements of electrical potential used for validation of this model (see below). Furthermore, incremental changes to muscle conductivity yielded the largest RMSE in the model results, which are plotted in Figure 18. Therefore, muscle conductivity was the sole free parameter in the optimization process.

The RMSE, i.e: error in measured vs. model at different iterations of muscle conductivity is reported in Table 3, where Table 3a shows conductivity divided by factors of 5, showing a minimum at 1/10. Table 3b shows RMSE result from subsequent finer iterations, giving a minimum at 1/12. This suggests an over ten-fold decrease in muscle conductivity as compared to the literature value.

3.3.2. Limitations

The sources of variability in the measured potentials may include sub-optimal electrode placement over the course of the experiments. This might be remedied by more precise placement at each location via stereotaxic frame. Multi-channel data acquisition, making measurements at all locations simultaneously would also be desirable, as significant time is spent moving the recording electrode from position to position during which the post-mortem tissue electrical properties can change. Tissue conductivity has been shown to be affected by onset of rigor [Zheng et al, 1984; Martinsen et al, 2000; Cui et al, 2010], it is also shown that the onset of rigor is accelerated by the application of an electric current [Roth et al., 2006], and this combination of factors may lead to the over ten-fold decrease in conductivity of the muscle

tissue suggested by the factor of (1/12) yielding the minimum RMSE between measured and modeled potentials. This is an admittedly large departure from the literature value and makes validation measurements in live animals all the more desirable.

3.3.3. Conclusions

Early results from an idealized "muppet" model geometry as well as the more detailed "Remy" model geometry were presented here. Some variability in the measured potentials and a scalar factor of (1/12) in muscle conductivity are notable in the model and the measurements taken to validate and optimize it. Some attempt has been made to explain these aspects, as well as suggestions for future work.

The rat head model presented here includes anatomical detail at several size scales (tens of microns to centimeters), both necessary and sufficient to predict current density at the level of the retina resulting from practical EST electrode configurations. A single model parameter (muscle conductivity) was optimized by comparing to empirical measurements made at several locations during WES current delivery; residual error between model and measurements was below inter-animal variance in the measurements.

The resulting model can serve as a baseline for objective comparison of other electrode shapes and configurations, as will be discussed in the following section.

4. Specific Aim 2 – Predict current density at the retina from different EST electrode configurations.

4.1. Methods

4.1.1. Representative electrode configurations

As described in Section 3, a detailed model of the rat skull was constructed using Greene's widely referenced illustrations [Greene, 1959]. While early simulations to compare the different electrode configurations were conducted with the idealized "muppet" model, subsequent simulations were later run on the more detailed, "Remy" model. For this more detailed model, orthogonal section views representing the sagittal, coronal and axial anatomical planes were extrapolated and sculpted to arrive at a three-dimensional representation of the rat skull in SolidWorks. The optic foramen, spheno-palatine foramen, alisphenoid canal and intraorbital fissure were represented in this model, as these were considered significant features that would affect the electric field distribution from an exogenous current source, as described in previous sections. Muscle tissue, skin and a detailed eye model were then applied to this initial skull structure. This geometry was then imported to ANSYS for simulations. Validation, optimization and a measure of sensitivity of the model to changes in conductivity values were also discussed in Section 3. The muscle conductivity value which provided the lowest RMSE, .02223S/m, was the applied muscle conductivity in these simulation runs. As previously described, one eye in the model was taken to be the target of simulated EST and was defined with a high level of detail including all the layers as previously described and listed in Table 1. It was to this base geometry that the different electrode configurations were applied for comparison.

Three distinct electrode geometries used to investigate EST in rats have been represented in the model, as illustrated in Figure 20. Whole-eye stimulation (WES, Figure 20A) uses Ag/AgCl pellet electrodes placed at the cornea and mouth [Rahmani et al., 2013]. Transcorneal electrical stimulation (TES, Figure 18B) uses concentric gold ring electrodes incorporated into a contact lens [Morimoto et al., 2005, 2007, 2010, 2012]. Subretinal electrical stimulation (SES, Figure 20C) includes parallel plate electrodes on opposing sides of a silicon chip implanted in the subretinal space [Pardue et al., 2005]. In the model, only one electrode configuration is present during each simulation. Electrode surfaces are assigned as current sources or sinks, and were assigned conductivity of silver 6.3×10^7 S/m (WES) or gold: 4.1×10^7 S/m (TES, SES) as appropriate [Serway, 1998; Griffiths, 1999]. Electrode dimensions were assigned to closely match those used in the respective empirical studies described in the literature (see Figure 20 legend). Assigning a constant, time-invariant current input as the applied load (active electrode surface) and a boundary condition of zero volts at the reference electrode surface, the potential at each node was solved using Maxwell's equations in ANSYS Engineering Analysis System 14.5, Windows x64 version.

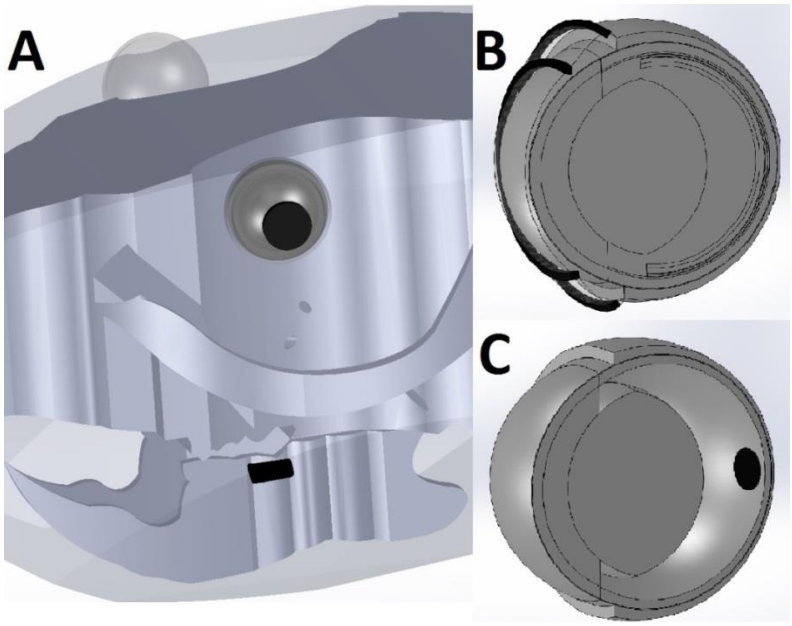

Figure 20. Rat head geometry with different electrode configurations.

Figure 20. Rat head geometry with different electrode configurations. Electrodes marked in black. (**A**) WES with electrodes placed on cornea and in the mouth, as described in Rahmani et al. 2013. (**B**) Cross-section of rat eye with concentric ring electrodes on the cornea, as employed for TES using the "Kyoto lens"; electrode locations and dimensions as per Morimoto et al. 2005. (**C**) Cross-section of rat eye with subretinal electrodes (opposing surfaces of the disk) used in SES (the retina is rendered transparent in this view); electrode locations and dimensions as per Pardue et al., 2005.

4.1.2. Electrode configurations as applied to diseased vs. healthy states

Because retinal EST is generally intended for patients (and animal models) with retinas that have experienced cell loss, and specifically photoreceptor loss in retinitis pigmentosa, this condition was also implemented in the model for some simulations. Photoreceptor loss disrupts the outer limiting membrane, which is a high-resistance layer in the healthy retina. A degenerated state of the retina was approximated by applying the conductivity value of the adjacent cell layer (GC, AC, H/BC, MC) to the OLM layer. This is consistent with recent measured resistance profiles of rd1 mouse retina (significant photoreceptor loss) [Wang and Weiland, 2015].

4.2. Results

4.2.1. Spatial profiles of current density

Early simulations using the "muppet" model showed distinct profiles of current density distribution along the retina afforded by the different electrode configurations, as plotted in Figure 21.

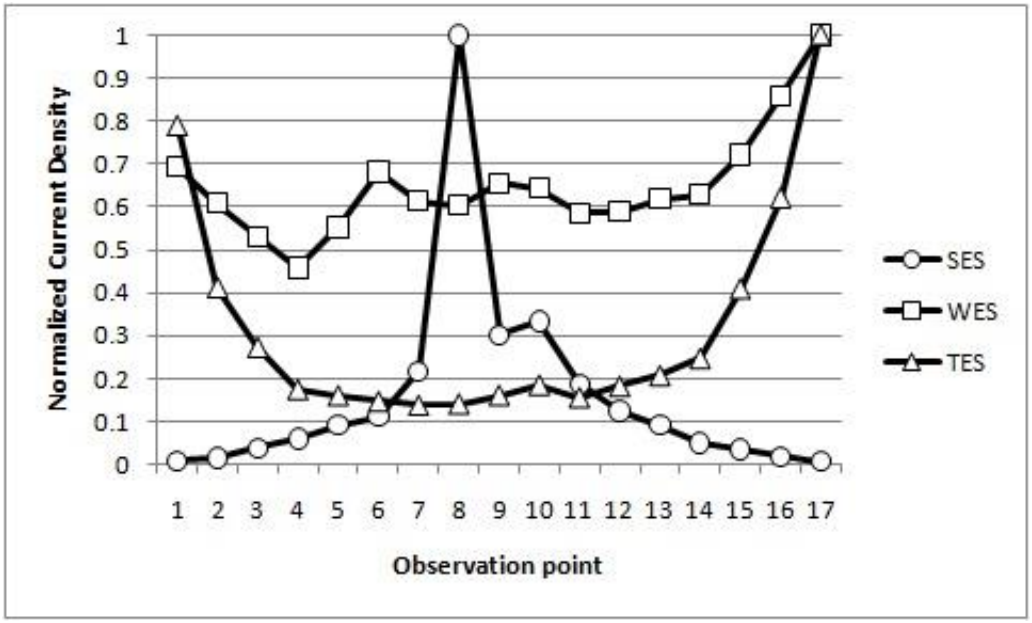

Figure 21. Current density profiles using simplified rat head geometry.

Figure 21. Current density profiles using simplified rat head geometry. Normalized, simulated potentials from observation points along the retina for the three electrode configurations. With each configuration, current density was normalized to the maximum value to provide a comparison of the spatial distribution of current density across the retina. Points 1 and 17 correspond to points at the ora serrata on opposite sides of the retina, with the remaining points equally spaced along a line between them, bisecting the retina.

Using the more detailed, "Remy" model of the rat head, current density values were evaluated at seven locations across one arc through the retina at the inner (vitreal) surface of the photoreceptor layer, as illustrated in Figure 22A. Current density values were evaluated in a nasal-temporal direction normal to the surface of the retina at each location. The resulting

values, along with summary statistics, are given in Table 4. Note that the mean current density provided by the SES electrode configuration is orders of magnitude lower than that obtained with WES and TES. To help visualize the spatial distribution of retinal current density, the values of Table 4 were normalized, and plotted together vs. retinal location in Figure 22B.

To evaluate the influence of advanced retinal degeneration, specifically photoreceptor loss, on the distribution of retinal currents, the low-conductivity OLM was assigned the relatively higher conductivity of the neighboring cell types, and the current densities evaluated at the seven locations indicated in Figure 22A. Figure 22C-E plot the current densities for healthy and degenerate retina for WES, TES and SES, respectively (values provided in Table 4).

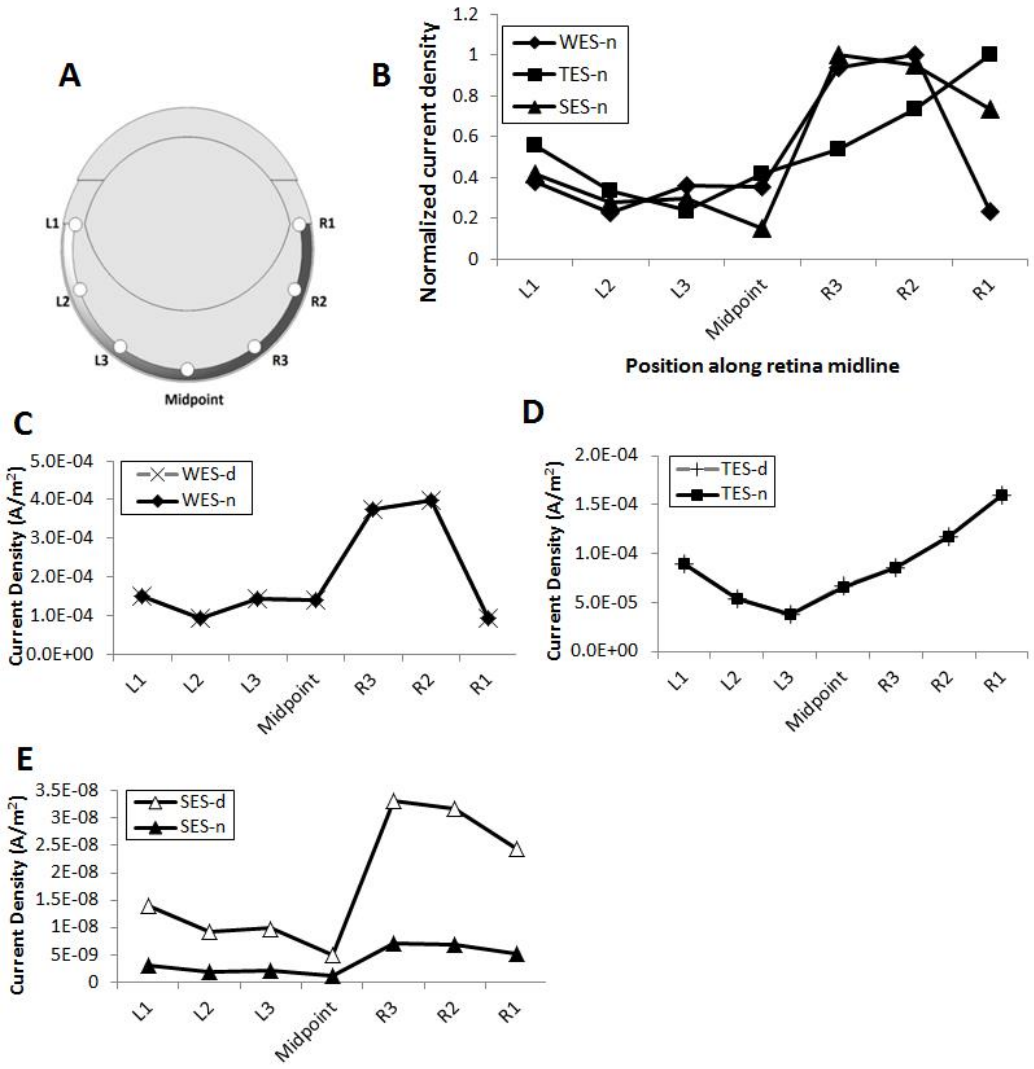

Figure 22. Distribution profiles of current density at the retina, healthy vs. diseased states.

Figure 22. Distribution profiles of current density at the retina, normal vs. diseased states. (A) Current density evaluation points along the retina, for comparing different electrode geometries. L1 and R1 correspond to points at the ora serrata, while L2, L3, R2 and R3 are equally spaced points between the ora serrata and the midpoint. All evaluation points are nodes within the photoreceptor later of the model. (B) Normalized current density at observation points along the retina for the three electrode geometries. For each geometry, current density was normalized to the maximum value to provide a comparison of the spatial distribution of current density across the retina. (C), (D), (E) Comparison of normalized current density in normal (-n) versus diseased (-d) condition for WES, TES and SES respectively.

Location on Retina	WES-n	WES-d	TES-n	TES-d	SES-n	SES-d
L1	1.51E-04	1.51E-04	8.90E-05	8.90E-05	3.02E-09	1.39E-08
L2	9.12E-05	9.14E-05	5.39E-05	5.39E-05	2.00E-09	9.22E-09
L3	1.44E-04	1.44E-04	3.79E-05	3.79E-05	2.13E-09	9.83E-09
Midpoint	1.40E-04	1.40E-04	6.63E-05	6.66E-05	1.09E-09	5.02E-09
R3	3.74E-04	3.74E-04	8.55E-05	8.55E-05	7.18E-09	3.31E-08
R2	3.97E-04	3.97E-04	1.17E-04	1.17E-04	6.86E-09	3.16E-08
R1	9.34E-05	9.34E-05	1.59E-04	1.59E-04	5.28E-09	2.44E-08
Mean	1.98E-04	1.99E-04	8.70E-05	8.71E-05	3.94E-09	1.82E-08
Std. dev.	1.30E-04	1.30E-04	4.10E-05	4.10E-05	2.48E-09	1.14E-08
Coefficient of Variation	1.53E+00	1.53E+00	2.12E+00	2.12E+00	1.59E+00	1.59E+00

Table 4 Current density across retina, normal vs. diseased during EST in rat model

Current density (in A/m^2) at seven locations across the retina (Figure 19A) for each electrode configuration in normal (WES-n, TES-n, SES-n) and degenerate (WES-d, TES-d, SES-d) models.

Color contour plots of current density for each EST electrode configuration are shown in Figure 23 at all locations across the photoreceptor layer, providing maps with fuller view of the spatial distribution of current density.

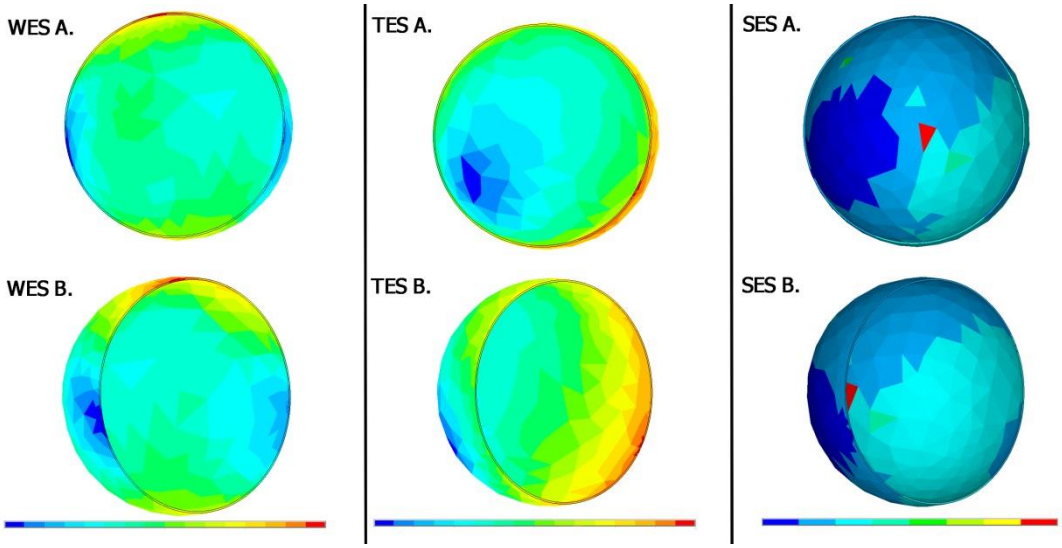

Figure 23 Element solution, current density at the retina from different electrode configurations.

Figure 23. Element solution, current density at the retina from different electrode configurations. The photoreceptor layer is shown here with color contour map, scale ranging from red at maximum ($6.74x10^{-4}$ A/m^2, $1.82x10^{-4}$ A/m^2 and $9.0x10^{-8}$ A/m^2 for WES, TES and SES respectively) to blue at minimum ($8.4x10^{-6}$ A/m^2, $5.550x10^{-6}$ A/m^2 and $4.81x10^{-9}$ A/m^2 for WES, TES and SES respectively). For each geometry, the view A shows the perspective when looking directly into the retina and view B has the layer rotated off-center to better show the peripheral edges. Each view represents over 5k solutions, with the left and right sides corresponding to the nasal and temporal directions respectively.

4.3. Discussion

4.3.1. Summary

Results were presented for the three representative electrode configurations. Of note is the marked asymmetric non-uniformity in retinal current density resulting from WES and SES, both of which distinctly peak off-center and appear to be influenced by the foramina in the skull (local areas of high conductivity). TES results in a more symmetric non-uniformity, with peaks near the margins of the retina; this is consistent with the corneal positions of the active and return electrodes. A perfectly symmetric field distribution with uniform current all along the peripheral retinal is not achieved despite the use of symmetric ring electrodes, possibly due to underlying skull morphology.

Absolute and relative current densities were reported for models representing normal and degenerate retina. The significant change in OLM conductivity in the approximation of a diseased state had no observable effect on WES or TES. For SES, the current density at each evaluation point increased in the absence of the low-conductivity OLM. This appears to reflect

an increase in current passing through the inner retina (current density values were evaluated at the inner margin of the photoreceptor layer, adjacent to the OLM).

4.3.2. Limitations

The subdermal locations chosen for empirical measurements of voltage during EST may have limited relevance to the electric fields in deeper tissues that are more relevant to predicting currents at the retina such as locations marked in Figure 22A. This is particularly made evident by the comparison of healthy vs. disease states with SES (Figure 22E), where both active and reference electrodes positioned in retinal tissues appears to result in an electric field distribution more influenced by the differences in retinal layer conductivities as compared to the WES and TES configurations. Potential measurements made at precise locations closer to, and within, the eye via a stereotaxic frame would be required for further model refinement. As mentioned in Section 3, making measurements at all locations simultaneously would also be desirable, as significant time is spent moving the recording electrode from position to position, during which the post-mortem tissue electrical properties can change. Muscle conductivity as determined from the methods described in Section 3 is a key factor in determining absolute values in potential one can expect to measure from the different electrode configurations, and as such validation measurements from live animals are all the more desirable.

4.3.3. Conclusions

Magnitude and distribution of retinal current density appears to be influenced by electrode configuration and anatomy. For a given controlled-current stimulation level, WES (also called monopolar TES in many laboratories) resulted in the highest average current densities compared to TES and SES. The current density distribution at the retina during WES

appeared strongly influenced by gross anatomy, specifically the foramen representing high conductivity current paths through the skull between the active and return EST electrodes, resulting in significantly higher current density in the temporal retina.

It is notable that current densities in WES and TES seemed unaffected by changes to the OLM conductivity (Figure 22C, D). This suggests treatment protocols using these electrode configurations may be not be affected by the stage of disease progression in the subjects, which is a useful consideration in the design of EST protocols.

Per Figure 23, TES protocol appears to concentrate current density at the periphery of the retina whereas SES localizes the current density to the region immediately surrounding the subretinal implant. This suggests the TES and SES protocols should be chosen for peripheral or localized EST delivery respectively.

Recent reviews have tabulated the promise of EST for several conditions that threaten vision [Sehic et al., 2016; Pardue and Allen, 2018], yet comparison across studies is difficult due to the variety of protocols and lack of measurements of current delivery at the retina. The quantitative, objective evaluation of current density across EST electrode configurations reported here is unique, and will assist in generalizing results across studies, and in the design of optimal electrode configurations. The conductivity values used here are generally conserved across mammalian species, the basic approach may now be applied to other mammal models, including human as described in the following section. Results thus obtained may directly inform the design of EST protocols for clinical practice.

5. Specific Aim 3 – Develop a model of the human head and predict current density at the retina during EST.

5.1. Methods

5.1.1. Building geometry of the human head

Similar to the approach described in Section 3 on building the geometry for the rat head, views of the sagittal, coronal and axial anatomical planes were extrapolated and sculpted to arrive at a three-dimensional representation of the a skull in SolidWorks. Photographs were taken of an anatomical reference skull (National Biological Labs, Newington, VA) at the needed orthogonal perspectives. These photographs were then imported to SolidWorks, traced with spline tools and projected out to provide the base structure of a human skull for the simulation geometry, as seen in Figure 24. Muscle tissue, skin and a detailed eye model were then applied to this initial skull structure as seen in Figure 25 and Figure 26. Gross anatomy of the human head was referenced from literature [Wendel et al., 2008; Gray et al., 2003]. This geometry was then imported to ANSYS for simulations.

As with the previously described rat head model, one eye in the model was taken to be the target of simulated EST and was defined with a high level of detail. Gross anatomy of ocular structures was referenced from literature [Oyster, 1999]. As current density and distribution at, and within, the retina are of particular interest, and because conductivities of layers in the mammalian retina vary significantly [Kasi *et al*., 2011; Wang and Weiland, 2015; Loizos et al., 2016], the detailed model eye as shown in Figure 27. included discreet posterior layers.

The retinal layers in the model include: retinal nerve fiber layer (RNFL); combined ganglion cell and inner plexiform layer (GC, IPL), amacrine, horizontal, bipolar and Muller cells

(A, H, B, M), outer limiting membrane (OLM), and the photoreceptor layer (rods, cones). The eye model also includes distinct layers to represent the retinal pigment epithelium (RPE) and choroid. These layers were modeled with uniform thickness to simplify computation. The thickness of each of these layers was based on established literature on the human eye, with a total retinal thickness of 304.4mm [Bagci et al., 2008; LoDuca et al., 2010; Shahidi et al., 2005; Wang et al., 2018; Ban, 2011]. Table 5 lists the thickness (D) of each model layer along the central axis of the eye as well as the assigned conductivity values from literature [Andreuccetti et al., 1997; Hasgall et al., 2018]. The sclera was given a variable thickness, with 1mm at the central axis and tapering to .45mm thickness at the edges [Vurgese et al., 2010; Olsen et al., 1998]. The full assembly of the human head geometry with detailed eye is seen in Figure 28. In order to represent the thinning of retinal ganglion cells as seen in glaucoma patients [Zhang et al., 2014], a second version of the eye with 20% thinner (.056mm) GCL/IPL layer was built as well.

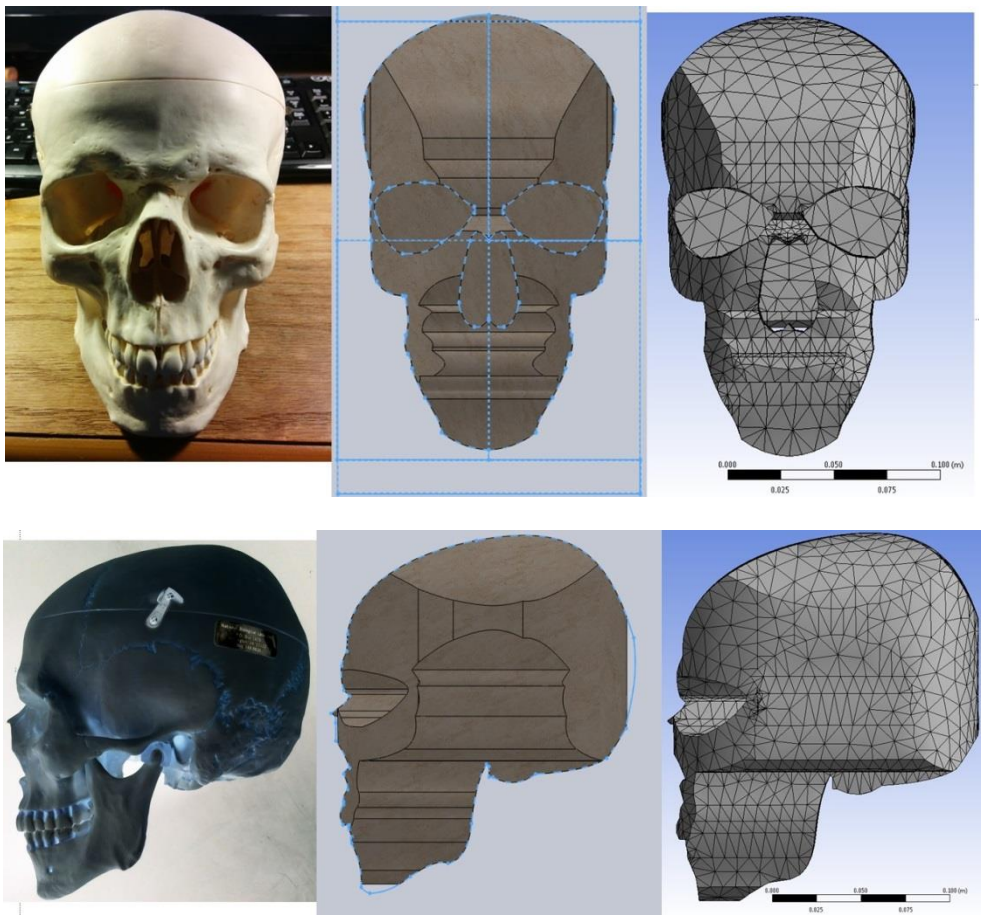

Figure 24. Initial steps in human model construction

Figure 24. Initial steps in human model constructionFront (top row) and sagittal (bottom row) views of model construction. From left to right: photographed human skull replica, solid model via spline trace in Solidworks, meshed model after porting via ANSYS WB.

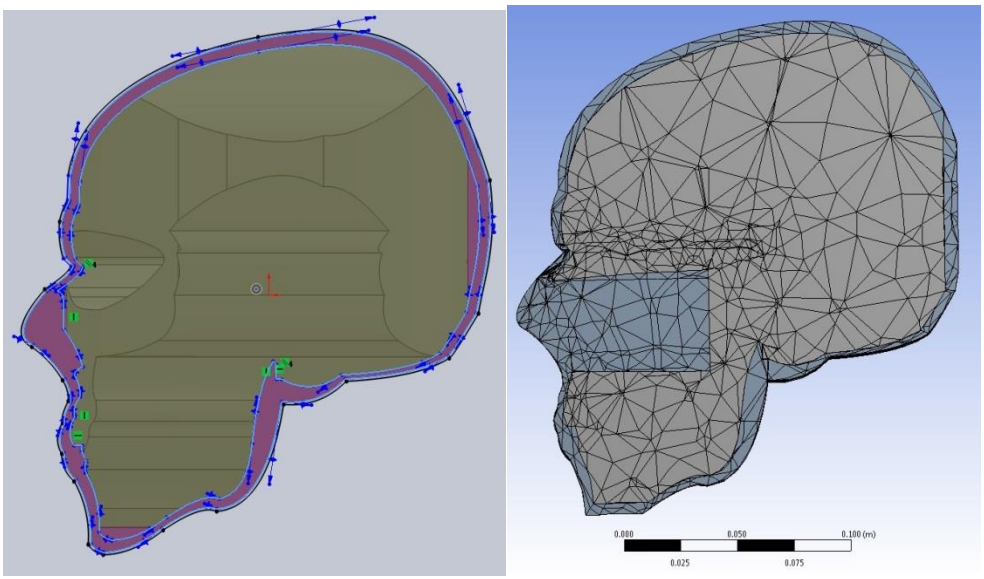

Figure 25. Fleshing out human model, sagittal.

Figure 25. Fleshing out human model, sagittal.Sagittal cross-section views: (left) assembly of fitted muscle and bone layers in Solidworks, (right) meshed model after porting via ANSYS WB.

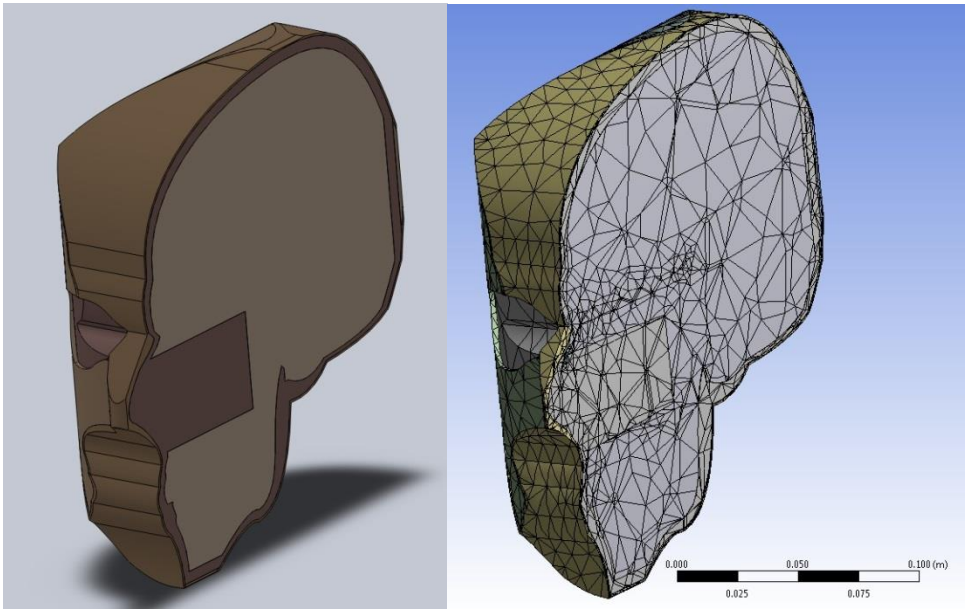

Figure 26. Fleshing out human model, orthogonal.

Figure 26. Fleshing out human model, orthogonal. Oblique cross-section views: (left) assembly of fitted skin, muscle and bone layers in Solidworks, (right) meshed model after porting via ANSYS WB.

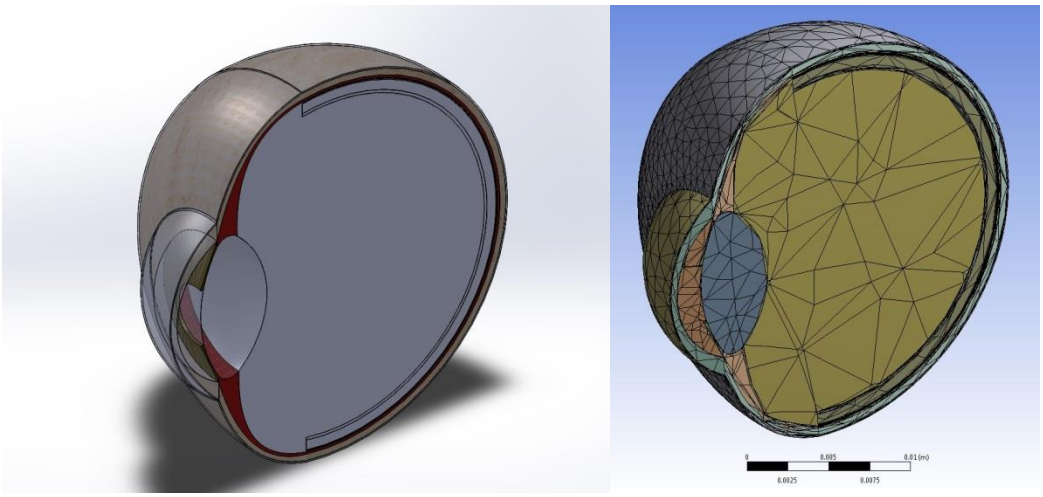

Figure 27. Human eye geometry

Figure 27. Human eye geometry. Human eye assembly in Solidworks with differentiated retinal layers (left), discretized in ANSYS WB (right).

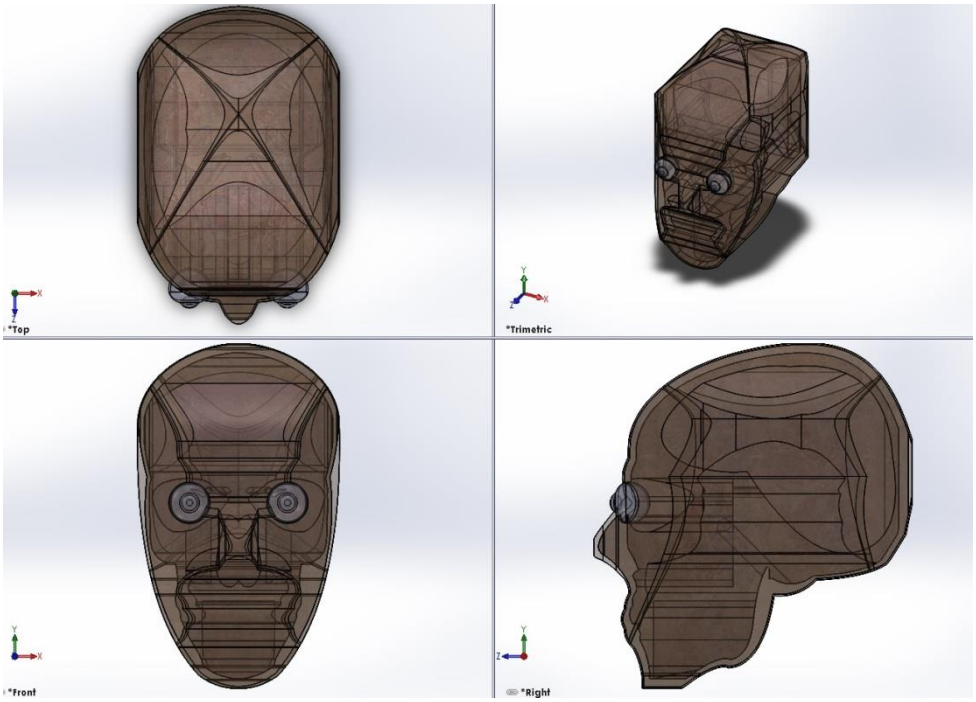

Figure 28 Human head geometry.

Figure 28. Human head geometry. Human head assembly in SolidWorks, orthogonal views, all tissues included (transparent view mode) in Solidworks. Orbital fissures, optic canal implemented.

5.1.2. Electrode configuration

A Dawson-Trick-Litzkow (DTL) electrode with a reference electrode on the ipsilateral temple was chosen as a representative design appropriate for the present study, as this a commonly adopted design in several human studies [Schatz et al., 2011; Naycheva et al., 2013; reviewed in Sehic et al., 2016]. The electrode filament is typically draped on or inferior to the corneal limbus and is represented in the model by a 50μm filament in a 60-degree arc in contact with the sclera, as seen in Figure 29A. The reference electrode is a 10mm disc with 2mm hole representing a typical gold cup electrode (e.g.: LKC Technologies Inc., Gaithersburg, MD).

A second electrode configuration modeled was the ERG-Jet electrode, with a 10mm outer dia., .5mm thick gold film ring electrode inlaid to a polymer contact lens. A 10mm silver disc electrode as reference, placed on the ipsilateral temple, as seen in Figure 29B. This electrode configuration as also been used in several studies of human EST, and the circular shape of the ring electrode has been considered conducive to evenly delivering current to the eye [Xie et al. 2011; reviewed in Sehic et al. 2016].

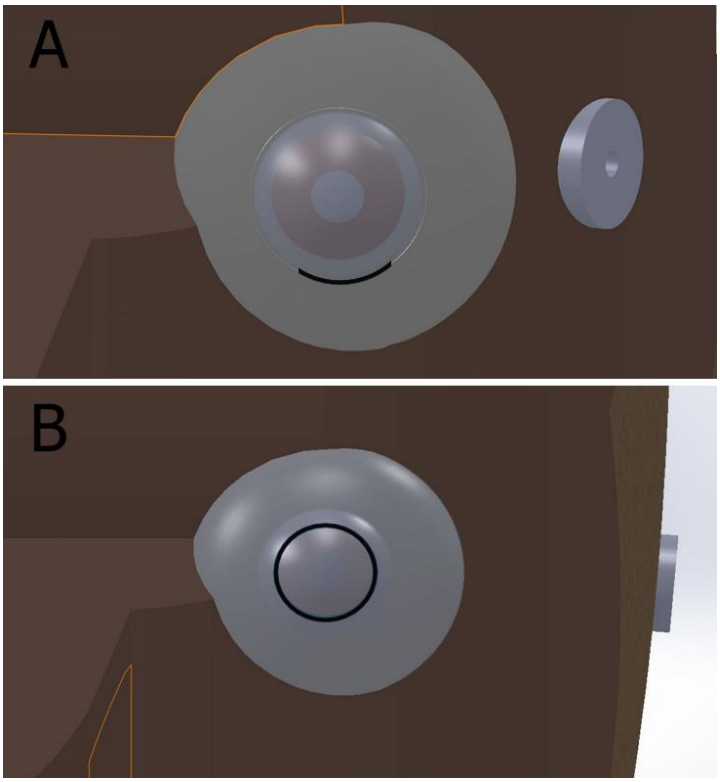

Figure 29 Human head geometry with different electrode configurations

Figure 29. Human head geometry with different electrode configurations. Electrodes marked in black. (A) The DTL electrode, modeled as contacting a 60-degree arc on the sclera of the right eye. The reference electrode, seen on the right, is modeled after the 10mm gold cup electrode with 2mm hole and placed on the temple. (B) The Jet-ERG electrode, embedded in a polymer contact lens placed over the right eye. The reference electrode, seen on the right, is modeled as a 10mm disc and placed on the temple.

Material	D (mm)	Cond. s (S/m)
Vitreous Humor	16.3	1.5
RNFL [a]	0.032	0.5028
GC, IPL [a, b]	0.07	0.5028
A, H,B, M [a, b]	0.06	0.5028
OLM [b, c]	0.075	0.109
Rods, Cones [c]	0.05	0.5028
RPE [d]	0.01744	0.109
Choroid	0.28	0.2779
Sclera	0.45-1	0.5028
Posterior Tear Film	0.1	1.5
Adipose Tissue	-	0.02081
Air	-	0
Anterior Tear Film	0.1	1.5
Cornea	0.45	0.422
Anterior Chamber	1.79	1.5
Lens	4.98	0.3222
Muscle	-	0.26671
Bone	-	0.020059
Skin	-	0.00020
Gold	-	45200k
Silver	-	63000k
Si	-	0.00200

Table 5 Geometric and electrical properties of tissues, materials in the FE model of a human head.

Here D is the thickness of the structure as measured along the central axis of the eye [Oyster, 1999; Ban, 2011]. Particular emphasis was placed on including distinct retinal layers of appropriate thickness [a. Bagci et al., 2008; b. LoDuca et al., 2010; c. Shahidi et al., 2005; d. Wang et al., 2018]. Conductivity is given in Siemens per meter [Andreuccetti et al., 1997; Hasgall *et al.*, 2018].

5.1.3. Design considerations

Analogous with the previously described model of a rat head, various foramina of the human skull were considered for this model. The optic foramen, superior orbital fissure and

inferior orbital fissure were represented in this model, as these were considered significant features that would affect the electric field distribution from an exogenous current source as also described in previous sections. Apart from the detailed eye, muscle conductivity was chosen as representative of the soft tissue throughout the head, which was not further differentiated into vascular or nervous systems to reduce computational complexity.

As noted in Section 2, there is a wide range in ES parameters, including current amplitude, delivered throughout various studies of human EST, from 1μA to 10mA [Sehic et al., 2016]. A current source of 200mA was applied in the simulation, considered a representative example appropriate for the present study.

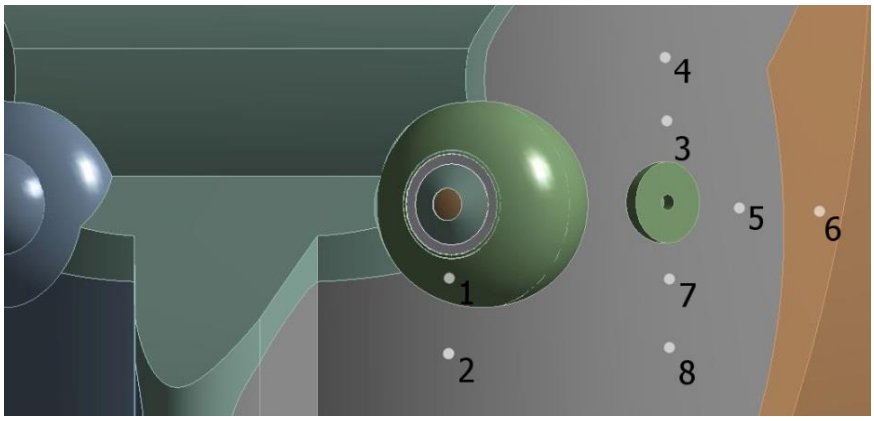

Figure 30. Voltage probe locations, human EST model.

Figure 30. Human head geometry as seen in ANSYS WB, white dots marking locations of voltage probes in simulation.

Execution of an EST treatment protocol in human subjects was beyond the scope of the present study, and as such no measurements from human subjects were obtained to as a means of validating the model of a human head subjected to EST as was done for the earlier rat model. However, locations of voltage probes in the DTL electrode simulation are marked with reference to location of the eye and associated electrodes such that future protocols may noninvasively measure potentials at analogous locations in human subjects for comparison. As seen in Figure

30, probe location 1 is on the sclera inferior to the corneal electrode and approximately another 1cm inferior to this is location 2 on skin. Locations 3, 5 and 7 are approximately 1cm from the center of the reference (cup) electrode in the superior, lateral (right) and inferior directions respectively. Locations 4,6 and 8 are 2cm from the center of the reference (cup) electrode in the superior, lateral (right) and inferior directions respectively.

Sensitivity of the model to changes in conductivity values of muscle, bone, skin and lens tissue was compared on the basis of RMSE. For each of these tissues, the model was run at 50%, 100% and 150% increments of the literature value for conductivity of that tissue while keeping all other tissues at literature value. Results of these simulations are plotted in Figure 31. The RMSE between potentials at each increment and the 100% value for each tissue was found.

Analogous to the process used for the comparison of electrode configurations in rats, the human EST electrode configurations were compared on current density at locations distributed along a line bisecting the retina at the photoreceptor layer, as seen in Figure 32. and Table 6.

5.2. Results

5.2.1. Sensitivity analysis

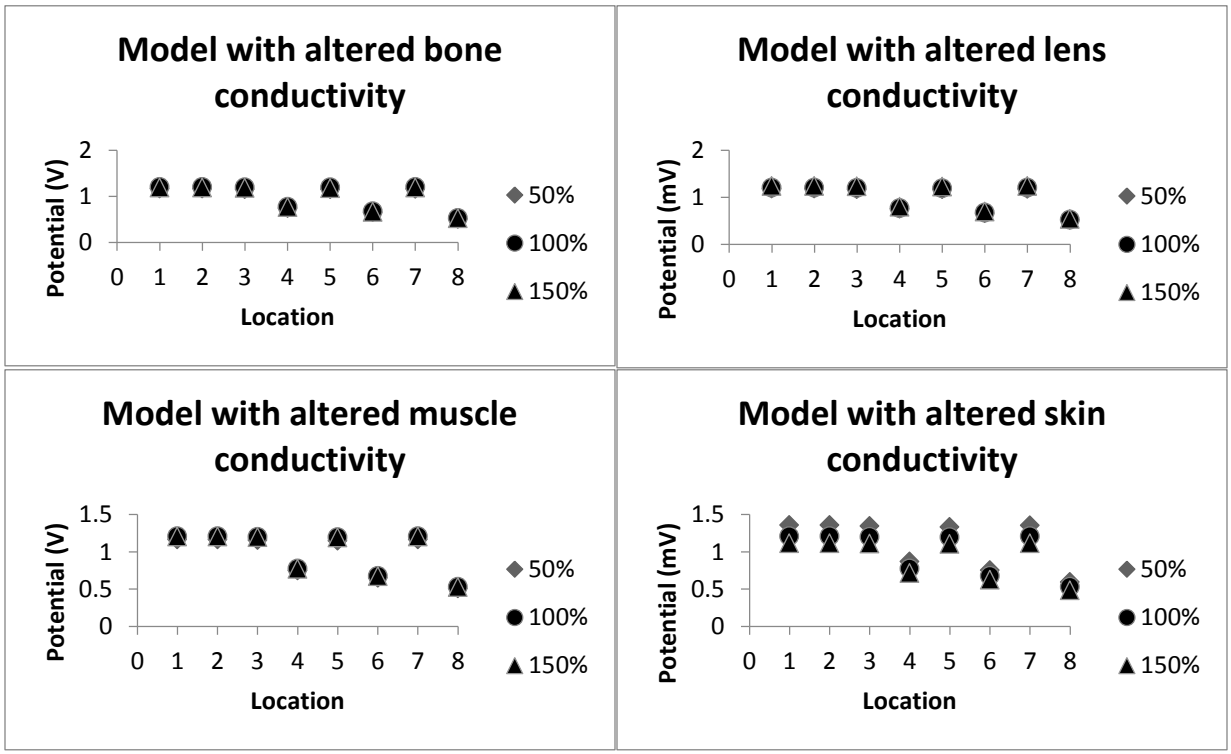

Figure 31. Effects of altering conductivity in tissues.

Figure 31. Effects of altering conductivity in tissues. Conductivity values were altered to increments of 50% and 150% in reference to literature values (at 100%) in bone, muscle, skin and lens tissues respectively, while holding all other tissues at literature values. Model results (V) are plotted vs. location, where locations correspond those shown in Figure 17B.

The RMSE was found to be .0253, .0207, .0249 and .1025V for bone, muscle, lens and skin respectively.

5.2.2. Spatial profiles of current density

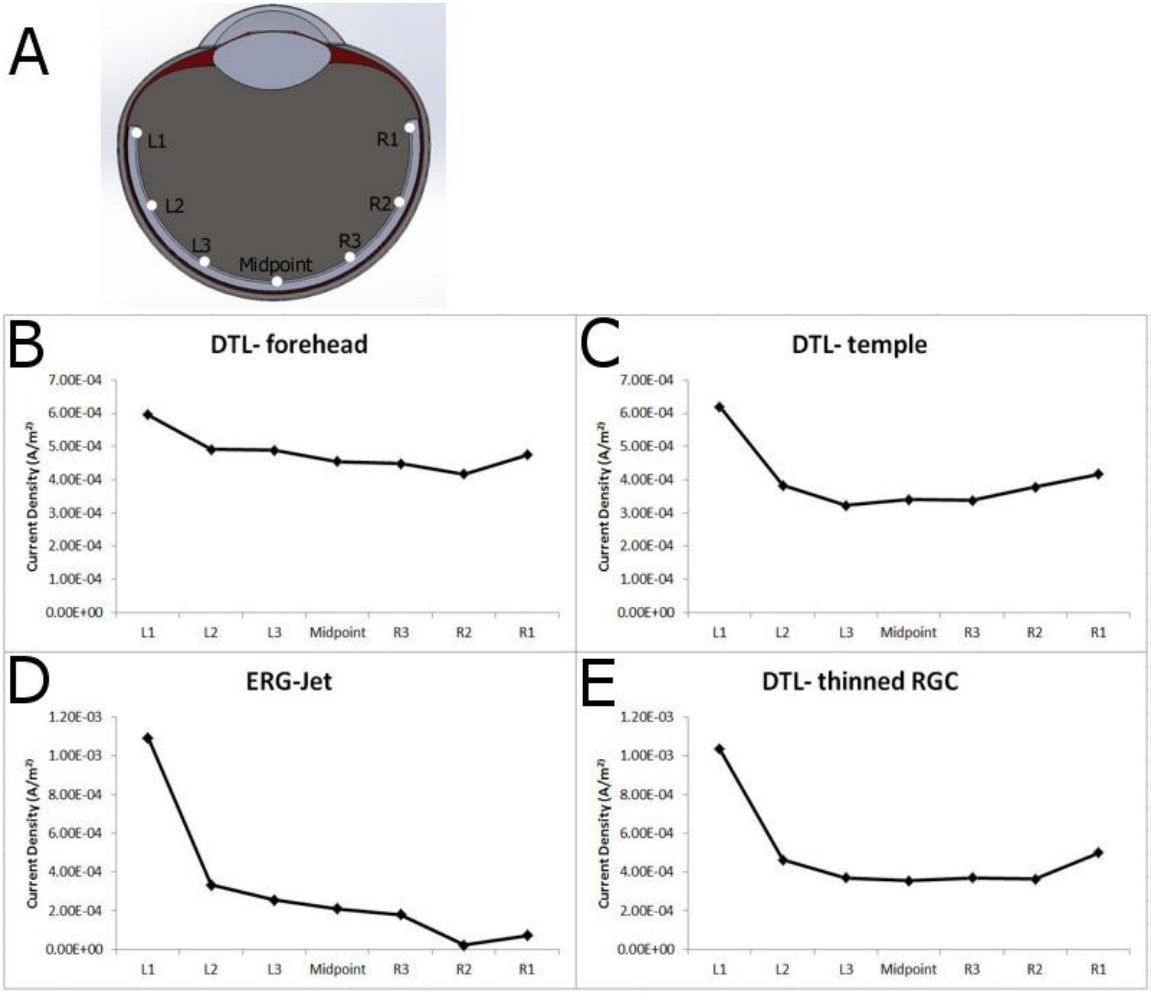

Figure 32. Distribution profiles of current density at the retina, human EST.

Figure 32. Distribution profiles of current density at the retina, human EST. (A) Current density evaluation points along the retina, for comparing the different electrode geometries. L1 and R1 correspond to points at the ora serrata, while L2, L3, R2 and R3 are equally spaced points between the ora serrata and the midpoint. All evaluation points are nodes within the photoreceptor later of the model. (B) Current density at observation points along the retina for the DTL electrode configuration with reference electrode places on the forehead. (C) Current density at observation points along the retina using the DTL electrode configuration with reference electrode on the temple. (D) Current density at observation points along the retina for the ERG-Jet electrode configuration with reference electrode on the temple. (E) Current density at observation points along the retina using the DTL electrode configuration and an approximation of thinned retinal ganglion cells as seen in glaucoma patients.

Location on the Retina	DTL-temple	DTL-thinned RGC	ERG-Jet	DTL-forehead
L1	6.20E-04	1.04E-03	1.09E-03	5.96E-04
L2	3.84E-04	4.63E-04	3.33E-04	4.92E-04
L3	3.23E-04	3.70E-04	2.56E-04	4.88E-04
Midpoint	3.40E-04	3.53E-04	2.10E-04	4.55E-04
R3	3.38E-04	3.70E-04	1.80E-04	4.49E-04
R2	3.78E-04	3.64E-04	2.25E-05	4.17E-04
R1	4.17E-04	5.00E-04	7.16E-05	4.75E-04
Mean	4.00E-04	4.94E-04	3.09E-04	4.82E-04
Std. Dev.	1.02E-04	2.45E-04	3.61E-04	5.65E-05
Coefficient of Variation	3.90E+00	2.01E+00	8.57E-01	8.52E+00

Table 6 Current density across the retina, EST in human model

Current density (in A/m^2) at seven locations across the retina (Figure 32A) for both electrode configurations as well as different placements of the reference electrode (as plotted in Figure 32B-E).

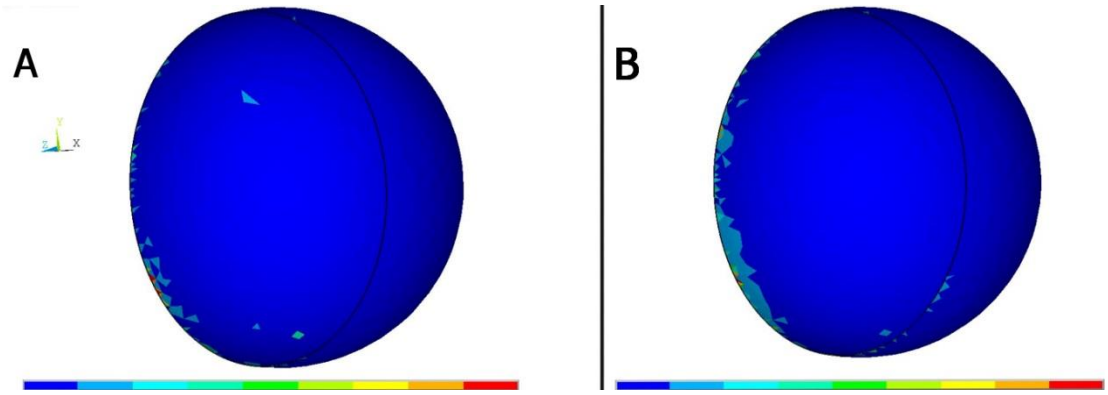

Figure 33. Current density at the retina in human EST.

Figure 33. The photoreceptor layer is shown here displaying the element solution for current density as color contour maps. (A) Results from model with DTL electrode, scale ranging from red at maximum ($1.696x10^{-3}$ A/m^2) to blue at minimum ($3.65x10^{-6}$ A/m^2). (B) Results from model with Jet-ERG electrode, scale ranging from red at maximum ($1.736x10^{-3}$ A/m^2) to blue at minimum ($2.32\ x10^{-6}$ A/m^2). For each geometry, the view has the photoreceptor layer rotated off-center to better show the peripheral edges. Each view represents over 5k solutions, with the left and right sides corresponding to the nasal and temporal directions respectively.

5.3. Discussion

5.2.1. Summary

A model of the human head exposed to an exogenous current from two different EST electrode configurations is presented. Sensitivity analysis of the model with the DTL electrode configuration applied showed the RMSE to be .0253, .0207, .0249 and .1025V for bone, muscle, lens and skin respectively, which occupy 26.9%, 57.46%, <1% and 6.2% respectively. By this metric, variation in skin showed the greatest effect on the model. This contrasts with the muscle conductivity giving highest RMSE in the rat model and may be due to greater skin thickness in the human model vs. that in the rat model.

Current density delivered by the two electrode configurations seem comparable in spatial distribution but on average the ERG-Jet electrode afforded lower current density, as evidenced by Figure 32 and the corresponding data in Table 6. As the same load of 200mA was applied

through the larger surface area of the ERG-Jet electrode, it follows that the current density distribution is significantly lower as seen here.

Viewing the contour plot of current density suggests higher current density delivered near the ora serrata/ peripheral nasal aspect of the retina as compared to the rest of the retina with both DTL and ERG-Jet electrode configurations, as suggested by Figure 33.

5.2.2. Limitations

The simplification of soft tissues throughout the head as having one conductivity, that of muscle, limits the utility of the model in some respects. This precludes using the model, for example, to investigate the effects of adipose deposits, nervous or circulatory systems and changes in conductivity therein. There is lack of validation data from human subjects in the present study.

5.2.3. Conclusions

Results from this model of the human head exposed to EST using DTL and ERG-Jet electrodes suggest these configurations delivery higher current density to the peripheral of the retina and a steep drop-off in density towards the center. This concurs with results from the analogous configuration in the rat model presented earlier, where the TES electrode also showed peaks in current density at the margins of the retina. This also concurs with a 2011 study by Xie et al., which plotted potential distribution results from an admittance model of DTL and ERG-Jet electrodes for retinal activation [Xi et al., 2011].

In both configurations applied to the human head model here, the reference electrodes were similarly placed on the ipsilateral temple. This is markedly different from the three

configurations presented earlier for the rat model, where the reference electrode size and placement were drastically different between WES, TES and SES. It follows then that the distribution profiles from the electrode configurations applied to the human model show less distinct differences in magnitude and spatial distribution.

As conductivity values are generally considered to be conserved across animal species, the model provided here may be considered a valid preliminary step towards more definitive models of the human head exposed to EST. Results thus obtained may directly inform the design of EST protocols for clinical practice. Considering the lack of validation data from human subjects, caution should presently be exercised in drawing generalizations from these results. Notably, there is considerable morphological variation between human subjects which can in turn lead to differences in electric field distribution from patient to patient. Ideally, future models would use geometry derived from bioimaging data from a morphological survey of human subjects, such that an idealized, "average human head" geometry could provide model results applicable to the most patients.

6. Specific Aim 4 – Analysis of ERG data following EST.

(Parts of this section were previously published as Rahmani, Safa, et al. “Chronic Delivery of Low-Level Exogenous Current Preserves Retinal Function in Pigmented P23H Rat.” Vision Research, 2013, doi:10.1016/j.visres.2012.10.016.)

6.1. Methods

Electroretinogram data was made available for analysis from two separate investigations into the effects of EST in P23H rats. Data from first study was collected by Dr.Safa Rahmani out of the Hetling lab at the University of Illinois at Chicago [Rahmani et al., 2013], while data from the second study was collected by Moon Han out of the Pardue lab at Center for Visual and Neurocognitive Rehabilitation, Atlanta VA Medical Center [Hanif et al., 2016]. Equipment for delivering EST and treatment parameters were provided by the Hetling lab at the University of Illinois at Chicago, consistent with previous work [Rahmani et al., 2013].

6.1.1. Methods, first data set, Hetling lab

In the first study, by Rahmani et al., low-level electric currents (sinusoidal, 1.5μ p-p at 5Hz) were delivered via electrodes placed on the cornea and in the mouth for 30-minute sessions twice a week thru 16 weeks of age. Single-flash electroretinograms were recorded at 4-week increments. Animals were dark adapted over two hours prior to ERG measurements. Under red light, the rats were anesthetized by an intraperitoneal (IP) injection of Ketamine and Xylazine (100 and 5 mg (kg body wt)"1, respectively). Flash stimuli (0.01, 2.6, 12, 54, 886, 2005 sc cd s m^2) were delivered in a semi-random order at intervals of 2 minutes, with each flash strength delivered three times. ERG responses were recorded using a stainless steel wire loop electrode placed in contact with the corneal surface. Two platinum subdermal needle electrodes (E2-4800,

Astro-Med Grass) were used as the reference electrodes, placed in the cheek and under the skin by the nape of the neck. All electrodes were connected to a differential AC amplifier (P511, Astro-Med Grass), with 1000x gain and 0.1–300 Hz pass band (-6 dB). Data was acquired with a sampling rate of 1 kHz [Rahmani et al., 2013].

Normalized ERG waveforms thus obtained were analyzed based on Lamb & Pugh's work characterizing ERG waveforms [Breton et al., 1994] using Equation 17 as follows,

$$f(t) = 1 - e^{I_{test}\,\gamma\left(\frac{(t-t_d)}{\alpha}\right)}$$

Equation 17

where f(t) is the normalized response, I_{test} is strength in sc cd s m^2, γ is a scaling factor, t is time, t_d is a delay of 3.1ms and α represents the amplification, left as the free parameter. Waveforms from a single experiment were averaged for repeated presentations of the same stimulus strength, and the fit of Equation 17 performed to the sets of four average waveforms (one waveform for each of the four highest flash strengths), resulting in a single value of a for each experiment. The set of waveforms for each experiment was normalized to the a-wave peak for the response to the highest flash strength; the time of peak was determined from the averaged response taken across all experiments under a given condition. The fit was performed for the segment of each waveform extending from t = 3 ms (the approximate post-stimulus time at which responses depart from baseline) to a time just preceding the a-wave peak for that response, which was evaluated for each individual waveform. The quality of the fit was evaluated using the correlation coefficient r^2, and the values of α were then averaged across experiments for comparison between treated and control groups at 4 and 16 weeks of age.

6.1.2. Methods, second data set, Pardue lab

In the second study, by Hanif et al., low-level electric currents (sinusoidal, 4μA at 5Hz) were passed between electrodes placed on the cornea and in the mouth for 30-minute sessions twice a week until 24 weeks of age. Animals were anesthetized by injection of ketamine (60 mg/kg)/xylazine (7.5 mg/kg) and dark-adapted overnight under dim red light. ERG responses of the retina were recorded every 4 weeks using a custom DTL electrode contacting the cornea prepped with a layer of 1% methylcellulose [Dawson et al., 1979]. Two platinum subdermal needle electrodes served as reference, placed in the cheek and tail respectively. ERG stimuli consisted of a series of increasing flash stimuli presented by a Ganzfeld dome [LKC BigShot, Gaithersburg, MD] with scotopic flash strengths (−3.4 to 3.0 log cd s/m^2) and photopic flash strengths (−0.8 to 2.0 log cd s/m^2)]. For photopic ERG recordings animals were light-adapted for 10 min prior to recording. During acquisition ERG responses were differentially amplified at 1–1500 Hz with a recording length of 250 ms digitized at a rate of 1.92 MHz [Hanif et al., 2016].

ERG a-wave and b-wave amplitudes were normalized to the amplitude of the response elicited with the strongest stimulus, which was above saturation, and used to generate amplitude–intensity plots. Survival of photoreceptor and bipolar cells may be inferred via analysis of a-wave and b-wave amplitudes. A difference in rod-photoreceptor response vs. cone-photoreceptor response may be inferred by differences between scotopic vs. photopic ERG responses in treated vs. control groups. The metric for amplification in the phototransduction cascade, α, was found using Equation 17 as it was for the data set collected by the Hetling lab. The stimulus strength required to elicit a half-saturated response, $I_{1/2}$, was taken as a measure of rod sensitivity. $I_{1/2}$ was determined at each 4-week increment by fitting the Naka-Rushton equation to the data, as described here,

$$A/Amax = I/(I+ I_{1/2})$$

Equation 18

where A is the response amplitude to the flash stimulus I (sc cd s m^{-2}), A_{max} is the maximum a-wave amplitude in response to a saturating flash strength.

6.2. Results

6.2.1 Analysis of first data set, Hetling lab

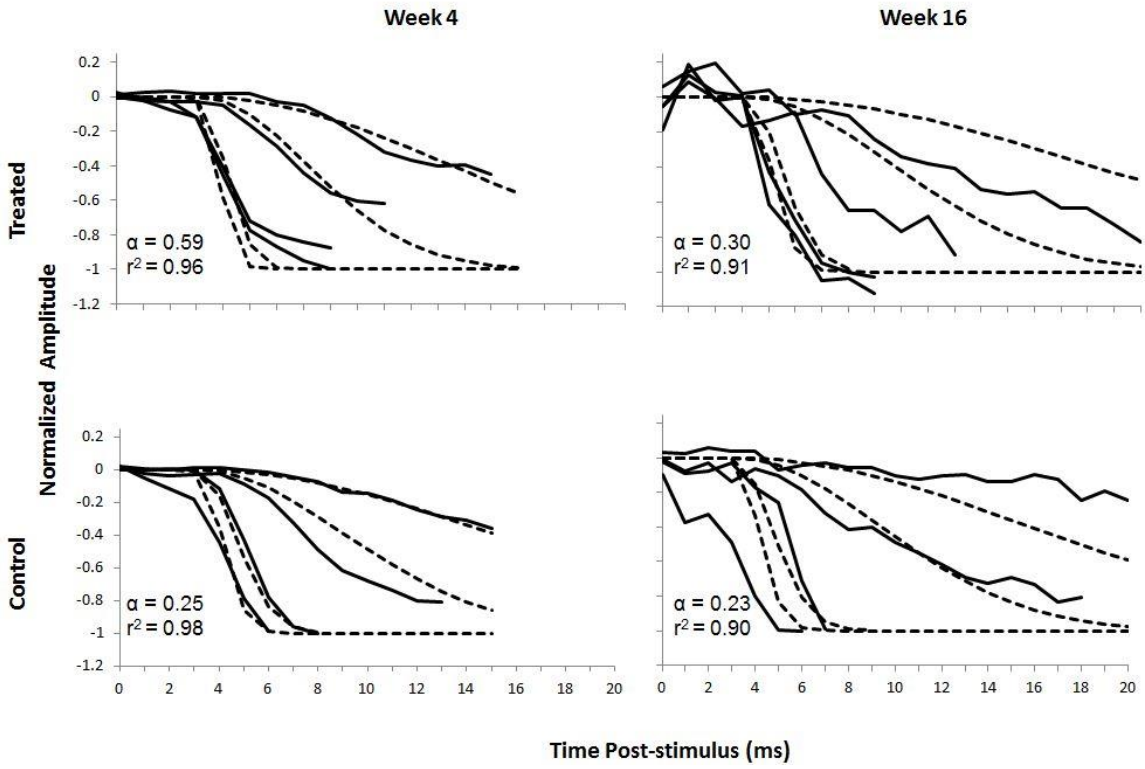

Figure 34. Representative ensemble fits to establish sensitivity constant α

Normalized ERG response waveforms (solid lines) and Equation 17 fitted to the ensemble of responses in each plot (dashed lines); values of free parameter α and measure of quality of fit (r^2) given in each panel. Stimulus strengths were 10, 52, 911 and 1850 sc cd s m^{-2} for the treated animal (top) and 14, 56, 860 and 2160 sc cd s m^{-2} for the control animal (bottom). Representative responses recorded at 4 weeks of age (left) and 16 weeks of age (right). Reprinted with permission [Rahmani et al., 2013].

As a measure of amplification in the phototransduction cascade, α was found using Equation 17 fit to the average response amplitude at each of 4 stimulus strengths, as in the

representative ensemble of fits from two individual animals plotted in Figure 34 (one treated, one control). The comparison of α in treated vs. control across all animals is summarized in Table 7.

	Control 4 week vs. 16 week	Treated 4 week vs. 16 week
α (mean ± 1 SD)	0.31 ± 0.14 vs. 0.27 ± 0.11	0.51 ± 0.22 vs. 0.32 ± 0.03
p-value (power)	.507 (10.3%)	.059 (61.6%)

Table 7 Trend in sensitivity constant α under EST

The parameter α, considered an index of the gain in phototransduction. Student's t-test used to calculate p-values; post hoc power analysis. Reprinted with permission [Rahmani et al., 2013].

6.2.2 Analysis of second data set, Pardue lab

ERG data from the Pardue lab were analyzed for a-wave and b-wave amplitude. Scotopic (dark-adapted) a-waves originate from rod photoreceptors [Hood and Birch, 1990] and were measured from baseline to trough of the first, negative component of the ERG waveform. A representative set of waveforms in response to different stimulus strengths is plotted in Figure 35. The results averaged across animals at 4 week increments of data collection, are shown in Table 8A and plotted in figure 36A. The b-wave component of the ERG waveform originates from depolarizing bipolar cells (Stockton and Slaughter, 1989), and was measured from the trough of the a-wave to the following peak of the waveform. Scotopic b-wave amplitudes averaged across animals at 4 week increments of data collection are shown in Table 8B and plotted in figure 36B.

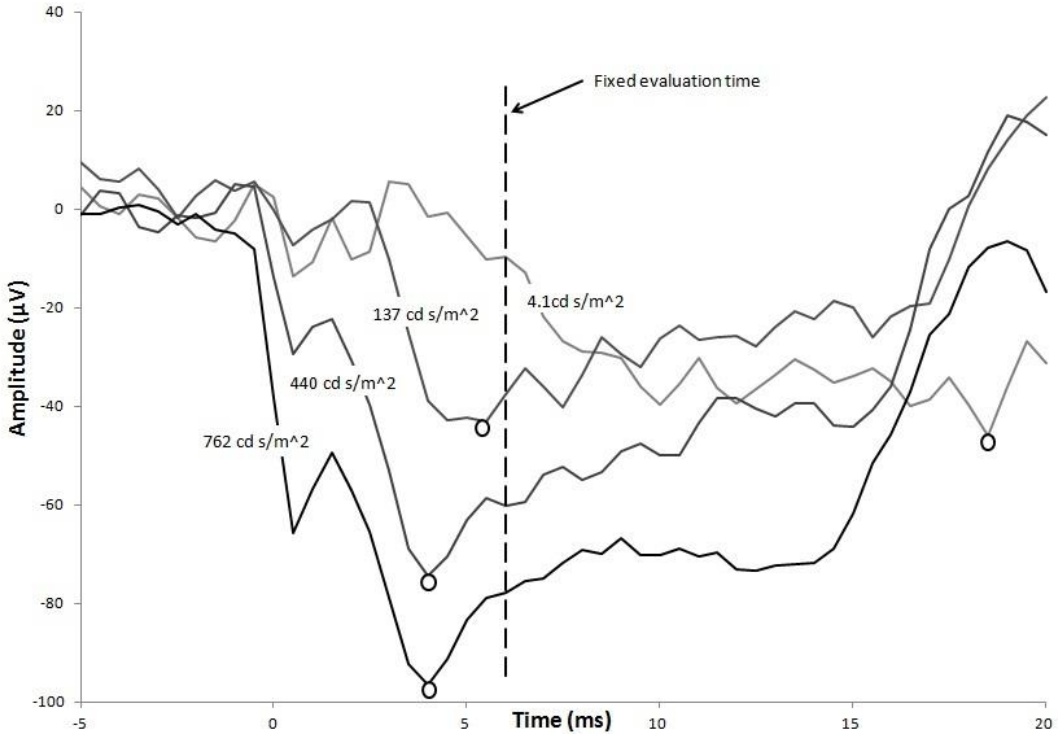

Figure 35. Evaluation of ERG a-wave amplitudes, representative waveforms.

Responses were evaluated for a-wave amplitude by two methods: 1) from baseline to the peak (most negative value within the window 3-32 ms after the stimulus), illustrated by the open circles in the traces, or 2) from baseline to the value of the waveform at a fixed time, here 6 ms after the flash (flash presented at t = 0), illustrated by the vertical dashed line. Note the significant negative-going artifact immediately following stimulus presentation. Stimulus strength noted for each waveform in figure.

A.

a-wave maximum amplitude						
Week	4	8	12	16	20-21	24
Control	-	42.07873	57.09542	32.71021	30.20253	41.58784
Std.Dev.	-	17.33644	30.34215	19.3079	18.61694	46.15148
n		8	8	9	10	13
Treated	64.44917	45.41299	53.27097	41.65077	38.98984	56.6607
Std.Dev.	37.82553	19.29102	27.96988	38.09725	28.28341	34.18395
n	6	13	6	7	10	9

B.

b-wave maximum amplitude						
Week	4	8	12	16	20-21	24
Control		193.1967	240.2177	272.7352	179.7235	211.4097
Std.Dev.	-	34.17953	106.2893	148.953	82.37989	109.5846
n	-	8	8	9	10	13
Treated	271.5609	185.4942	318.6912	258.5568	228.0564	243.0532
Std.Dev.	116.5279	79.09391	131.6068	130.3024	111.5229	65.59066
n	-	13	6	7	10	9

Table 8 Scotopic ERG amplitudes vs. age in treated and control animals.

A. Average scotopic a-wave amplitudes vs. age in treated and control animals stimulated with a 762 sc cd s m^{-2} flash. Evaluated for amplitude at 6 ms after the stimulus flash. B. Average scotopic b-wave amplitudes vs. age in treated and control animals stimulated with a 762 sc cd s m^{-2} flash. Evaluated for amplitude from a-wave trough to b-wave peak. Also plotted in Figure 36.

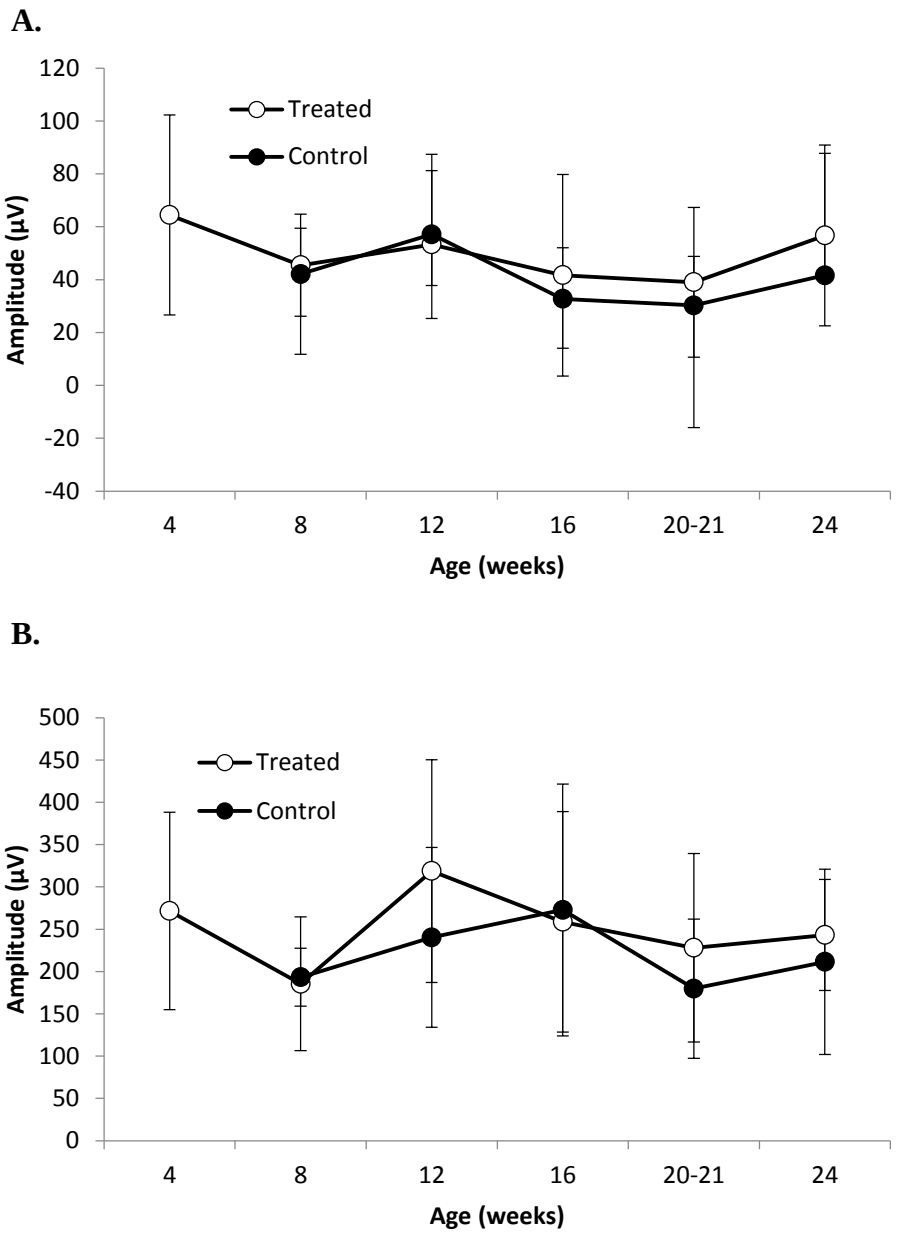

Figure 36. Scotopic ERG amplitudes vs. age in treated and control animals

A. Average scotopic a-wave amplitudes vs. age in treated and control animals stimulated with a 762 sc cd s m^{-2} flash. Evaluated for amplitude at 6 ms after the stimulus flash. B. Average scotopic b-wave amplitudes vs. age in treated and control animals stimulated with a 762 sc cd s m^{-2} flash. Evaluated for amplitude from a-wave trough to b-wave peak.

The b-wave of the photopic ERG response is attributed to ON-bipolar cells [Sieving et al., 1994]. Baseline scotopic and photopic ERG amplitudes were measured at 4 weeks from all animals, as plotted in Figure 37. and Figure 38 respectively.

A.

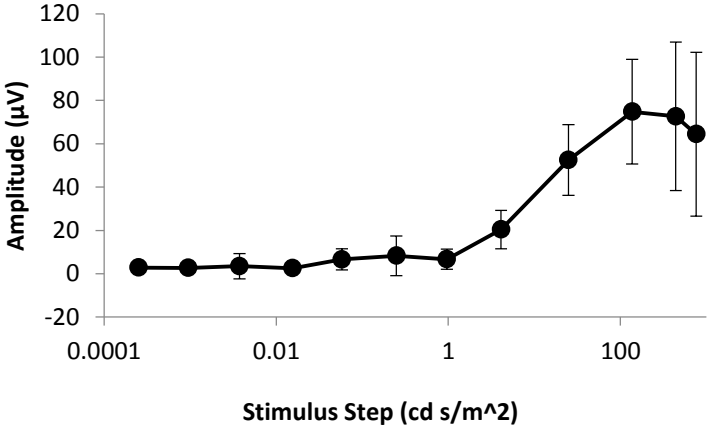

B.

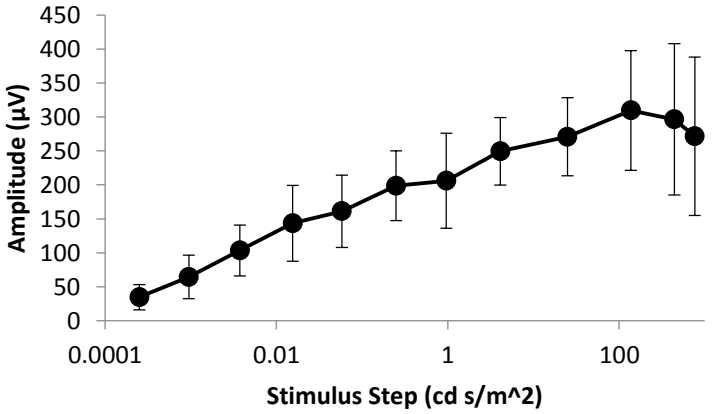

Figure 37 Scotopic ERG amplitudes per stimulus strength.

A. Average scotopic a-wave peaks at 4 weeks of age vs. stimulus strength, evaluated at a fixed time post-stimulus (t = 6 ms). Error bars plot ± 1 SD; n = 6. B. Average scotopic b-wave peaks at 4 weeks of age vs. stimulus strength. Amplitude evaluated from a-wave trough to b-wave peak. Error bars plot + 1 SD; n = 6.

A.

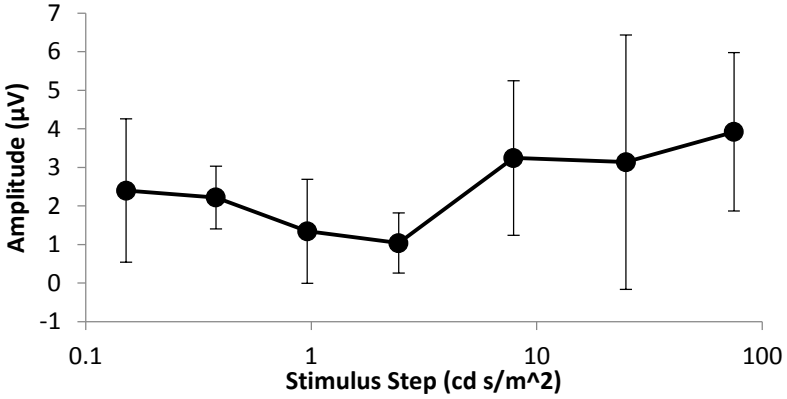

B.

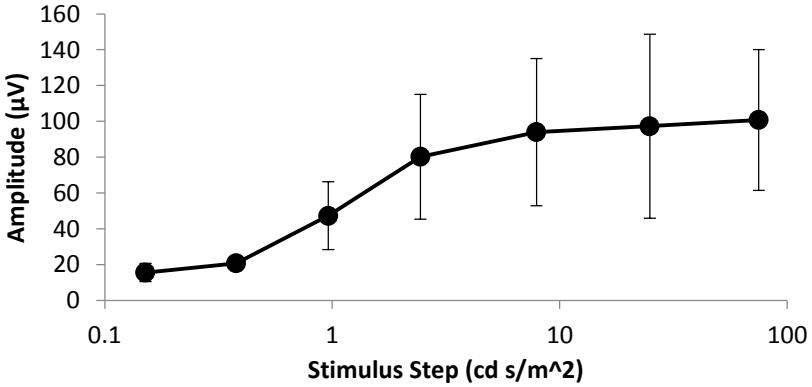

Figure 38. Photopic ERG amplitudes per stimulus strength.

A. Average photopic a-wave peaks at 4 weeks of age vs. stimulus strength, evaluated at a fixed time post-stimulus (t = 6 ms). Error bars plot ± 1 SD; n = 6. B. Average photopic b-wave peaks at 4 weeks of age vs. stimulus strength. Amplitude evaluated from a-wave trough to b-wave peak. Error bars plot + 1 SD; n = 6.

Continued ERG measurements at 4 week increments of time were taken in order to compare responses from treated and control groups. Considering what is known about the a-wave and b-wave components and their sources so far described, effects of EST of lack thereof may be inferred by looking for trends in photopic and scotopic a-wave and b-wave amplitudes over time. Scotopic a-wave and photopic a-wave amplitudes at 8 weeks are plotted in Figure 39. and Figure 40 respectively. Figure 41 plots photopic a-wave and b-wave amplitudes at 8 weeks. Scotopic and photopic a-wave peaks at week 16 are plotted in Figure 42A and Figure 42B respectively. Scotopic and photopic b-wave peaks at week 16 are plotted in Figure 43A and Figure 43B respectively. Similarly, scotopic a-wave and photopic a-wave amplitudes at 20 weeks are plotted in Figure 44. and Figure 45 respectively. Scotopic and photopic b-wave peaks at week 20 are plotted in Figure 46A and Figure 46B respectively.

A.

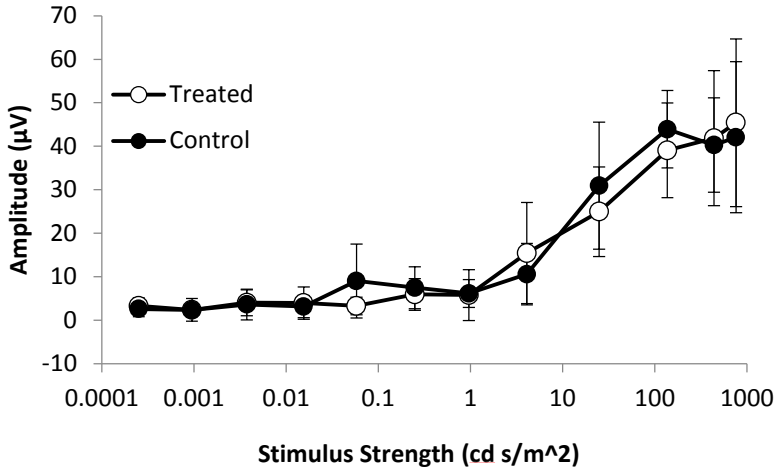

B.

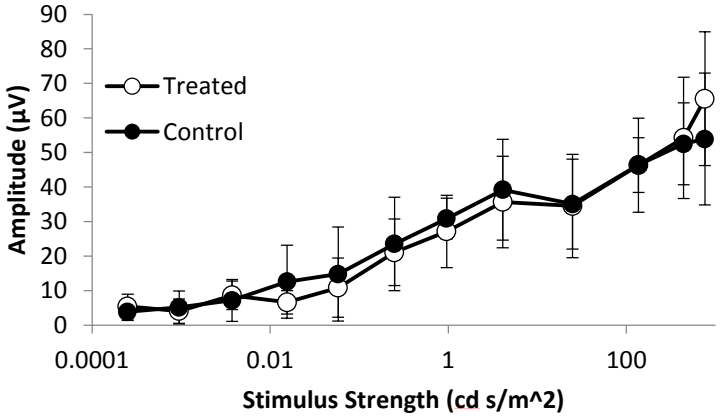

Figure 39. Scotopic a-wave amplitudes per stimulus strength at 8 weeks.

A. Average scotopic a-wave peaks at 8 weeks of age vs. stimulus strength, evaluated at a fixed time post-stimulus (t = 6 ms). Error bars plot ± 1 SD, n = 9 (control), n = 14 (treated). B. Average scotopic a-wave, at 8 weeks of age vs. stimulus strength. a-wave amplitude evaluated at peak (most negative value within the window 3-32 ms after the stimulus). Error bars plot ± 1 SD, n = 9 (control), n = 14 (treated).

A.

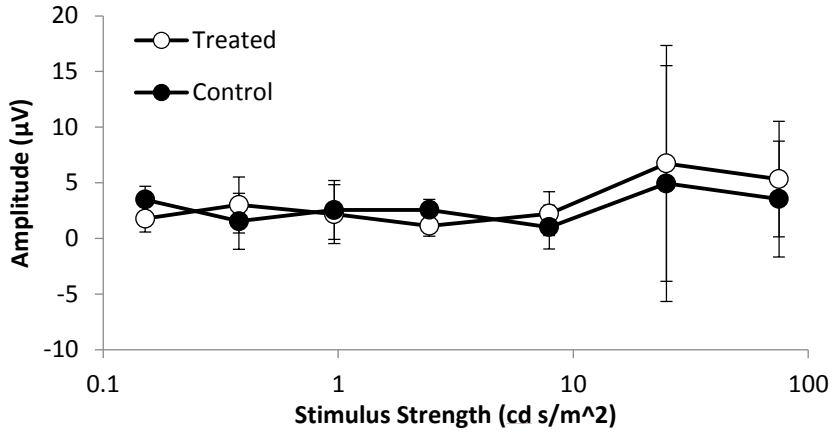

B.

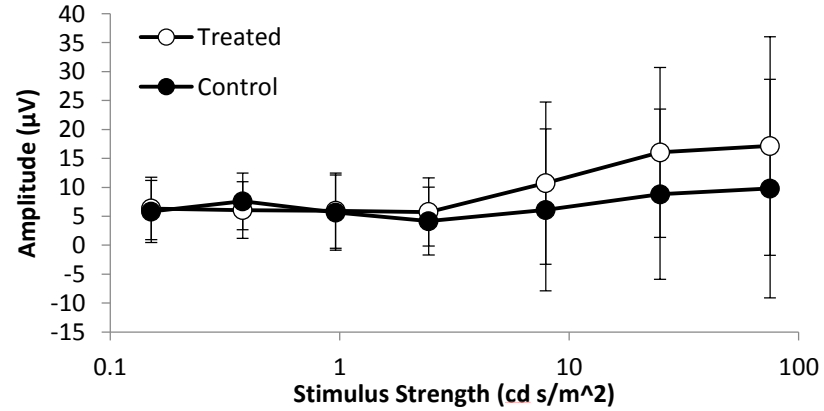

Figure 40. Phototopic a-wave amplitudes per stimulus strength at 8 weeks.
A. Average photopic a-wave peaks at 8 weeks of age vs. stimulus strength, evaluated at a fixed time post-stimulus (t = 6 ms). Error bars plot ± 1 SD, n = 9 (control), n = 14 (treated). B. Average photopic a-wave, at 8 weeks of age vs. stimulus strength. a-wave amplitude evaluated at peak (most negative value within the window 3-32 ms after the stimulus). Error bars plot ± 1 SD, n = 9 (control), n = 14 (treated).

A.

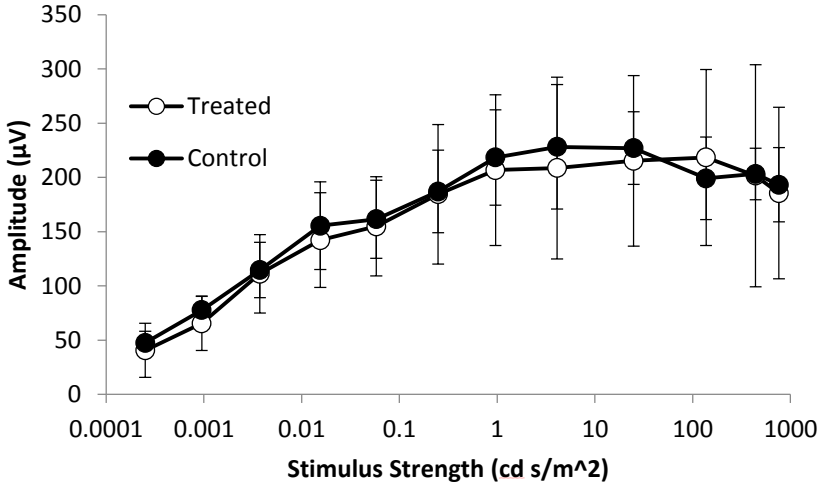

B.

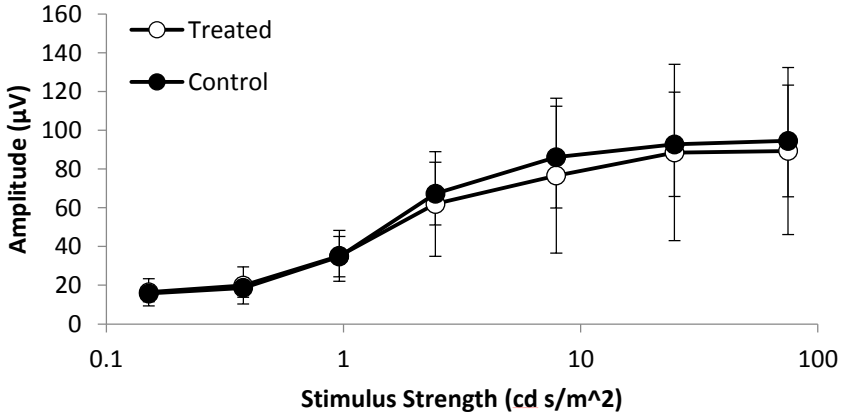

Figure 41. ERG b-wave amplitudes per stimulus strength at 8 weeks.

A. Average scotopic b-wave peaks at 8 weeks of age vs. stimulus strength. Amplitude evaluated from a-wave trough to b-wave peak. Error bars plot + 1 SD; n = 9 (control), n = 14 (treated). B. Average photopic b-wave peaks at 8 weeks of age vs. stimulus strength. Amplitude evaluated from a-wave trough to b-wave peak. Error bars plot + 1 SD; n = 9 (control), n = 14 (treated).

A.

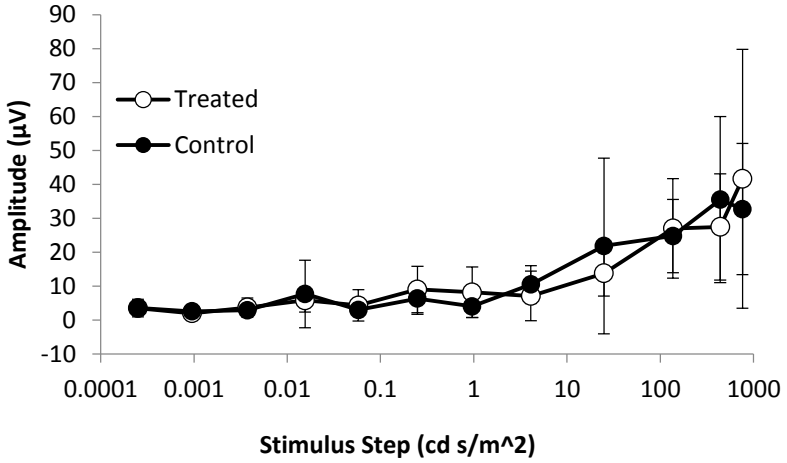

B.

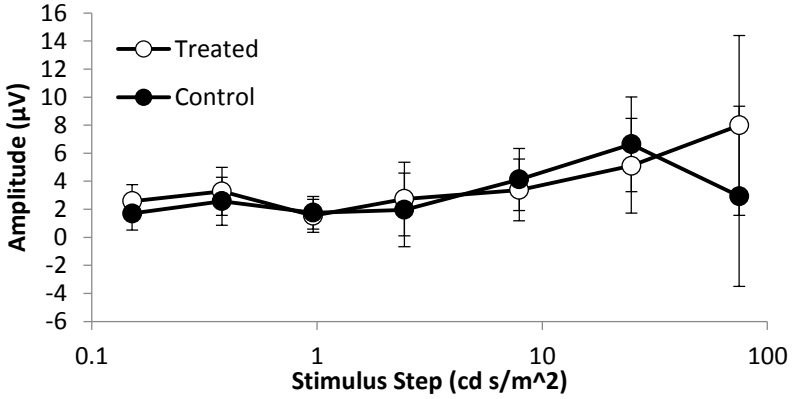

Figure 42. ERG a-wave amplitudes per stimulus strength at 16 weeks.

A. Average scotopic a-wave peaks at 16 weeks of age vs. stimulus strength, evaluated at a fixed time post-stimulus (t = 6 ms). Error bars plot ±1 SD; n = 8 (control), n = 6 (treated). B. Average photopic a-wave peaks at 16 weeks of age vs. stimulus strength, evaluated at a fixed time post-stimulus (t = 6 ms). Error bars plot ±1 SD; n = 8 (control), n = 6 (treated).

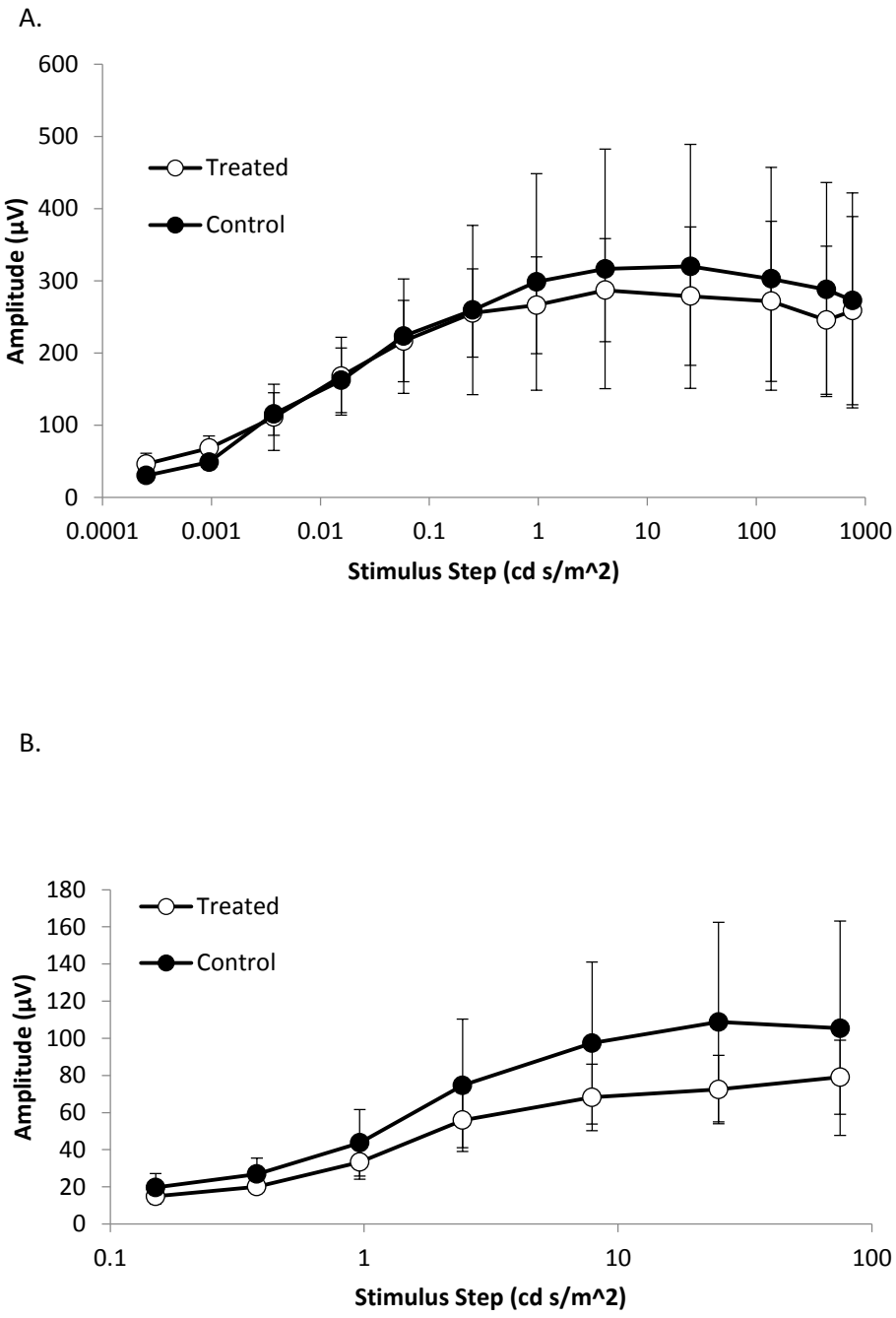

Figure 43. ERG b-wave amplitudes per stimulus strength at 16 weeks.
A. Average scotopic b-wave peaks at 16 weeks of age vs. stimulus strength. Amplitude evaluated from a-wave trough to b-wave peak. Error bars plot + 1 SD; n = 8 (control), n = 6 (treated). B. Average photopic b-wave peaks at 16 weeks of age vs. stimulus strength. Amplitude evaluated from a-wave trough to b-wave peak. Error bars plot + 1 SD; n = 8 (control), n = 6 (treated).

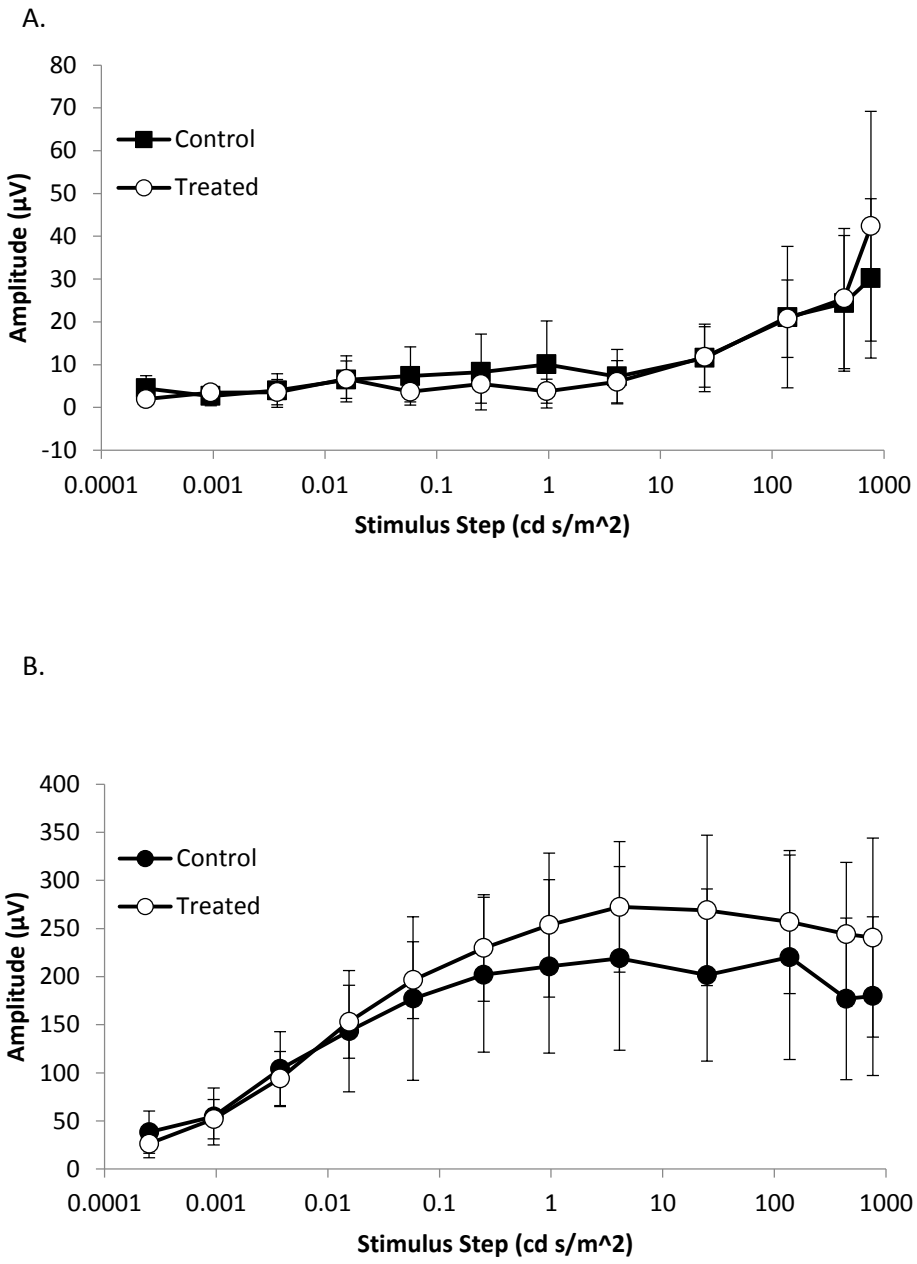

Figure 44. Average scotopic a-wave amplitudes at 20 weeks.

A. Average scotopic a-wave peaks at 20 weeks of age vs. stimulus strength, evaluated at a fixed time post-stimulus (t = 6 ms). Error bars plot ±1 SD; n = 3 (control), n = 8 (treated). B. Average scotopic a-wave, at 20 weeks of age vs. stimulus strength. a-wave amplitude evaluated at peak (most negative value within the window 3-32 ms after the stimulus). Error bars plot ±1 SD; n = 3 (control), n = 8 (treated).

A.

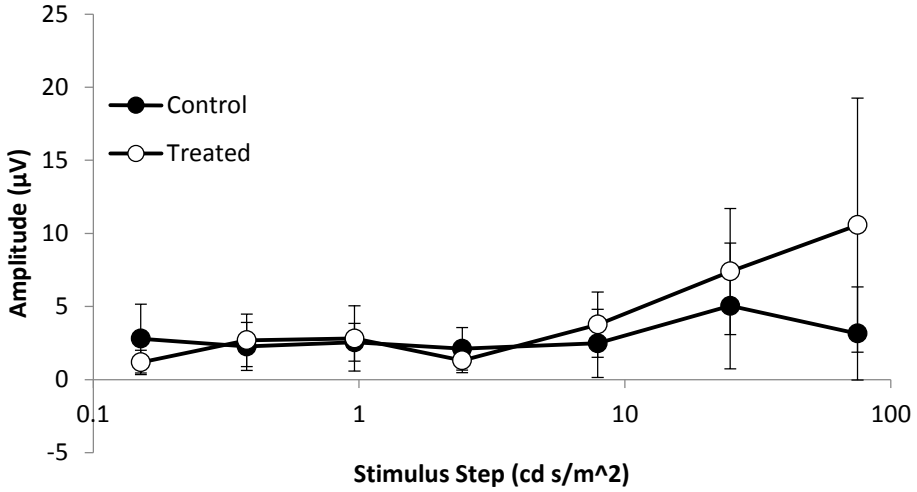

B.

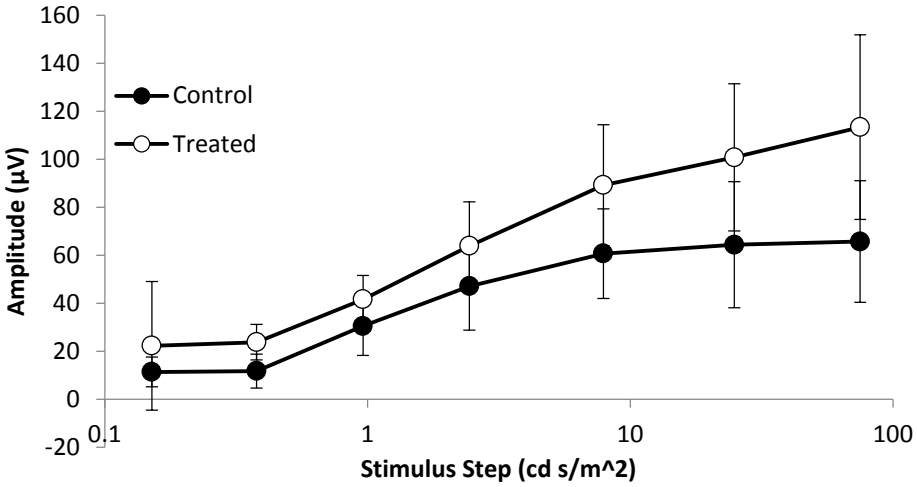

Figure 45. Average photopic a-wave amplitudes at 20 weeks.

A. Average photopic a-wave peaks at 20 weeks of age vs. stimulus strength, evaluated at a fixed time post-stimulus (t = 6 ms). Error bars plot ±1 SD; n = 3 (control), n = 8 (treated). B. Average photopic a-wave, at 20 weeks of age vs. stimulus strength. a-wave amplitude evaluated at peak (most negative value within the window 3-32 ms after the stimulus). Error bars plot ±1 SD; n = 3 (control), n = 8 (treated).

A.

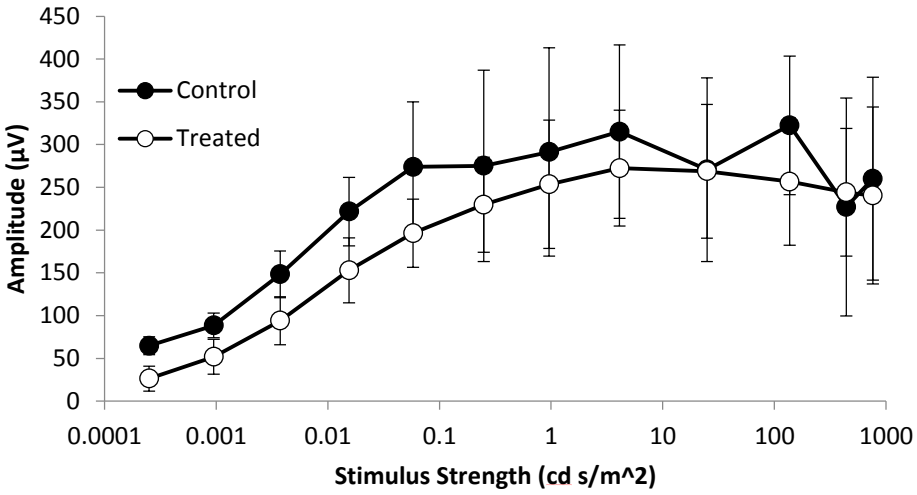

B.

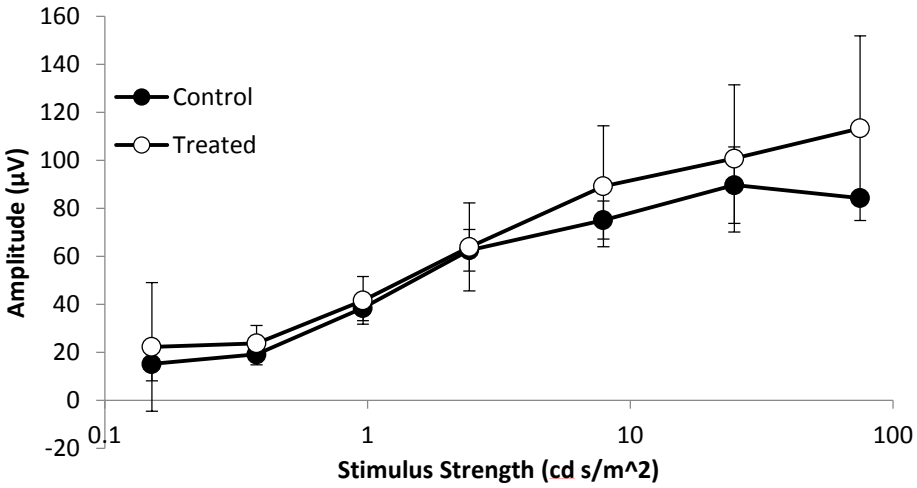

Figure 46. Average b-wave amplitudes at 20 weeks.

A. Average scotopic b-wave peaks at 20 weeks of age vs. stimulus strength. Amplitude evaluated from a-wave trough to b-wave peak. Error bars plot + 1 SD; n = 3 (control), n = 8 (treated). B. Average photopic b-wave peaks at 20 weeks of age vs. stimulus strength. Amplitude evaluated from a-wave trough to b-wave peak. Error bars plot + 1 SD; n = 3 (control), n = 8 (treated).

Having obtained ERG data at 4 week increments thru 20 weeks, the trends in a-wave amplitudes over time and any differences between treated and control groups per stimulus step could also be observed, as plotted in Figure 47. From the same 4 week increments of data collected, half-saturation ($I_{1/2}$) values are reported in Table 9 and plotted in Figure 48, and amplification factor α are reported in Table 10 And plotted in Figure. 49.

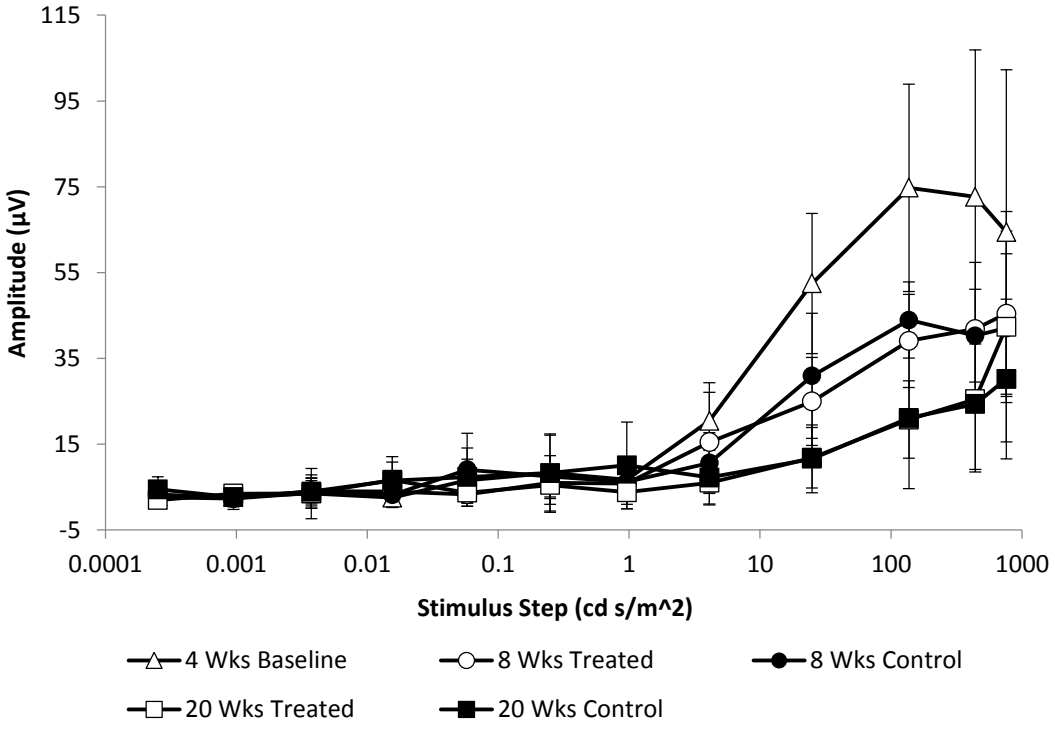

Figure 47. Scotopic a-wave amplitudes vs. stimulus strength over time.

Average scotopic a-wave peaks vs. stimulus strength, evaluated at a fixed time post-stimulus (t = 6 ms). Error bars plot ±1 SD.

	Half Saturation				
	Week	**4**	**8**	**16**	**20**
Control	**Mean**		**31.9375**	**24.3875**	**42.79143**
	Std.Dev.		**32.18966**	**19.49875**	**36.72308**
	n		**8**	**9**	**6**
Treated	**Mean**	**20**	**30.75**	**79.66667**	**75.4**
	Std.Dev.	**7.071068**	**25.4376**	**8.386497**	**14.72413**
	n	**2**	**4**	**4**	**5**

Table 9 Half-saturation vs. age.

Evaluated using scotopic a-wave peak amplitudes. Plotted in Figure 48.

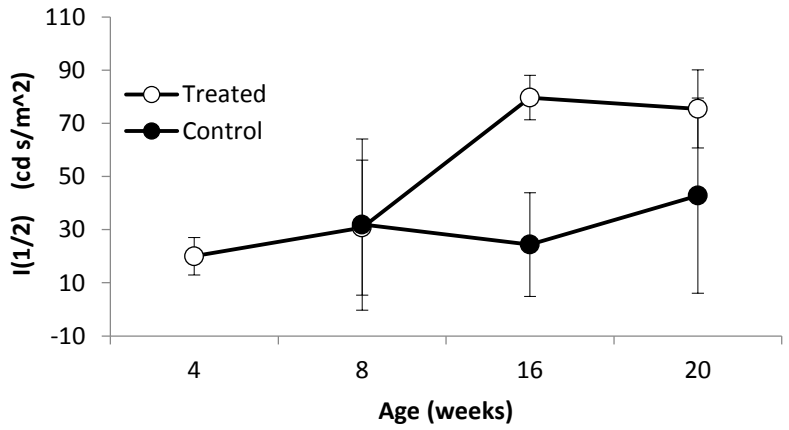

Figure 48. Half-saturation over time.

Half-saturation stimulus vs. age, evaluated using scotopic a-wave peak amplitudes. Error bars plot + 1 SD.

Week

	Animal #	4	16	20	24
Control	2026		0.25		
	2027		0.41		
	2028				
	2278		0.4		0.6
	2279				
	2280		0.41		
	2281		0.44		
	2335			0.6	
	2336				
	2337			0.65	
	2342				
	2343				
	2344				
	Avg.		0.382	0.625	0.6
	Std.Dev.	0	0.075299	0.035355	
	n	0	5	2	1

		Week			
	Animal #	4	16	20	24
Treated	2226		0.34	1	
	2227		0.32		
	2235	0.28	0.43		0.75
	2236	0.27	0.4		
	2238	0.34			
	2239	0.24			
	2333				
	2334				
	2339			0.83	
	2340				
	Avg.	0.2825	0.3725	0.915	0.75
	Std.Dev.	0.041932	0.051235	0.120208	
	n	6	4	2	1

Table 10 Sensitivity constant α over time.

As per the Equation 17, evaluated using scotopic a-wave responses. Plotted in Figure 49.

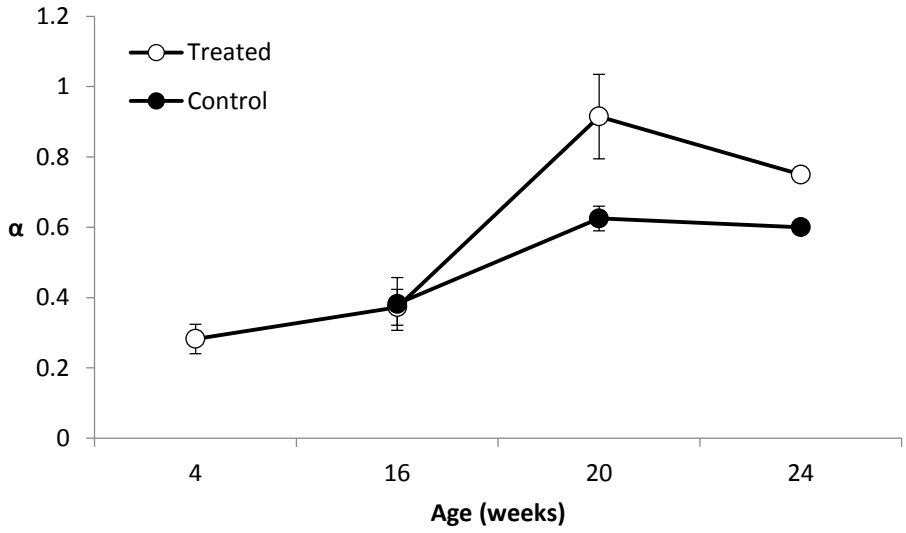

Figure 49. Sensitivity constant α over time.

As per Equation 17, evaluated using scotopic a-wave responses. Error bars plot + 1 SD.

6.3 Discussion

6.3.1. Summary

In analysis of the first data set, representative ensemble fits to Equation 17 to ascertain the sensitivity constant α are shown in Figure 34. Fits to the responses were generally good, with the mean (±1 SD) r^2 value of 0.97 + 0.02 (range 0.92–0.99) for responses recorded at 4 weeks of age, and 0.91 + 0.03 (range 0.84–0.97) at 16 weeks of age. The normalized responses used for the fits appear quite noisy by 16 weeks of age (right-side panels in Figure 34). The mean values of the sensitivity constant α for each group at 4 and 16 weeks of age are summarized in Table 7. The control group showed no significant change in α over the ages investigated, while the treated group exhibited a slight decrease.

In analysis of the second data set, where survival of photoreceptor and bipolar cells might be inferred via a- and b-wave analysis respectively, there was no appreciable difference in amplitude between treated and control group at each time increment (statistical power of 6.9%.

9.2% and 30.9% at weeks 4, 12 and 20 respectively for Student's t-test), as reported in Table 8 and plotted in Figure 36, suggesting that the survival rate among the populations of photoreceptor and bipolar cells remains unaffected by EST treatments, and the mechanism for any effects of the treatment lay elsewhere.

Regarding sensitivity of the retinal tissues to light, it was observed that whereas $I_{1/2}$ shows an increase in both treated and control groups over time, the treated group exhibits a greater rate of increase than the control group (statistical power of 5.1%, 100% and 51.3% for Student's t-test at weeks 8, 16 and 20 respectively), as plotted in Figure 48.

Regarding gain in the phototransduction, it was observed that whereas α increased in both treated and control groups over time, the treated group exhibits a greater increase than the control group (statistical power of 90.7% for Student's t-test), as reported in Table 10 and plotted in Figure 49.

6.3.2. Limitations

In analyzing the first data set, the noisy quality of the data may be considered the consequence of too low of a sampling rate (1 kHz) as well as small amplitude of the responses by 16 weeks (~50μV at most) due to the extent of progression of the retinal degeneration by this age in the P23H rats. The same loss of amplitude may be the reason for no discernable difference in response amplitude between treated and control groups of the second data set. Notably the waveforms show a pronounced negative response at time 0, which arises from the photovoltaic effect of the stimulus flash acting on the silver wire of the custom DTL electrode used to measure the ERG responses. This type of artifact is known in the literature [Perlman et al., 2015], and while this may have impacted assessment of the a-wave amplitudes, the values for the amplification factor α found via Equation 17 should remain unaffected.

6.3.3. Conclusions

While ERG analysis suggests no effect from EST on survival of photoreceptor and bipolar cell populations, there appears to be functional effects pertaining to sensitivty and gain in the phototransduction cascade. The greater increase in α in the treated group from the first data set suggests EST enhancement of a compensatory mechanism in retinal cells as degeneration progresses. This concurs with other findings reported on the same group of animals [Rahmani et al., 2013], where preservation of b-wave amplitudes but continued decay of a-wave amplitudes in treated EST-treated animals suggested a preservation of photoreceptor-bipolar cell coupling. The $I_{1/2}$ value, which is the stimulus strength needed to elicit a half-saturating a-wave, increased in control animals but was constant in treated animals. This result, combined with the decrease in α reported by the present study, suggests the preservation of sensitivity was mediated by an increase of efficiency in photoisomerization.

The preserved rod sensitivity (vis-à-vis conserved $I_{1/2}$ value) in treated animals reported by Dr.Rahmani on her analysis of first data set was not mirrored in analysis of the second data set in the present work. This may be in part due to the higher current level of 4μA used for treatment in the animals of the second data set vs. the 1.5 μA used on the animals of the first data set. Notably, histological analysis [Rahmani et al., 2013; Hanif et al., 2016] of animals from which both data sets were collected showed no structural preservation of the outer retina, further emphasizing the significance of the functional effects from EST on the retina.

As reported by Hanif et al. from the Pardue lab, animals of the second data set were further studied on visual function via optokinetic tracking (OKT), on gene expression analysis of retinal tissue and on retinal structure [Hanif et al., 2016]. Assessment via OKT showed significant preservation of visual acuity in WES treated rats. Analysis of relative expression of

Bdnf, Fgf2, Casp3 and *Gs* 1 hour after WES sessions showed significantly greater expression in the WES treated rats, while no difference in expression was seen in *Igf1, Cntf1* or *Bax*. At 24 hours post-treatment, expression levels were not different in any of the genes tested. This suggests further studies are needed to establish dose-dependancy of the gene expression induced by WES and to establish whether greater frequency in treatments would produce more sustained increase in such gene expression.

Measurements of thickness of the outer segment and inner photoreceptor segment, ONL, inner nuclear layer and inner plexiform layers confirmed no difference between treated and control groups. This concurs with the results of the present thesis, where there was no appreciable difference in a-wave amplitudes, from which it was inferred that there was no effect on the sruvival of photoreceptor cells. It was however noted that summed nuclei in the RGC layer from both inferior and superior regions were found to be significantly greater in WES treated animals. This suggests further studies are needed to measure RGC function and ascertain the source of neuropreservation from WES.

7. Global Summary

7.1. Review of main results, conclusions and potential clinical impact

7.1.1. Specific Aim 1

Build and validate an electrostatic model of a rat head undergoing EST.

Early simulations were run using the simplified "muppet" model shown in Figure 17A. Measurements of electric potential for validation purposes were made on twelve P23H transgenic rats (line 1), aged 6 to 11 weeks undergoing EST. This early work provided a profile of electric potentials, albeit with wide standard of deviation seen in the measured potentials. Orthogonal section views representing the sagittal, coronal and axial anatomical planes were extrapolated and sculpted to arrive at a three-dimensional representation of the rat skull for the more detailed "Remy" model of a rat head. Both models included one eye with high detail, including distinct retinal layers. Regarding model sensitivity, incremental changes to muscle conductivity yielded the largest RMSE in the model results, and muscle tissue is known to undergo significant conductivity changes with time post-mortem [Zheng et al., 1984; Martinsen et al., 2000; Roth et al., 2006]. These temporal changes may account, in part, for variability in the impedance values reported across literature, and may have affected the *in situ* measurements of electrical potential used for validation of this model (see below). Muscle conductivity was thus the sole free parameter in the optimization process. Iterative simulations showed minimum error with conductivity value at (1/12) of literature value. Post-mortem changes in muscle conductivity and onset of rigor accelerated by the application of an electric current [Roth et al., 2006] may account for this suggested over-ten-fold decrease in muscle conductivity. Residual error between model and measurements was below inter-animal variance in the measurements. The resulting model can serve as a baseline for objective comparison of other electrode shapes and configurations.

7.1.2. Specific Aim 2

Predict current density at the retina using the electrostatic model of a rat head for different EST electrode configurations.

Three distinct electrode geometries used to investigate EST in rats have been represented in the model, as illustrated in Figure 20. Whole-eye stimulation (WES),transcorneal electrical stimulation (TES) and subretinal electrical stimulation (SES) configurations were applied both to the early, idealized "muppet" model of a rat head and to the later, more detailed "Remy" model. The diseased state of the retina as in RP was also implemented in the model, approximated by applying the conductivity value of the adjacent cell layer (GC, AC, H/BC, MC) to the OLM layer.

Early simulations using the "muppet" model showed distinct profiles of current density distribution along the retina afforded by the different electrode configurations, as plotted in Figure 21. Using the more detailed, "Remy" model of the rat head, current density values were evaluated at locations across the inner (vitreal) surface of the photoreceptor layer, as illustrated in Figure 22A. The resulting values, along with summary statistics, are given in Table 4. Notably, the mean current density provided by the SES electrode configuration is orders of magnitude lower than that obtained with WES and TES. To help visualize the spatial distribution of retinal current density, the values of Table 4 were normalized, and plotted together vs. retinal location in Figure 22B. Figure 22C-E plot the current densities for healthy and degenerate retina for WES, TES and SES, respectively. Color contour plots of current density for each EST electrode configuration are shown in Figure 23 at all locations across the photoreceptor layer, providing maps with fuller view of the spatial distribution of current density. Of note is the marked asymmetric non-uniformity in retinal current density resulting from WES and SES, both of which peak off-center and appear to be influenced by the foramen in

the skull (local areas of high conductivity). TES results in a more symmetric non-uniformity, with peaks near the margins of the retina; this is consistent with the corneal positions of the active and return electrodes.

The significant change in OLM conductivity in the approximation of a diseased state had no observable effect on WES or TES. For SES, the current density at each evaluation point increased in the absence of the low-conductivity OLM. This appears to reflect an increase in current passing through the inner retina.

Potential measurements made at precise locations closer to, and within, the eye via a stereotaxic frame would be required for further model refinement. Making measurements at all locations simultaneously would also be desirable. Muscle conductivity as determined from the methods described in Section 3 is a key factor in determining absolute values in potential one can expect to measure from the different electrode configurations, and as such validation measurements from live animals are all the more desirable.

The quantitative, objective evaluation of current density across EST electrode configurations reported here is unique, and will assist in generalizing results across studies, and in the design of optimal electrode configurations. This basic approach may now be applied to other mammal models, including human as described in the following section. Results thus obtained may directly inform the design of EST protocols for clinical practice.

7.1.3. Specific Aim 3

Develop a model of the human head and predict current density at the retina afforded by EST.

Similar to the approach described in Section 3 on building the geometry for the rat head, views of the sagittal, coronal and axial anatomical planes were extrapolated and sculpted to arrive at a three-dimensional representation of the a skull in SolidWorks. As with the previously described rat head model, one eye in the model was taken to be the target of simulated EST and was defined with a high level of detail. Two electrode configurations were applied to this base model, the DTL electrode and the ERG-Jet electrode, as seen in Figure 29.

Sensitivity of the model to changes in conductivity values of muscle, bone, skin and lens tissue was compared on the basis of RMSE, which suggested changes to skin conductivity had the greatest affect on the model. Analogous to the process used for the comparison of electrode configurations in rats, the human EST electrode configurations were compared on current density at locations distributed along a line bisecting the retina at the photoreceptor layer. Results from this model of the human head exposed to EST using DTL and ERG-Jet electrodes suggest these configurations delivery higher current density to the peripheral of the retina and a steep drop-off in density towards the center. This concurs with results from the analogous configuration in the rat model presented earlier, where the TES electrode also showed peaks in current density at the margins of the retina. This also concurs with a 2011 study by Xie et al. which plotted potential distribution results from an admittance model of DTL and ERG-Jet electrodes for retinal activation [Xie et al., 2011].

There is lack of validation data from human subjects in the present study. As conductivity values are generally considered to be conserved across animal species, the model provided here, may be considered a valid preliminary step towards more definitive models of the

human head exposed to EST. Results thus obtained may directly inform the design of EST protocols for clinical practice. Considering the lack of validation data from human subjects, caution should presently be exercised in drawing generalizations from these results. Notably, there is considerable morphological variation between human subjects which can in turn lead to differences in electric field distribution from patient to patient. Ideally, future models would use geometry derived from bioimaging data from a morphological survey of human subjects, such that an idealized, "average human head" geometry could provide model results applicable to the most patients.

7.1.4. Specific Aim 4
Analysis of ERG data following EST.

Electroretinogram data was made available for analysis from two separate investigations into the effects of EST in P23H rats. Data from first study was collected by Dr. Safa Rahmani out of the Hetling lab at the University of Illinois at Chicago [Rahmani et al., 2013], while data from the second study was collected by Moon Han out of the Pardue lab at Center for Visual and Neurocognitive Rehabilitation, Atlanta VA Medical Center [Hanif et al., 2016].

In analysis of the first data set, representative ensemble fits to Equation 17 to ascertain the sensitivity constant α are shown in Figure 34. The control group showed no significant change in α over the ages investigated, while the treated group exhibited a decrease that was on the margin of significance. This concurs with other findings reported on the same group of animals [Rahmani et al., 2013], where preservation of b-wave amplitudes but continued decay of a-wave amplitudes in treated EST-treated animals suggested a preservation of photoreceptor-bipolar cell coupling.

In analyzing the first data set (from the Hetling lab), the noisy quality of the data may be considered the consequence of too low of a sampling rate as well as small amplitude of the responses by 16 weeks due to the extent of progression of the retinal degeneration by this age in the P23H rats. The same loss of amplitude may be the reason for no discernable difference in response amplitude between treated and control groups of the second data set.

In analysis of the second data set (from the Pardue lab), where survival of photoreceptor an bipolar cells might be inferred via a- and b-wave analysis, there was no appreciable difference in amplitude between treated and control group at each time increment, as plotted in Figure 36, suggesting that the survival rate among the populations of photoreceptor and bipolar cells remains unaffected by EST treatments, and the mechanism for any effects of the treatment lay elsewhere. Regarding sensitivity of the retinal tissues to light, it was observed that whereas $I_{1/2}$ shows an increase in both treated and control groups over time, the treated group exhibits a greater rate of increase than the control group, as plotted in Figure 48. Regarding gain in the phototransduction, it was observed that whereas α increased in both treated and control groups over time, the treated group exhibits a greater increase than the control group, as plotted in Figure 49.

While ERG analysis suggests no effect from EST on survival of photoreceptor and bipolar cell populations (per a-wave and b-wave amplitudes), there appears to be functional effects pertaining to sensitivty and gain in the phototransduction cascade. The greater increase in α in the treated group from the first data set suggests EST enhancement of a compensatory mechanism in retinal cells as degeneration progresses. The $I_{1/2}$ value increased in control animals but was constant in treated animals. The combination of these two metrics suggests the preservation of sensitivity was mediated by an increase of efficiency in photoisomerization.

Results on further assessment of the animals of the second data set [Hanif et al., 2016] suggest further studies are needed to establish dose-dependancy of the gene expression induced by WES and to establish whether greater frequency in treatments would produce more sustained increase in such gene expression. The results also suggest further studies are needed to measure RGC function and ascertain the source of neuropreservation from WES. Measurements of thickness of the outer segment and inner photoreceptor segment, ONL, inner nuclear layer and inner plexiform layers confirmed no difference between treated and control groups. This concurs with the results of the present thesis, where there was no appreciable difference in a-wave amplitudes, from which it was inferred that there was no effect on the sruvival of photoreceptor cells.

7.2. Future directions

The FE models described herein, while sufficient to answer the questions posed in the specific aims of the present work, may be improved upon in future iterations. Model geometry was constructed by projecting spline traces of anatomical drawings of the skull to build a base skull to which soft tissues and detailed eye models were added, in both rat and human models. This approach provided a financially and computationally low-cost method of geometry construction, but is only one of several options available for building geometry. DICOM files of MRI scans of human anatomy may provide a high degree of detail for model geometry of the head after either manual or algorithm-driven segmentation from layer to layer of the scan. A similar approach could be taken for rat anatomy, through rodent MRI scans from appropriately specialized facilities. Even with geometry of the head built from such highly detailed scans, the microscale resolution at the eye required to discern discreet retinal layers is not yet part of standard clinical MRI protocols, and as such the eye geometry would need to be separately

imported to achieve relevant results. Computational cost will inherently become a lesser concern over time. Whereas early modeling work was taxing on available computer hardware, which included a 2.5 GHz processor and redundant hard disk drives arranged in RAID configuration, later models were run on a machine with a 3.5 Ghz six-core processor off of a solid-state drive, eliminating bottlenecks in simulation processing and enabling multiple, rapid iterations of the simulations. Processing power on commonly available computer hardware has significantly advanced even within the timeframe of data collection in the present work. Improved computational capabilities could enable, for example, the inclusion of a tapered profile to the margin of the retina making a clearly discernable and anatomically relatable ora serrata.

In collecting measurements for model validation, a stereotaxic frame for more precise measurements and a custom jig for consistent electrode placements would be ideal to minimize sources of variability in potentials measured from subjects undergoing EST. Multi-channel data acquisition making measurements at all locations simultaneously would also be desirable, as significant time is spent moving the recording electrode from position to position during which the post-mortem tissue electrical properties can change in the case of recently sacrificed animal specimens. Use of a custom jig and simultaneous recordings should also reduce wear and tear on the platinum needle electrodes, which required sharpening between recording sessions and replacement after breakage from repeated insertions. Measurements for validation from live subjects undergoing EST are desirable for more direct comparison with simulation while eliminating post-mortem effects on tissue conductivity.

While representative electrode configurations have been presented here for both rat and human models of EST, there is such a large variety in possible treatment protocols that custom models can and should be built for direct comparison to any treatment protocol of interest. The

principles applied in the present work regarding electrical field distribution and the effects of gross anatomy and the high conductivity current paths afforded by various soft tissues through and around the skull, should apply to any mammal model. As the work suggests, the basic approach presented here can thus be applied to other mammalian models following a similar protocol of: geometry construction-> application of material properties (conductivity values), loads and boundary conditions-> model solution-> model validation/optimization with reference to empirically collected (electric potential) measurements-> prediction of current density distribution throughout the model anatomy. The methodology described here thus provides a means of accommodating future designs, allowing for objective, quantitative comparisons and predictions of current distribution in subjects undergoing EST and informing potential clinical protocols.

8. References

Andreuccetti, D., et al. "An Internet Resource for the Calculation of the Dielectric Properties of Body Tissues in the Frequency Range 10 Hz - 100 GHz." *Website at Niremf.Ifac.Cnr.It/Tissprop/*, 1997.

Ba, Jun, et al. "Intravitreal Anti-VEGF Injections for Treating Wet Age-Related Macular Degeneration: A Systematic Review and Meta-Analysis." *Drug Design, Development and Therapy*, 2015, doi:10.2147/DDDT.S86269.

Bagci, Ahmet Murat, et al. "Thickness Profiles of Retinal Layers by Optical Coherence Tomography Image Segmentation." *American Journal of Ophthalmology*, 2008, doi:10.1016/j.ajo.2008.06.010.

Breton, M. E., et al. "Analysis of ERG A-Wave Amplification and Kinetics in Terms of the G- Protein Cascade of Phototransduction." *Investigative Ophthalmology and Visual Science*, 1994.

Chen, Ming, and David Jeffery Mogul. "A Structurally Detailed Finite Element Human Head Model for Simulation of Transcranial Magnetic Stimulation." *Journal of Neuroscience Methods*, 2009, doi:10.1016/j.jneumeth.2009.01.010.

Creel, Donnell J. "The Electroretinogram and Electro-oculogram:Clinical Applications by Donnell J. Creel." *Webvision*, 2015, https://webvision.med.utah.edu/book/electrophysiology/the-electroretinogram-clinical-applications/.

Cui, Mei Lan, et al. "Bioelectrical Impedance May Predict Cell Viability during Ischemia and Reperfusion in Rat Liver." *Journal of Korean Medical Science*, 2010, doi:10.3346/jkms.2010.25.4.577.

Dawson, W. W., et al. "Improved Electrode for Electroretinography." *Investigative Ophthalmology and Visual Science*, 1979.

Derafshi, Zahra, et al. "Corneal Potential Maps Measured with Multi-Electrode Electroretinography in Rat Eyes with Experimental Lesions." *Investigative Ophthalmology and Visual Science*, 2017, doi:10.1167/iovs.16-20726.

Doslak, M. J., et al. "Numerical Solution of the Bioelectric Field." *Medical & Biological Engineering & Computing*, no. 19, 1982, pp. 149–56.

Doslak, Michael J., et al. "The Effects of Variations of the Conducting Media Inhomogeneities on the Electroretinogram." *IEEE Transactions on Biomedical Engineering*, 1980, doi:10.1109/TBME.1980.326712.

Fu, Lin, et al. "Transcorneal Electrical Stimulation Inhibits Retinal Microglial Activation and Enhances Retinal Ganglion Cell Survival After Acute Ocular Hypertensive Injury." *Translational Vision Science & Technology*, 2018, doi:10.1167/tvst.7.3.7.

Gibson, William, et al. "Transcutaneous Electrical Nerve Stimulation (TENS) for Neuropathic Pain in Adults." *Cochrane Database of Systematic Reviews*, 2017, doi:10.1002/14651858.CD011976.pub2.

Gray, Henry. *Gray's Anatomy*. Edited by T. Pickering Pick and Robert Howden, 15th ed., J. W. Edwards, 2003.

Greene, Eunice Chace. *Anatomy of The Rat*. New Series, Hafner Publishing Co., 1959.

Griffiths, D. J. "Introduction to Electrodynamics, 3rd Ed." *Prentice Hall*, 1999, doi:10.1016/S1570-

8659(04)13001-9.

Hanif, Adam M., et al. “Whole-Eye Electrical Stimulation Therapy Preserves Visual Function and Structure in P23H-1 Rats.” *Experimental Eye Research*, 2016, doi:10.1016/j.exer.2016.06.010.

Hanson, Anne. *The Rat’s Eyes*. 2012, http://ratbehavior.org/Eyes.htm.

Hasgall, PA, et al. “IT’IS Database for Thermal and Electromagnetic Parameters of Biological Tissues, Version 4.0.” *IT’IS*, 2018, doi:10.13099/VIP21000-04-0.

Hood, DC, and David G. Birch. “A Quantitative Measure of the Electrical Activity of Human Rod Photoreceptors Using Electroretinography.” *Visual Neuroscience*, 1990, doi:10.1017/S0952523800000468.

Hughes, A. “A Schematic Eye for the Rat.” *Vision Research*, 1979, doi:10.1016/0042-6989(79)90143-3.

Hunckler, Jerome, and Achala de Mel. “A Current Affair: Electrotherapy in Wound Healing.” *Journal of Multidisciplinary Healthcare*, vol. 10, 2017, pp. 179–94.

Job, H. M., et al. “Three-Dimensional Electromagnetic Model of the Human Eye: Advances towards the Optimisation of Electroretinographic Signal Detection.” *Medical and Biological Engineering and Computing*, 1999, doi:10.1007/BF02513372.

Kandel, Eric R., et al. “Principles of Neural Science. 2000.” *Appleton & Lange, New York*, 1981.

Karwoski, Chester J., and Xijing Xu. “Current Source-Density Analysis of Light-Evoked Field Potentials in Rabbit Retina.” *Visual Neuroscience*, 1999, doi:10.1017/S0952523899162163.

Kasi, Harsha, et al. “Direct Localised Measurement of Electrical Resistivity Profile in Rat and Embryonic Chick Retinas Using a Microprobe.” *Journal of Electrical Bioimpedance*, 2011, doi:10.5617/jeb.149.

Kim, Nam-Ho, and Bhavani V. Sankar. *Introduction to Finite Element Analysis and Design*. John Wiley & Sons Inc., 2009.

Kolb, Helga. “Photoreceptors by Helga Kolb.” *Webvision*, 2013, https://webvision.med.utah.edu/book/part-ii-anatomy-and-physiology-of-the-retina/photoreceptors/.

Krakau, C. E. T. “On the potential field of the rabbit electroretinogram.” *Acta Ophthalmologica*, no. 36, 1958, pp. 183–207, doi:10.1111/j.1755-3768.1958.tb07707.x.

Loduca, Ana L., et al. “Thickness Mapping of Retinal Layers by Spectral-Domain Optical Coherence Tomography.” *American Journal of Ophthalmology*, 2010, doi:10.1016/j.ajo.2010.06.034.

Machida, S., et al. “P23H Rhodopsin Transgenic Rat: Correlation of Retinal Function with Histopathology.” *Investigative Ophthalmology and Visual Science*, 2000.

Martinsen, Ørjan G., et al. “Non-Invasive Measurements of Post-Mortem Changes in Dielectric Properties of Haddock Muscle - a Pilot Study.” *Journal of Food Engineering*, 2000, doi:10.1016/S0260-8774(99)00151-X.

Morimoto, Takeshi, Tomomitsu Miyoshi, Hajime Sawai, et al. “Optimal Parameters of Transcorneal Electrical Stimulation (TES) to Be Neuroprotective of Axotomized RGCs in Adult Rats.” *Experimental Eye Research*, 2010, doi:10.1016/j.exer.2009.11.002.

Morimoto, Takeshi, Hiroyuki Kanda, Mineo Kondo, Hiroko Terasaki, et al. “Transcorneal Electrical Stimulation Promotes Survival of Photoreceptors and Improves Retinal Function in Rhodopsin P347L Transgenic Rabbits.” *Investigative Ophthalmology and Visual Science*, 2012, doi:10.1167/iovs.11-9067.

Morimoto, Takeshi, Takashi Fujikado, Jun Sub Choi, Hiroyuki Kanda, et al. “Transcorneal Electrical Stimulation Promotes the Survival of Photoreceptors and Preserves Retinal Function in Royal College of Surgeons Rats.” *Investigative Ophthalmology and Visual Science*, 2007, doi:10.1167/iovs.06-1404.

Morimoto, Takeshi, Tomomitsu Miyoshi, Satoshi Matsuda, et al. “Transcorneal Electrical Stimulation Rescues Axotomized Retinal Ganglion Cells by Activating Endogenous Retinal IGF-1 System.” *Investigative Ophthalmology and Visual Science*, 2005, doi:10.1167/iovs.04-1339.

Naycheva, L., et al. “Transcorneal Electrical Stimulation in Patients with Retinal Artery Occlusion: A Prospective, Randomized, Sham-Controlled Pilot Study.” *Ophthalmology and Therapy*, 2013, doi:10.1007/s40123-013-0012-5.

NEI. “Age-Related Macular Degeneration (AMD).” *National Eye Institute*, 2010, https://nei.nih.gov/eyedata/amd. Last accessed: June 18, 2019.

NEI “Facts About Age-Related Macular Degeneration.” *National Eye Institute*, 2018, https://nei.nih.gov/health/maculardegen/armd_facts. Last accessed: June 18, 2019. Last accessed: June 18, 2019.

Ni, Ying qin, et al. “Neuroprotective Effect of Transcorneal Electrical Stimulation on Light-Induced Photoreceptor Degeneration.” *Experimental Neurology*, 2009, doi:10.1016/j.expneurol.2009.06.016.

NORD. “Retinitis Pigmentosa.” *Rare Disease Database*, *National Organization for Rare Disorders*, 2017, https://rarediseases.org/rare-diseases/retinitis-pigmentosa/.

Nunez, Paul L., and Ramesh Srinivasan. “Electric Fields of the Brain: The Neurophysics of EEG.” *Electric Fields of the Brain: The Neurophysics of EEG*, 2009, doi:10.1093/acprof:oso/9780195050387.001.0001.

Olsen, Timothy W., et al. “Human Sclera: Thickness and Surface Area.” *American Journal of Ophthalmology*, 1998, doi:10.1016/S0002-9394(99)80096-8.

Oyster, Clyde W. “The Human Eye: Structure and Function.” *Nature Medicine*, 1999, doi:978-0-87893-644-1.

Pardue, Machelle T., et al. “Neuroprotective Effect of Subretinal Implants in the RCS Rat.” *Investigative Ophthalmology and Visual Science*, 2005, doi:10.1167/iovs.04-0515.

Pardue, Machelle T., and Rachael S. Allen. “Neuroprotective Strategies for Retinal Disease.” *Progress in Retinal and Eye Research*, 2018, doi:10.1016/j.preteyeres.2018.02.002.

Peratta, A. “3D Low Frequency Electromagnetic Modelling of the Human Eye with Boundary Elements: Application to Conductive Keratoplasty.” *Engineering Analysis with Boundary Elements*, 2008, doi:10.1016/j.enganabound.2007.11.010.

Perlman, Ido. “Webvision The Electroretinogram : ERG by Ido Perlman.” *Webvision*, 2015.

Perlman, Ido, and Shiri Soudry. “Bright-Flash Electroretinogram.” *Encyclopedia of Ophthalmology*, 2015, doi:10.1007/978-3-642-35951-4_1034-1.

Poljak, Dragan, et al. “The Assessment of Human Exposure to Low Frequency and High Frequency Electromagnetic Fields Using the Boundary Element Analysis.” *Engineering Analysis with Boundary Elements*, 2003, doi:10.1016/S0955-7997(03)00070-5.

Potschka, Heidrun, and Wolfgang Löscher. “Corneal Kindling in Mice: Behavioral and Pharmacological Differences to Conventional Kindling.” *Epilepsy Research*, 1999, doi:10.1016/S0920-1211(99)00062-5.

Rahmani, Safa, et al. “Chronic Delivery of Low-Level Exogenous Current Preserves Retinal Function in Pigmented P23H Rat.” *Vision Research*, 2013, doi:10.1016/j.visres.2012.10.016.

Roth, Bjørn, et al. “Pre or Post Mortem Muscle Activity in Atlantic Salmon (Salmo Salar). The Effect on Rigor Mortis and the Physical Properties of Flesh.” *Aquaculture*, 2006, doi:10.1016/j.aquaculture.2005.10.021.

Schachar, R. A., et al. “Insights into the Age-Related Decline in the Amplitude of Accommodation of the Human Lens Using a Non-Linear Finite-Element Model.” *British Journal of Ophthalmology*, 2006, doi:10.1136/bjo.2006.100347.

Schatz, Andreas, Tobias Röck, et al. “Transcorneal Electrical Stimulation for Patients with Retinitis Pigmentosa: A Prospective, Randomized, Sham-Controlled Exploratory Study.” *Investigative Ophthalmology & Visual Science*, 2011, doi:10.1167/iovs.10-6932.

Schatz, Andreas, Johanna Pach, et al. “Transcorneal Electrical Stimulation for Patients with Retinitis Pigmentosa: A Prospective, Randomized, Sham-Controlled Follow-up Study over 1 Year.” *Investigative Ophthalmology and Visual Science*, 2017, doi:10.1167/iovs.16-19906.

Sehic, Amer, et al. “Electrical Stimulation as a Means for Improving Vision.” *American Journal of Pathology*, 2016, doi:10.1016/j.ajpath.2016.07.017.

Selner, Ashley N., et al. “Three-Dimensional Model of Electroretinogram Field Potentials in the Rat Eye.” *IEEE Transactions on Biomedical Engineering*, 2018, doi:10.1109/TBME.2018.2816591.

Serway, Raymond A. *Principles of Physics*. 2nd ed., Brooks Cole, 1997, doi:10.1007/978-3-642-23026-4.

Shahidi, Mahnaz, et al. “Quantitative Thickness Measurement of Retinal Layers Imaged by Optical Coherence Tomography.” *American Journal of Ophthalmology*, 2005, doi:10.1016/j.ajo.2005.01.012.

Sieving, Paul A., et al. “ Push–Pull Model of the Primate Photopic Electroretinogram: A Role for Hyperpolarizing Neurons in Shaping the b -Wave .” *Visual Neuroscience*, 1994, doi:10.1017/s0952523800002431.

Su, Yongxian, et al. “Photodynamic Therapy in Combination with Ranibizumab versus Ranibizumab Monotherapy for Wet Age-Related Macular Degeneration: A Systematic Review and Meta-Analysis.” *Photodiagnosis and Photodynamic Therapy*, 2018, doi:10.1016/j.pdpdt.2018.05.002.

Sung, C. H., et al. “Functional Heterogeneity of Mutant Rhodopsins Responsible for Autosomal Dominant Retinitis Pigmentosa.” *Proceedings of the National Academy of Sciences*, 2006, doi:10.1073/pnas.88.19.8840.

Tagami, Yuichi, et al. “Axonal Regeneration Induced by Repetitive Electrical Stimulation of Crushed Optic Nerve in Adult Rats.” *Japanese Journal of Ophthalmology*, 2009, doi:10.1007/s10384-009-0657-8.

Takeda, Kotaro, et al. “Review of Devices Used in Neuromuscular Electrical Stimulation for Stroke Rehabilitation.” *Medical Devices: Evidence and Research*, 2017, doi:10.2147/MDER.S123464.

Vurgese, Sujiv, et al. “Scleral Thickness in Human Eyes.” *PLoS ONE*, 2012, doi:10.1371/journal.pone.0029692.

Wang, Boshuo, and James D. Weiland. “Resistivity Profiles of Wild-Type, Rd1, and Rd10 Mouse Retina.” *Proceedings of the Annual International Conference of the IEEE Engineering in Medicine and Biology Society, EMBS*, 2015, doi:10.1109/EMBC.2015.7318692.

Wang, Xiang-Ning, et al. “The Thickness and Volume of the Choroid, Outer Retinal Layers and Retinal Pigment Epithelium Layer Changes in Patients with Diabetic Retinopathy.” *International Journal of Ophthalmology*, 2018, doi:10.18240/ijo.2018.12.14.

Wendel-Mitoraj, Katrina Stoliar, Dmytro, et al. “Measuring Tissue Thicknesses of the Human Head Using Centralized and Normalized Trajectories.” *Consciousness and Its Measures*, 2008.

Willand, Michael P., et al. “Electrical Stimulation to Promote Peripheral Nerve Regeneration.” *Neurorehabilitation and Neural Repair*, 2016, doi:10.1177/1545968315604399.

Xie, John, et al. “Modeling and Percept of Transcorneal Electrical Stimulation in Humans.” *IEEE Transactions on Biomedical Engineering*, 2011, doi:10.1109/TBME.2010.2087378.

Yin, Houmin, et al. “Transcorneal Electrical Stimulation Promotes Survival of Retinal Ganglion Cells after Optic Nerve Transection in Rats Accompanied by Reduced Microglial Activation and TNF-α Expression.” *Brain Research*, 2016, doi:10.1016/j.brainres.2016.08.034.

Zampatti, Stefania, et al. “Review of Nutrient Actions on Age-Related Macular Degeneration.” *Nutrition Research*, 2014, doi:10.1016/j.nutres.2013.10.011.

Zhang, Chunwei, et al. “Relationship between Ganglion Cell Layer Thickness and Estimated Retinal Ganglion Cell Counts in the Glaucomatous Macula.” *Ophthalmology*, 2014, doi:10.1016/j.ophtha.2014.06.047.

Zheng, E., et al. “Impedance of Skeletal Muscle from 1 Hz to 1 MHz.” *IEEE Transactions on Biomedical Engineering*, 1984, doi:10.1109/TBME.1984.325417.

9. Appendix

9.1. Supplemental figures

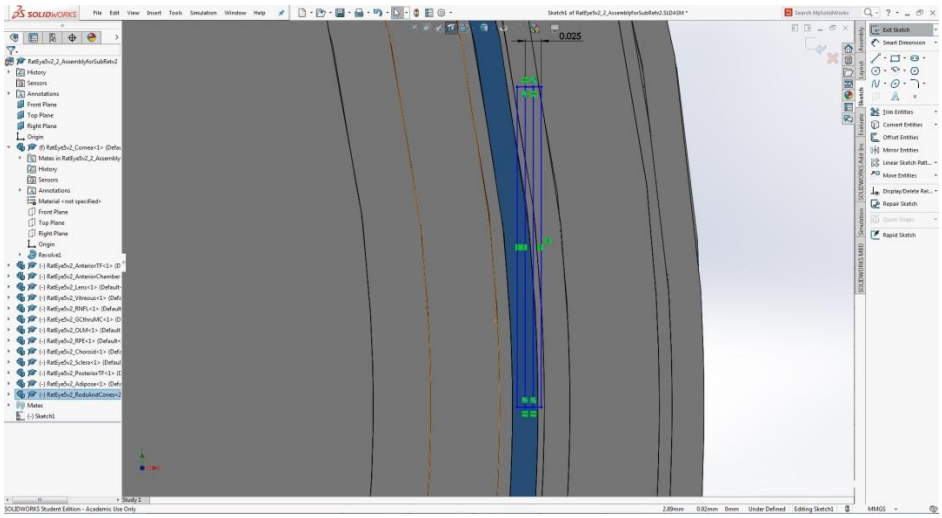

Figure 50 Placement of the subretinal implant.

Placement of the subretinal implant in the SES configuration for EST. The implant falls mainly within the photoreceptor layer (highlighted in blue) but also contacts the RPE and choroid layers.

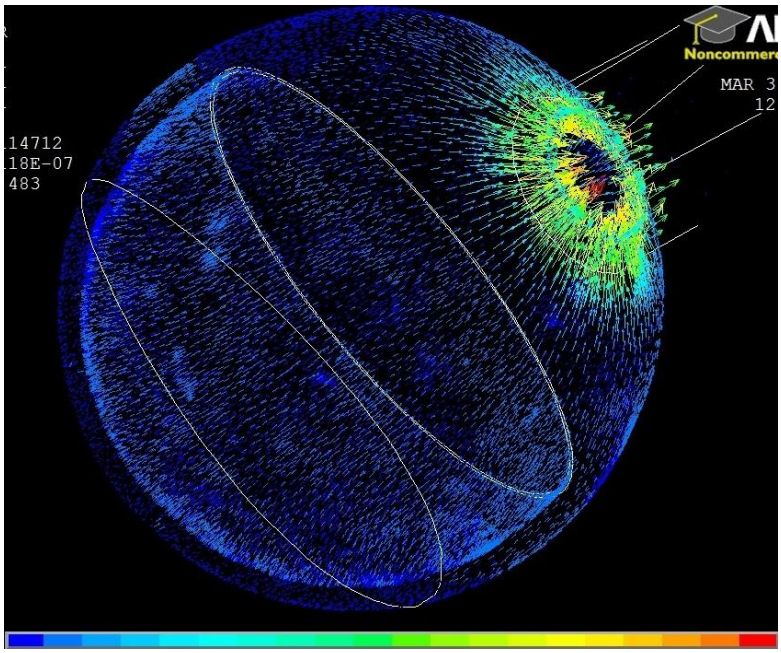

Figure 51 Vector plot of electric field in early modeling efforts.

Vector plot of electric field in early modeling efforts in ANSYS, layers selectively removed for better view of field concentrated in the vicinity of a stimulating electrode placed on the model rat cornea.

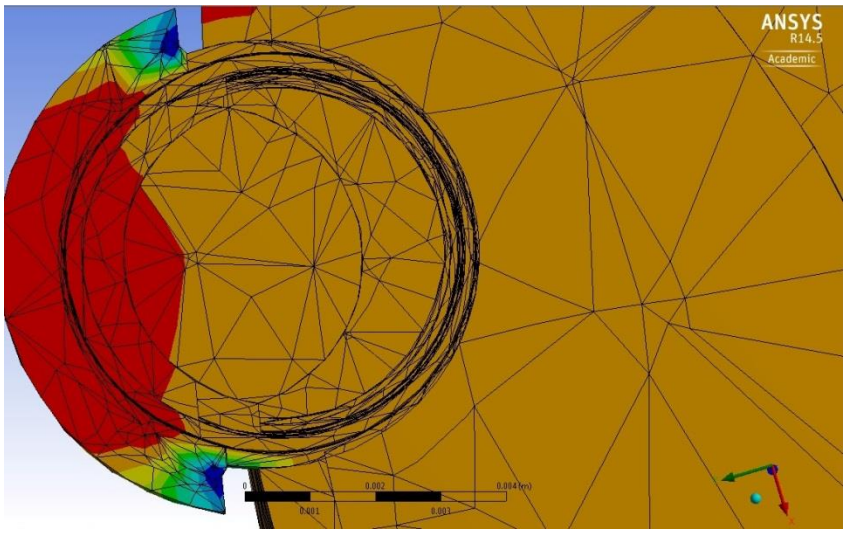

Figure 52 Electric potential distribution, TES cross-section

This color contour plot (max. voltage in red, min. in blue) shows voltage distribution in the rat model with the TES electrode configuration applied. The oblique cross-sectional view here highlights concentration of the field (in red) near the stimulating ring electrode embedded in the center of the contact lens and the minimum in the field at the reference ring electrode placed near the outer edge of the lens.

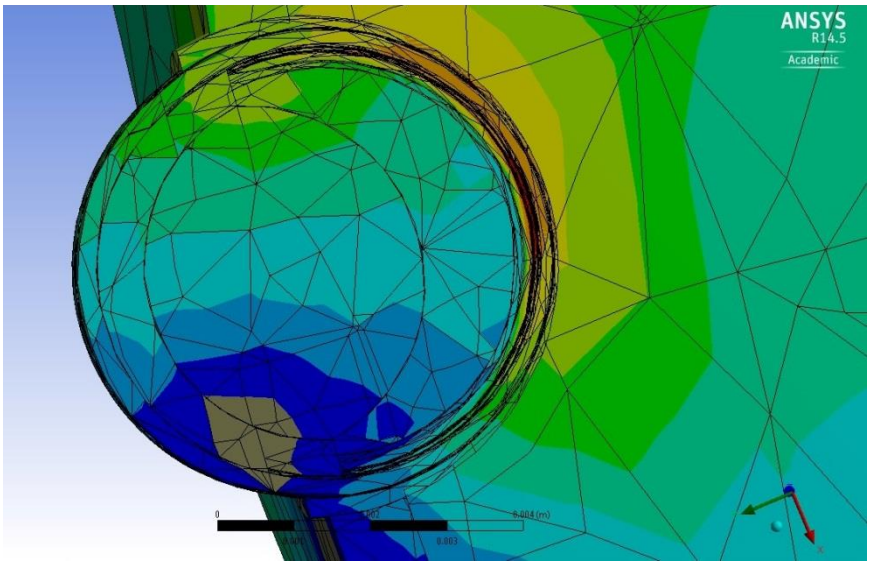

Figure 53 Electric potential distribution, SES cross-section

This color contour plot (max. voltage in red, min. in blue) shows voltage distribution in the rat model with the SES electrode configuration applied. The oblique cross-sectional view here highlights concentration of the field (in red) near the stimulating electrode surface at the back of the eye.

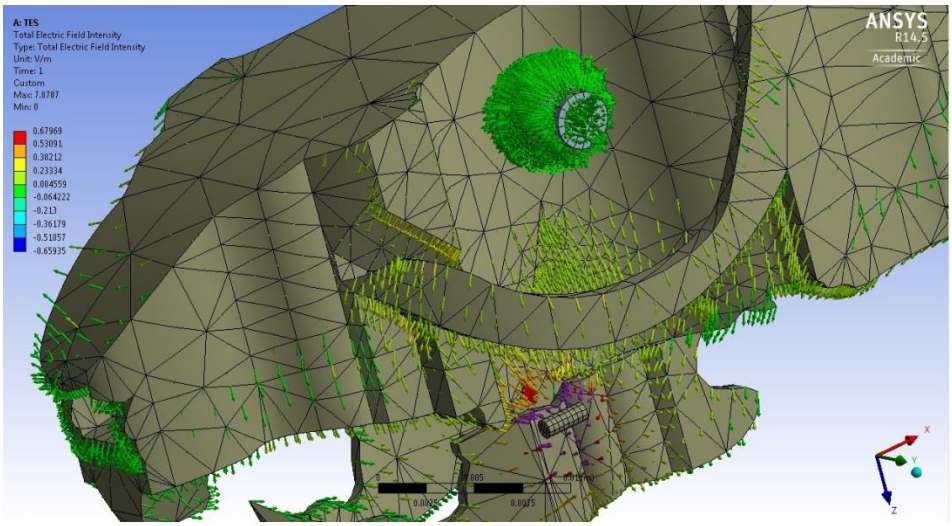

Figure 54 Vector plot, early efforts with detailed rat head model.

This vector plot shows the electric field from the WES electrode configuration for EST applied to the detailed "Remy" model of the head, with layers selectively removed to highlight field distribution with relation to the relatively low-conductivity skull. Note the field emanating anterior from the nasal cavity as well as from foramina inferior to the eye.

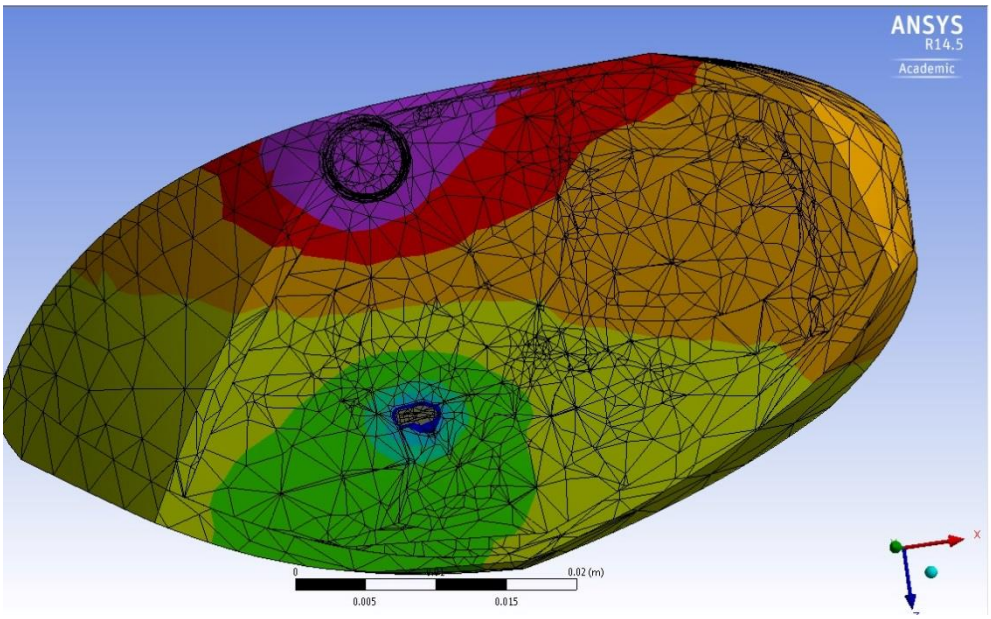

Figure 55 Color contour plot, early efforts with detailed rat head model.

This color contour plot shows electric potential distribution from the WES electrode configuration for EST applied to the detailed "Remy" model of the head, with a cross-sectional view take to highlight field max. (purple) and min. (blue) near the stimulating and reference electrodes respectively.

9.2. Permissions

Permission for use in Figure 1., Figure 3. and Figure 8.

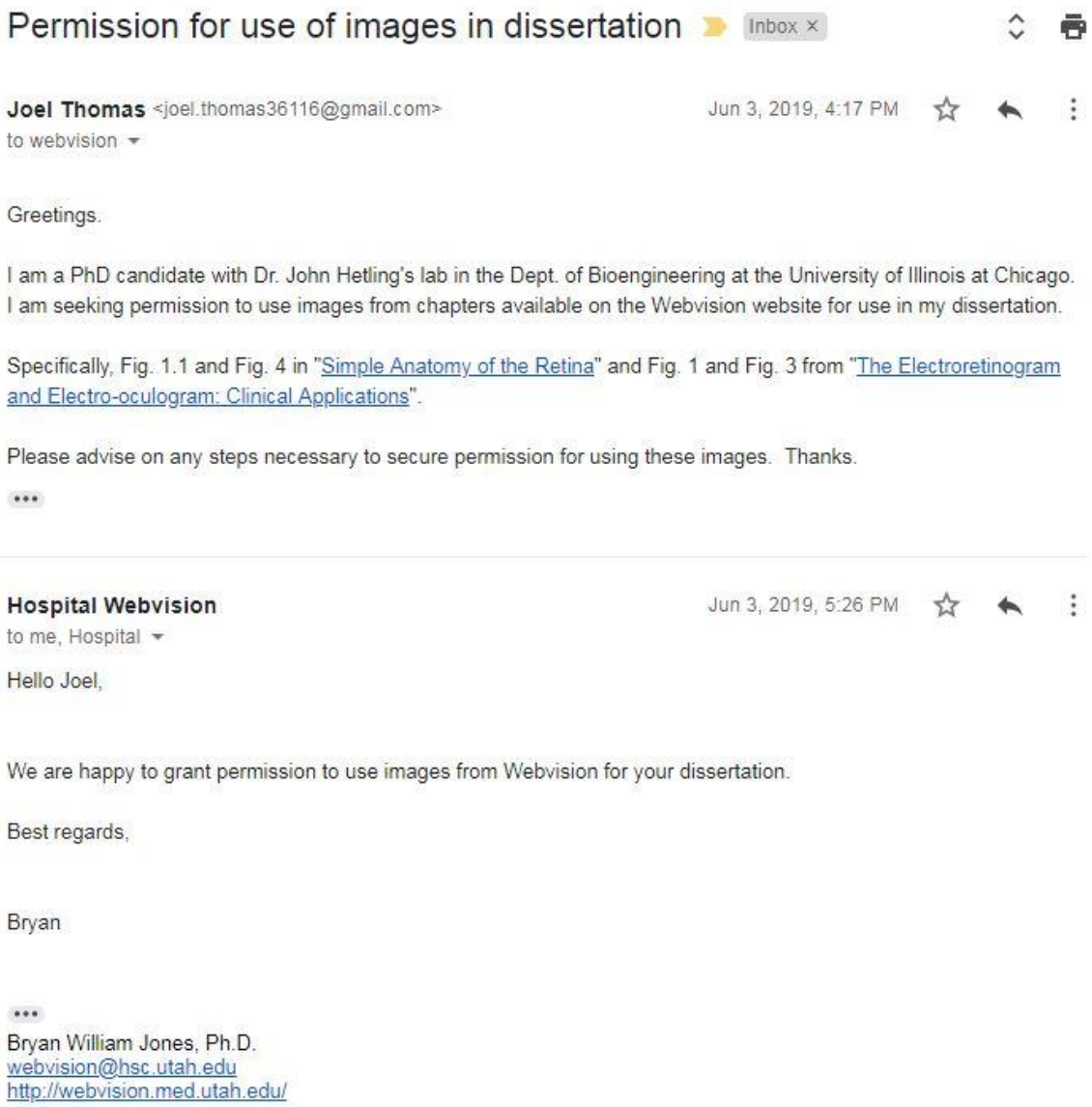

Permission for use of images in dissertation Inbox ×

Joel Thomas <joel.thomas36116@gmail.com> Jun 3, 2019, 4:17 PM

to webvision

Greetings.

I am a PhD candidate with Dr. John Hetling's lab in the Dept. of Bioengineering at the University of Illinois at Chicago. I am seeking permission to use images from chapters available on the Webvision website for use in my dissertation.

Specifically, Fig. 1.1 and Fig. 4 in "Simple Anatomy of the Retina" and Fig. 1 and Fig. 3 from "The Electroretinogram and Electro-oculogram: Clinical Applications".

Please advise on any steps necessary to secure permission for using these images. Thanks.

Hospital Webvision Jun 3, 2019, 5:26 PM

to me, Hospital

Hello Joel,

We are happy to grant permission to use images from Webvision for your dissertation.

Best regards,

Bryan

Bryan William Jones, Ph.D.
webvision@hsc.utah.edu
http://webvision.med.utah.edu/

Permission for use in Figure 4.

PLS Clear

PARTIES:

1. **Oxford Publishing Limited** (Company number – 01748118) (Licensor); and
2. **Joel Thomas** (Licensee).

Thank you for your recent permission request. Some permission requests for use of material published by the Licensor, such as this one, are now being facilitated by PLSclear.

Set out in this licence cover sheet (the **Licence Cover Sheet**) are the principal commercial terms under which Licensor has agreed to license certain Licensed Material (as defined below) to Licensee. The terms in this Licence Cover Sheet are subject to the attached General Terms and Conditions, which together with this Licence Cover Sheet constitute the licence agreement (the **Licence**) between Licensor and Licensee as regards the Licensed Material. The terms set out in this Licence Cover Sheet take precedence over any conflicting provision in the General Terms and Conditions.

Licence Terms

Licence Date:	05/06/2019
PLSclear Ref No:	14833

The Licensor

Company name:	Oxford Publishing Limited
Address:	Rights Department Great Clarendon Street Oxford OX2 6DP GB

The Licensee

Licensee Contact Name:	Joel Thomas
Licensee Address:	[redacted] United States

Licensed Material

title:	Electric fields of the brain : the neurophysics of EEG
ISBN/ISSN:	9780195027969
publisher:	Oxford Publishing Limited

figure number & title / caption	Fig. 6-5
page number	183
position on page	top
reproduction colour	Black and White
reproduction size	Quarter page
positioning	inside or later pages
Are you requesting permission to reuse your own work?	No. I am NOT the author

figure number & title / caption	Fig. 6-7
page number	189
position on page	top
reproduction colour	Black and White
positioning	inside or later pages
Are you requesting permission to reuse your own work?	No. I am NOT the author

For Use In Licensee's Publication(s)

usage type	Book, Journal, Magazine or Academic Paper...-Thesis
language	English
publication title	Quantitative Evaluation of Electrical Stimulation Therapy for Eye Disease
type of document	Thesis

Rights Granted

Exclusivity:	Non-Exclusive
Format:	THESIS/WHITEPAPER/CONULTATION DOCUMENT
Language:	English
Territory:	USA
Duration:	Lifetime of Licensee's edition
Maximum Circulation:	Total: 1 copies
Additional Terms:	If at some future date your thesis is published it will be necessary to re-clear this permission. Please also note that if the material to be used is acknowledged to any other source, you will need to clear permission with the rights holder and for any electronic version the © line must appear on the same page as the OUP material and the OUP material should not be included under a Creative Commons license, or any other open-access license allowing onward reuse.

Permission for use in Figure 5.

SPRINGER NATURE LICENSE
TERMS AND CONDITIONS

Jun 19, 2019

This Agreement between Joel Thomas ("You") and Springer Nature ("Springer Nature") consists of your license details and the terms and conditions provided by Springer Nature and Copyright Clearance Center.

License Number	4612570887438
License date	Jun 19, 2019
Licensed Content Publisher	Springer Nature
Licensed Content Publication	Medical & Biological Engineering & Computing
Licensed Content Title	Numerical solution of the bioelectric field of the e.r.g.
Licensed Content Author	M. J. Doslak, R. Plonsey, C. W. Thomas
Licensed Content Date	Jan 1, 1981
Licensed Content Volume	19
Licensed Content Issue	2
Type of Use	Thesis/Dissertation
Requestor type	academic/university or research institute
Format	print and electronic
Portion	figures/tables/illustrations
Number of figures/tables/illustrations	1
Will you be translating?	no
Circulation/distribution	<501
Author of this Springer Nature content	no
Title	Quantitative Evaluation of Electrical Stimulation Therapy for Eye Disease
Institution name	n/a
Expected presentation date	Jul 2019
Portions	Fig.1 The two-dimensional model depicting the e.r.g. source and volume conductor inhomogeneities.
Requestor Location	Joel Thomas [redacted] Attn: Joel Thomas
Total	0.00 USD
Terms and Conditions	

Permission for use in Figure 6.

SPRINGER NATURE LICENSE
TERMS AND CONDITIONS

Jun 19, 2019

This Agreement between Joel Thomas ("You") and Springer Nature ("Springer Nature") consists of your license details and the terms and conditions provided by Springer Nature and Copyright Clearance Center.

License Number	4612571307656
License date	Jun 19, 2019
Licensed Content Publisher	Springer Nature
Licensed Content Publication	Medical & Biological Engineering & Computing
Licensed Content Title	Three-dimensional electromagnetic model of the human eye: advances towards the optimisation of electroretinographic signal detection
Licensed Content Author	H. M. Job, D. Keating, A. L. Evans et al
Licensed Content Date	Jan 1, 1999
Licensed Content Volume	37
Licensed Content Issue	6
Type of Use	Thesis/Dissertation
Requestor type	academic/university or research institute
Format	print and electronic
Portion	figures/tables/illustrations
Number of figures/tables/illustrations	1
Will you be translating?	no
Circulation/distribution	<501
Author of this Springer Nature content	no
Title	Quantitative Evaluation of Electrical Stimulation Therapy for Eye Disease
Institution name	n/a
Expected presentation date	Jul 2019
Portions	Figure 4. Corneal potential topography following global retinal stimulation
Requestor Location	Joel Thomas [redacted] Attn: Joel Thomas
Total	0.00 USD

Permission for use in Figure 7.

Thesis / Dissertation Reuse

The IEEE does not require individuals working on a thesis to obtain a formal reuse license, however, you may print out this statement to be used as a permission grant:

Requirements to be followed when using any portion (e.g., figure, graph, table, or textual material) of an IEEE copyrighted paper in a thesis:

1) In the case of textual material (e.g., using short quotes or referring to the work within these papers) users must give full credit to the original source (author, paper, publication) followed by the IEEE copyright line © 2011 IEEE.
2) In the case of illustrations or tabular material, we require that the copyright line © [Year of original publication] IEEE appear prominently with each reprinted figure and/or table.
3) If a substantial portion of the original paper is to be used, and if you are not the senior author, also obtain the senior author's approval.

Permission for use in Figure 9., Figure 10, Figure 11.

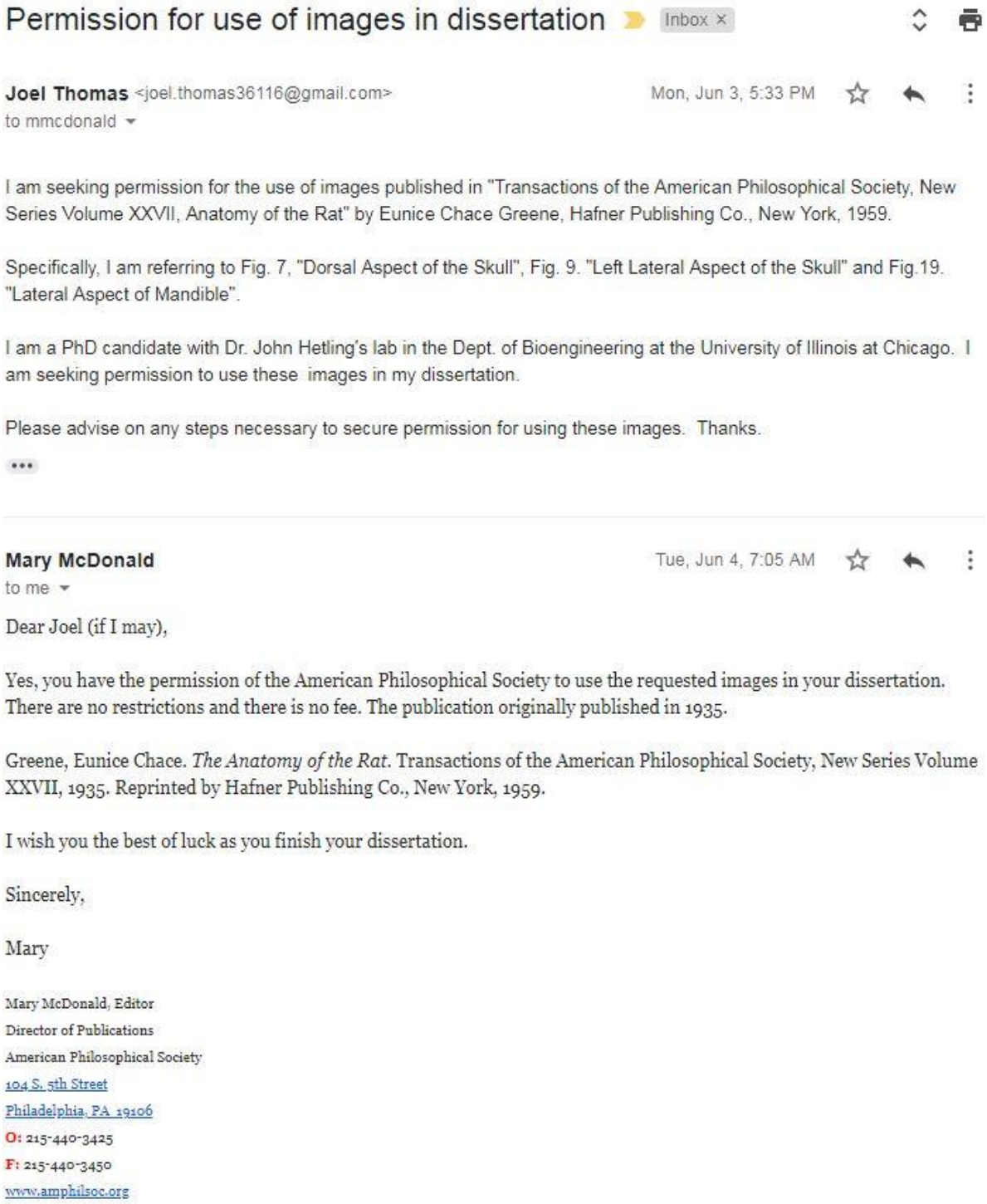

Permission for use of images in dissertation Inbox ×

Joel Thomas <joel.thomas36116@gmail.com> Mon, Jun 3, 5:33 PM

to mmcdonald

I am seeking permission for the use of images published in "Transactions of the American Philosophical Society, New Series Volume XXVII, Anatomy of the Rat" by Eunice Chace Greene, Hafner Publishing Co., New York, 1959.

Specifically, I am referring to Fig. 7, "Dorsal Aspect of the Skull", Fig. 9. "Left Lateral Aspect of the Skull" and Fig.19. "Lateral Aspect of Mandible".

I am a PhD candidate with Dr. John Hetling's lab in the Dept. of Bioengineering at the University of Illinois at Chicago. I am seeking permission to use these images in my dissertation.

Please advise on any steps necessary to secure permission for using these images. Thanks.

•••

Mary McDonald Tue, Jun 4, 7:05 AM

to me

Dear Joel (if I may),

Yes, you have the permission of the American Philosophical Society to use the requested images in your dissertation. There are no restrictions and there is no fee. The publication originally published in 1935.

Greene, Eunice Chace. *The Anatomy of the Rat*. Transactions of the American Philosophical Society, New Series Volume XXVII, 1935. Reprinted by Hafner Publishing Co., New York, 1959.

I wish you the best of luck as you finish your dissertation.

Sincerely,

Mary

Mary McDonald, Editor
Director of Publications
American Philosophical Society
104 S. 5th Street
Philadelphia, PA 19106
O: 215-440-3425
F: 215-440-3450
www.amphilsoc.org

Permission for use in Figure 13.

Title:	A schematic eye for the rat
Author:	A. Hughes
Publication:	Vision Research
Publisher:	Elsevier
Date:	1979

Logged in as:
Joel Thomas
LOGOUT

Order Completed

Thank you for your order.

This Agreement between Joel Thomas ("You") and Elsevier ("Elsevier") consists of your license details and the terms and conditions provided by Elsevier and Copyright Clearance Center.

Your confirmation email will contain your order number for future reference.

printable details

License Number	4601581504485
License date	Jun 03, 2019
Licensed Content Publisher	Elsevier
Licensed Content Publication	Vision Research
Licensed Content Title	A schematic eye for the rat
Licensed Content Author	A. Hughes
Licensed Content Date	Jan 1, 1979
Licensed Content Volume	19
Licensed Content Issue	5
Licensed Content Pages	20
Type of Use	reuse in a thesis/dissertation
Portion	figures/tables/illustrations
Number of figures/tables/illustrations	1
Format	electronic
Are you the author of this Elsevier article?	No
Will you be translating?	No
Original figure numbers	Fig. 4
Title of your thesis/dissertation	Quantitative Evaluation of Electrical Stimulation Therapy for Eye Disease
Expected completion date	Jul 2019
Estimated size (number of pages)	120
Requestor Location	Joel Thomas [redacted] United States Attn: Joel Thomas
Publisher Tax ID	98-0397604
Total	0.00 USD

10. Vita

EDUCATION

- PhD candidate, University of Illinois at Chicago (UIC)- Department of Bioengineering
  Aug. 2009 - present
  - Concentration in neural engineering, curriculum emphasis on neuroscience and computational analysis.
  - Investigating the use of low-level electric currents as a therapy for degenerative retinal diseases using electroretinogram (ERG) analysis and finite element (FE) modeling of current density distribution.
- Bachelor of Science, University of Illinois at Chicago (UIC)- Department of Bioengineering,
  Dec. 2007
  - Concentration in neural engineering, curriculum emphasis on neuroscience and electronics.
  - *Project leader*, senior design, 2006-2007; a new microdrive to enable cyclic voltammetry in awake mice via carbon fiber electrodes. Coordinated development and implementation, in conjunction with faculty & peer efforts. Presentation at annual student engineering exposition. Certified in animal handling protocol.
  - Awarded Chancellor's Student Service and Leadership Award, 2007-2008

RESEARCH INTERESTS

- Neural engineering
- Electronics-based bioengineering
- Vision science
- Medical devices
- Computational modeling of biology

PROFESSIONAL EXPERIENCE

UIC- Office of Technology Management – *Technology Commercialization Analyst* Sept.2013-Aug.2015,

- Evaluated disclosures of new technologies for viable intellectual property Jan. 2017- May 2018
- Reviewed market landscapes, filing decisions and licensing agreements on select inventions
- Presented findings on emergent technologies at regular interdisciplinary group meetings

Cardinal Intellectual Property – *Patent Search Analyst* Aug. 2016-Oct. 2016

- Reviewed patent applications, addressing claims on novelty, inventive step
- Conducted prior-art searches, classified and drafted professional opinion on applications

UIC- University of Illinois Alumni Association – *Graduate Assistant* Jan.2013 – May 2014

- Create/support educational and professional initiatives utilizing the U of I alumni network
- Advise Student Alumni Ambassadors in organizational, professional and academic pursuits

UIC- Department of Bioengineering - *Lab Manager/Research Assistant* Jan. 2009 – Jan. 2013

- Analyzed ERG data & recommended bioinstrumentation purchases, use & maintenance
- Computationally modeled electrical current density related to treatment protocols
- Trained/collaborated with undergraduates on various scientific research projects

UIC- Campus Housing - *Assistant Resident Director* July 2008 - June 2010

- Supervised & counseled student staff, advised student leaders
- Modeled student learning outcomes, prepared documentation and trained staff
- Managed routine residence hall functions & crisis response
- Awarded Student Staff Supervisor of the Year, 2009-2010.

AFFILIATIONS

- American Association for the Advancement of Science (AAAS) June 2015- Present

- SponsorLove Community Service Foundation – *IT Specialist* Sept.2012-Jan.2015
  - Served on executive team as administrator and advisor on IT infrastructure and usage
  - Developed and maintained web content via Drupal based CRM interface
  - Coordinated community meetings and service projects, often in collaboration with other nonprofits such as Habitat for Humanity and Heartland Alliance.

- Association for Research in Vision and Ophthalmology (ARVO) Nov. 2009 – Nov. 2012
  - *Member*; presented research at 2011 annual meeting

PUBLICATIONS

Thomas, J.G., Hetling, J.R., Distribution of Current Density at the Retina During Electrical Stimulation Therapy Predicted by an Electrostatic Model, *Vision Research*, in review, summer 2019.

Hanif, A. M., Kim, M. K., Thomas, J. G., Ciavatta, V. T., Chrenek, M., Hetling, J. R., & Pardue, M. T. (2016). Whole-eye electrical stimulation therapy preserves visual function and structure in P23H-1 rats. *Experimental Eye Research*. https://doi.org/10.1016/j.exer.2016.06.010

Rahmani, S., Bogdanowicz, L., Thomas, J., & Hetling, J. R. (2013). Chronic delivery of low-level exogenous current preserves retinal function in pigmented P23H rat. *Vision Research*. https://doi.org/10.1016/j.visres.2012.10.016

Kim, M. K., Thomas, J. G., Adkins, A., Ciavatta, V. T., Hetling, J. R., & Pardue, M. T. (2012) Electrical stimulation therapy preserves visual acuity and retinal ganglion cells in P23H-1 rats, *Association for Research in Vision and Ophthalmology* Annual Meeting, 2012.

Thomas, J. G., Selner, A., & Hetling, J. R., (2011) Exogenous currents delivered to the eye as a potential therapy: computational model comparing two electrode geometries in rat, *Association for Research in Vision and Ophthalmology* Annual Meeting, 2011.